Universitá degli Studi di Napoli "Federico II"
Graduate School of Physical Sciences
Research Doctorate in Fundamental and Applied Physics

Macroscopic quantum phenomena in superconductors: study of phase dynamics and dissipation in moderately damped Josephson junctions

Doctoral dissertation by
Davide Massarotti

Tutor:
Prof. Francesco Tafuri

Coordinator:
Prof. Raffaele Velotta

XXV cycle 2010-2013

Contents

Introduction **3**

1 Phase dynamics of superconducting Josephson junctions **7**

1.1 Underdamped Josephson junctions 9

1.2 Moderately damped regime 14

1.3 HTS Josephson junctions: grain boundary junctions 18

1.4 Macroscopic quantum phenomena in HTS based Josephson junctions 23

1.5 Switching processes in nanostructures 26

2 Experimental setup **28**

2.1 Dilution fridge 29

2.2 Electronic setup 33

2.3 Functioning of the measurement setup 36

3 Measurements and data analysis **41**

3.1 Phase dynamics of underdamped Josephson junctions 42

3.2 Macroscopic quantum tunneling in moderately damped NbN Josephson junctions 45

3.3 Diffusive dynamics in moderately damped NbN Josephson junctions 48

3.4 Ramp rate dependence of the transition temperature from thermal activation to phase diffusion regime 54

3.5 Phase dynamics of YBCO grain boundary Josephson junctions 56

3.6 Direct transition from MQT to phase diffusion in YBCO grain boundary Josephson junctions 61

4 Phase dynamics at extreme conditions **69**
4.1 Phase delocalization in the washboard potential 71
4.2 Approaching quantum phase diffusion in sub-micrometric YBCO grain boundary structures 74
4.3 Switching processes in superconducting nanowires 82
4.4 Switching dynamics of high critical current density YBCO Josephson junctions 86

Conclusions **91**

Bibliografy **94**

Introduction

The possibility that a macroscopic system could behave quantum mechanically if it was suitably decoupled from its environment[1] was somehow the start of an intense research activity aimed to investigate the boundary between the microscopic quantum and macroscopic classical worlds. Leggett immediately emphasized the importance of distinguishing macrosocpic quantum phenomena originating in the superposition of a large number of microscopic variables (such as superfluidity and superconductivity) from those displayed by a single macroscopic degree of freedom.

The Josephson effect[2] and the phenomena occurring in Josephson devices[3, 4] have been in these last 50 years a continuous source of inspiration and progress in physics. We have been learning by investigating a Josephson device, how macroscopic coherence propagates in heterostructures[1, 3, 4], how macroscopic and microscopic phases coherently combine at superconductor/normal metal (S/N) interfaces[5] of a S/N/S Josephson junction (JJ), how a Josephson coupling can unambiguously identify unconventional symmetry of the order parameter, as occurring in high critical temperature superconductors (HTS)[6].

Because of their design scalability and their flexibility in controlling the level of damping, Josephson systems have proven to be a fantastic test bench for studying fundamental physics problems such as quantum coherence in macroscopic systems, taking advantage from the anharmonicity deriving from the Josephson equations[2]. In the 1980s, the macroscopic quantum nature of the phase difference across a JJ has been demonstrated[7, 8, 9, 10, 11, 12, 13, 14, 15]. Quantum mechanics has been recently used to explain the behavior of superconducting circuits, that can be hundreds of nanometres wide and can contain trillions of electrons and function in a quantum design logic. The quantum nature of these circuits is observable because they can be to a significant level decoupled from the electrical environment[16].

The detection of macroscopic quantum tunneling and energy-level quantization in conventional JJ circuits[13, 14, 15] are the first step in the integration of superconducting junctions in a quantum system. This has been solidly established for low critical temperature superconductors (LTS) JJs, where the quantum superposition of distinct macroscopic states[17, 18] and the observation of Rabi oscillations[19, 20, 21, 22] have been also reported. For example, in the experiment of Friedman et al.[17] the tunneling object is the magnetic flux set up by billions of electron pairs coherently circulating within a superconducting ring.

Advances in material science and in the application of nanotechnologies to superconducting devices are leading to novel and promising devices in view of quantum systems, whose complete competitiveness has to be evaluated along with a possible impact on the fundamental themes of coherence and dissipation.

Between such structures, a particular mention should be dedicated to HTS oxides, which from 1986 have enlarged the occurrence of superconductivity to unexpected energy and length scales. This is obviously true also for the Josephson effect. Dimensionality, strong correlations, d-wave order parameter (OP) symmetry represent some of the most important features which contribute to define the properties of HTS[6, 23]. Therefore, HTS have really opened the new horizons of unconventional superconductivity, where probably all bundles will converge for a more complete understanding of its nature.

Recently, the observation of macroscopic quantum effects in HTS JJs[24, 25, 26] paved the way to the possible use of HTS in quantum hybrid circuits. From such experiments, studies on macroscopic quantum behavior have been extended to novel types of junctions, such as those composed of novel materials, or devices scaled to the nano-size or based on novel design concepts, as intrinsic junctions in HTS[27] or junctions using nanowires or graphene sheets[28] as barriers.

Therefore we look at phase dynamics aware that material science is not only offering a variety of novel interfaces and junctions, but also radically new solutions of synthesizing hybrid Josephson devices taking advantage at the same time of the progress registered in using nanotechnologies in superconducting electronics. The pioneering studies of Ono et al.[29], Iansiti et al.[30], and Kautz and Martinis[31] on phase diffusion on small junctions can be now supported and developed by different types of junctions of quite different sizes. We are specifically interested in discussing phase dynamics at intermediate levels of dissipation (moderately damped regime), which is going to permeate more and more the nature of futuristic superconducting hybrid nanostructures[32, 33].

The topic of such PhD project is a comparative study of phase dynamics and macroscopic quantum phenomena in moderately damped NbN trilayer and YBCO grain boundary (GB) JJs. This type of research activity responds to the needs of better identifying phase dynamics in JJs in the moderately damped regime[31, 34, 35, 36], which represents the technological result of the application of nanotechnology to LTS devices, and of the implementation of novel types of hybrid systems. Issues on a more detailed understanding of coherence, dissipation and noise in the various devices have a relevant role in the progress of quantum circuits.

The thesis has been organized in the following way: in the first chapter, phase dynamics of underdamped and moderately damped JJs will be addressed, both in the thermal and in the quantum regime. Phase dynamics will be studied as function of the damping both in conventional LTS JJs and in HTS structures, with particular attention to YBCO GB biepitaxial junctions.

In the second chapter the experimental setup will be described: the efforts in order to minimize the effects of noise and coupling from the environment will be highlighted, with the goal to build-up a reliable measurement system for the search of macroscopic quantum phenomena.

In the third chapter experimental results on the switching processes of moderately damped JJs will be discussed. Both LTS junctions (NbN JJs) and HTS structures (YBCO GB biepitaxial JJs) will be analyzed. Such measurements are supported by numerical codes, able to take into account the dissipation level in a wide range of junction conditions. An interesting and comprehensive result is the reconstruction of a phase diagram which summarizes the various activation regimes as a function of the fundamental junction energies and parameters.

Finally, in the last chapter phase dynamics of GB YBCO JJs will be addressed in the two limits of very low critical current density J_c and relatively high J_c. Experiments will be interpreted with the help of numerical models. In the former case phase dynamics at very low critical current and high dissipation level will be studied, and the quantum diffusion regime will be approached[30, 37]. In the latter case, switching dynamics has been used as a powerful tool in order to define the duality between the the Josephson effect and phase-slips dynamics occurring in superconducting nanowires.

Chapter 1

Phase dynamics of superconducting Josephson junctions

A Josephson junction (JJ) consists of two superconductive electrodes separated by an insulating barrier of appropriate thickness, typically few nanometers, through which Cooper pairs can tunnel coherently (see Fig. 1.1). Brian Josephson[2] showed that the supercurrent I through the barrier is related to the gauge invariant phase difference φ between the phases of the two superconductors by the current-phase relationship

$$I = I_{c0} \sin \varphi \tag{1.1}$$

where I_{c0} is the critical current of the junction in absence of thermal fluctuations. In presence of a potential difference V between the two electrodes, the phase difference evolves in time as

$$\frac{\partial \varphi}{\partial t} = \frac{2eV}{\hbar} \tag{1.2}$$

Eqns. 1.1 and 1.2 are the so called Josephson equations. In a quantum-mechanical picture, the two relevant operators are φ, which is associated with the Josephson coupling energy $E_J = I_{c0} \cdot \hbar/2e$, and the Cooper-pair number difference N across the junction capacitance C, which is associated with the charging energy $E_c = e^2/2C$. Therefore in absence of dissipation,

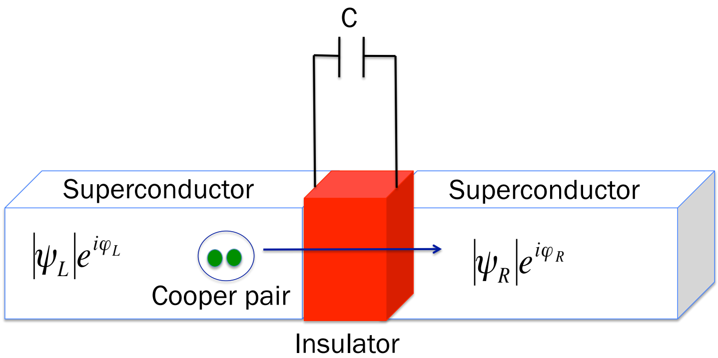

Figure 1.1: Schematic drawing of a JJ. The two superconductors are desribed by a macroscopic wavefunction $|\psi_{L(R)}|e^{i\varphi_{L(R)}}$, where $|\psi_{L(R)}|$ represents the Cooper pair density in the left (right) electrode. If the insulating barrier is sufficiently thin, such that the two wavefunctions overlap, Cooper pairs can tunnel coherently. C is the junction capacitance, which originates from the insulating layer.

the behavior of a JJ can be described by an Hamiltonian $\mathcal{H}$, which is a function of the phase difference φ and of the charge Q transferred between the electrodes[30, 37]:

$$\mathcal{H}(\varphi, Q) = E_c\,(Q/e)^2 - E_J \cos\varphi \tag{1.3}$$

As in the case of position and momentum operators x and p_x, the operators for φ and for the charge on the capacitor Q are canonically conjugate, as expressed by the commutator $[\varphi, Q] = i2e$. The fact that φ and Q are subject to Heisenberg's uncertainty principle has important consequences. When $E_J >> E_c$, φ is well defined, and Q has large quantum fluctuations; therefore, the Josephson nature of the junction dominates. On the other hand, when $E_J << E_c$, N is well defined, and φ has large quantum fluctuations; therefore, the charging nature of the capacitor is dominating[16]. In this situation the junction is known as a Cooper-pair box.

In the next two sections the phase dynamics of a JJ in the more standard condition $E_J >> E_c$ will be addressed, and dissipation arising from the environment will be discussed. Particular attention will be dedicated to macroscopic quantum phenomena and the interplay between coherence and dissipation in JJs. The phase dynamics will be studied as function of the damping of the junction and diffusive phenomena will result, as the natural consequence of very small critical currents induced by the application of nanotechnology to conventional low critical temperature (LTS) systems. The phase dynamics of unconventional superconductors, such as high critical temperature superconductors (HTS), will be compared to the phase dynamics of conventional LTS devices, with particular attention to the search of macroscopic quantum phenomena. Finally, the tools developed to study the phase dynamics in JJs will be discussed in relation to superconductive nanowires, nanostructures and hybrid devices.

1.1 Underdamped Josephson junctions

If the condition $E_J >> E_c$ is satisfied, the charging energy in Eqn. 1.3 can be disregarded. Therefore the phase difference φ is well defined and governs the dynamics of a current-biased JJ. In the framework of the Resistively and Capacitively Shunted Junction (RCSJ) model[3, 4], according to which a real junction is modelled as an ideal JJ in parallel to the junction capacitance C and a dissipative resistor R, the phase dynamics is equivalent to the motion of a particle in a washboard potential $U = -E_J(\cos\varphi + \varphi I/I_{c0})$ (see Fig. 1.2):

$$\left(\frac{\Phi_o}{2\pi}\right)^2 C\frac{\partial^2\phi}{\partial t^2} + \left(\frac{\Phi_o}{2\pi}\right)^2 \frac{1}{R}\frac{\partial\phi}{\partial t} + \frac{\partial}{\partial\phi}U = 0 \tag{1.4}$$

$\Phi_0 = h/2e$ is the flux quantum and the tilt of the washboard potential is given by the bias current I. The term involving the capacitance C represents the mass of the particle and the $1/R$ term represents the damping of the motion. For $I < 0$ the potential U has local minima where the phase particle is trapped and oscillates at the plasma frequency $\omega_p = \omega_0\,(1-i^2)^{1/4} = \sqrt{2eI_{c0}/\hbar C}\,(1-i^2)^{1/4}$, being $i = I/I_{c0}$. The strength of the friction can be

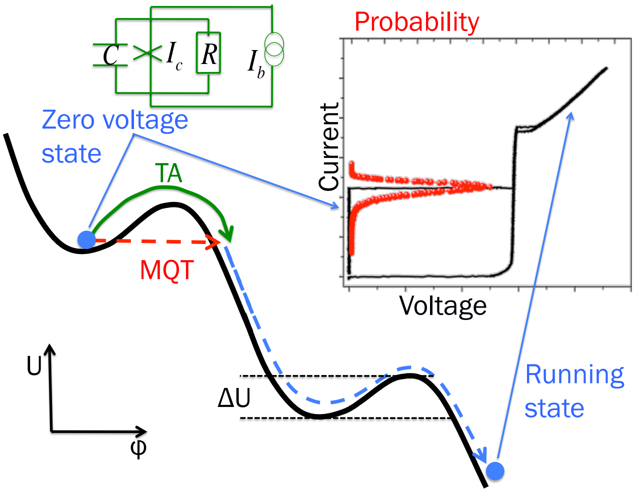

Figure 1.2: Phase dynamics of hysteretic current biased JJ. The equivalent circuit according to RCSJ model is shown on the top on the left. The top frame on the right presents an example of a measured $I - V$ characteristic of an underdamped JJ. In the superconducting state (zero voltage state) the phase is confined to one well of the washboard potential where it oscillates back and forth and the average voltage is zero. The phase particle can escape from the well either by thermal activation (TA) (green line) or macroscopic quantum tunnelling (MQT) (red dashed line) and the system switches to the free running state. The escape is a stochastic phenomenon and one can measure the distribution of the switching currents (superimposed on the $I-V$ characteristic) by repeatedly sweeping the bias current.

expressed through the junction quality factor $Q = \omega_p RC$. Therefore, the quality factor is function of the junction capacitance C, of the dissipative element R and of the critical current, which in turn is proportional to the Josephson coupling energy E_J. According to the mechanical analogy provided by the RCSJ model, low damping corresponds to $Q >> 1$, while the junction is overdamped for $Q < 1$. When ramping the bias current I, the tilt of the energy potential increases and the height $\Delta U(i) = 4\sqrt{2}/3 \cdot E_J(1-i)^{3/2}$ of the energy barrier between consecutive wells decreases. In absence of thermal fluctuations, for $I = I_{c0}$ the phase will escape from the well and roll down the washboard potential. Therefore a voltage will appear at the junction's edges. Decreasing the bias current, the potential tilt will be reduced and for $I = I_R$ the particle will be retrapped in a well, returning to the zero voltage state. Therefore I_R is known as the retrapping current. In the case of underdamped junctions, hysteresis is present in the $I - V$ characteristic and the voltage will switch abruptly from the zero voltage state to twice the superconducting gap Δ (see Fig. 1.2). Due to effects of thermal fluctuations and quantum tunneling the junction may switch to the finite voltage state for values of $I < I_{c0}$. This corresponds to the particle escaping from the well either by a thermally activated process[38] or by tunneling through the barrier potential, known as Macroscopic Quantum Tunneling (MQT)[1] (see Fig. 1.2). The relative weight of these two escape processes depends on the temperature of the system. For $k_B T >> \hbar\omega_p$ the escape process is dominated by Thermal Activation (TA) with a rate[38]:

$$\Gamma_T(i) = a_T \frac{\omega_p}{2\pi} \exp\left(-\frac{\Delta U(i)}{k_B T}\right) , \tag{1.5}$$

where $a_T = 4/[(1 + Qk_BT/1.8\Delta U)^{1/2} + 1]^2$. The escape rate will be dominated by MQT at low enough temperature [1]: for i close to one and to the lowest order in $1/Q$, it is approximated by:

$$\Gamma_q(i) = a_q \frac{\omega_p}{2\pi} \exp\left[-7.2 \frac{\Delta U(i)}{\hbar\omega_p}\left(1 + \frac{0.87}{Q}\right)\right] , \tag{1.6}$$

where $a_q = (864\pi\Delta U/\hbar\omega_p)^{1/2}$. The MQT rate is affected by dissipation, the irreversible energy transfer between the system and the environment, because of the damping dependent factor[1]. It is convenient to express the thermal and the quantum escape rate in a way that is indipendent as possible on the parameters of the junction through an escape temperature T_{esc} defined as:

$$\Gamma_{T,q}(i) = \frac{\omega_p}{2\pi} \exp\left[-\frac{\Delta U(i)}{k_B T_{esc}}\right] , \tag{1.7}$$

This is made possible because in both the classical and quantum regimes T_{esc} is very nearly independent of the bias current[14]. The crossover temperature T_{cross} between the thermal and quantum regimes is given by[39]:

$$T_{cross} = (\hbar\omega_p/2\pi k_B)\left[\left(1 + 1/4Q^2\right)^{1/2} - 1/2Q\right] \tag{1.8}$$

The behavior of the phase difference φ is deduced from measurements of the escape rate Γ from the zero-voltage state. To determine the escape rate, $10^4 - 10^5$ switching events are typically collected at fixed temperature. The resulting distribution of the switching probability $P(I)$ is used to compute the escape rate out of the zero-voltage state as a function of the bias current I[40]:

$$\Gamma(I) = \frac{1}{\Delta I}\frac{dI}{dt} ln\left(\frac{\sum_{i\geq I} P(I)}{\sum_{i\geq I+\Delta I} P(I)}\right) \tag{1.9}$$

where dI/dt is the current ramp rate and ΔI is the channel width of the analog-to-digital converter. In underdamped JJs, switching current distribution (SCD) histograms present a characteristic behavior reported schematically in Fig. 1.3. By lowering the temperature T the histograms move to higher currents and their standard deviation σ scales with the temperature down to T_{cross}. For $T < T_{cross}$, σ saturates, indicating the transition to the MQT regime. The first experiments on MQT in a JJ were carried out by Voss and Webb[7] and by Jackel et al.[8], while related experiments on a junction inserted in a superconducting loop were realized by de Bruyn Ouboter et al.[9], Prance et al.[10] and Dmitrenko et al.[11].

The temperature dependence and the effect of damping on the tunneling has been addressed by later experiments[12, 41, 42]. Devoret, Martinis and Clarke[14] have established a detailed conceptual and experimental protocol to follow to prove the macroscopic quantum nature of the phase difference across a JJ and the crossover to the thermal regime, used in most of later experiments. It has been clearly addressed the problem of the impedance presented to the junction at microwave frequencies by the wires directly connected to it, and classical phenomena have been used to measure all relevant parameters of the junction in situ[14]. The relevant parameters of the junction (critical current and shunting impedance) were determined in the thermal regime from the dependence of the escape rate Γ on the bias current and from measurements of resonant activation in the presence of microwaves[13]. The magnetic field has been used as a knob to tune the crossover temperature by changing the critical current and therefore the plasma frequency. In a further series of experiments, the existence of quantized energy levels in the potential well was demonstrated spectroscopically[14]. The escape rate from the zero-voltage state was increased when the microwave frequency Ω

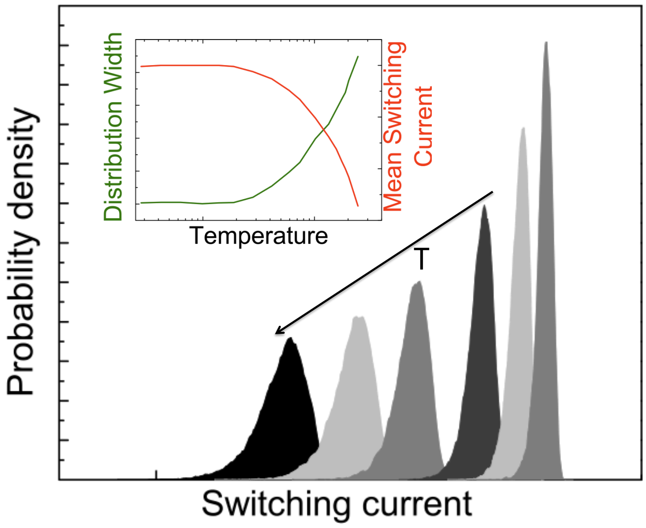

Figure 1.3: SCD histograms as function of temperature are schematized in the low damping regime ($Q >> 1$). The temperature dependence of the width and of the mean switching current are both sketched in the inset of the figure.

corresponded to the energy difference between two adjacent energy levels. A crucial point is that the anharmonic nature of the well, which results from the nonlinearity of the first Josephson equation, causes the energy spacing to decrease as the quantum number progressively increases, so each transition has a distinct frequency. The transition may involve more than one photon at once, thus called multi-photon transition, which has been observed experimentally[43]. This set of experiments clearly proved that φ is a quantum variable. Although a JJ contains a large number of atomic constituents, it is atomlike in the sense that it has a single degree of freedom behaving quantum mechanically. Thermal energy must be sufficiently low to avoid incoherent mixing of eigenstates, and the macroscopic degree of freedom must be sufficiently decoupled from other degrees of freedom for the lifetime of the quantum states to be long on the characteristic time scale of the system[1].

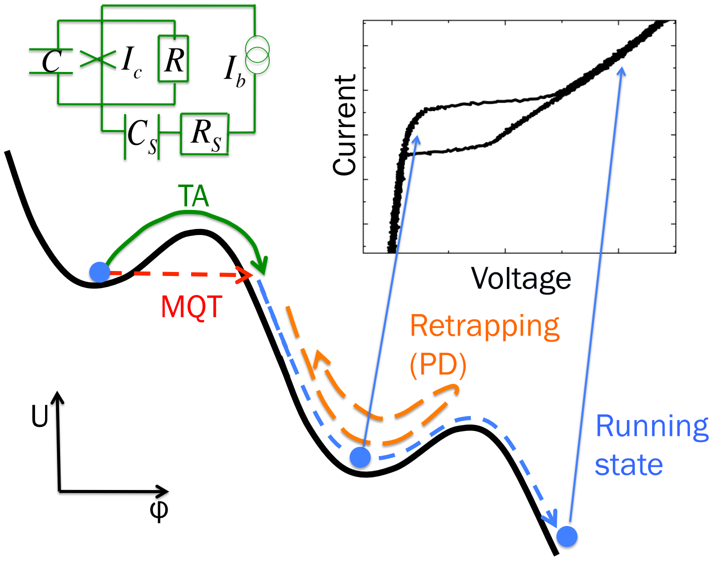

Figure 1.4: Phase dynamics of small area JJ[31]. The equivalent circuit in the framework of freqency dependent RCSJ model is shown on the top on the left. Due to onset of multiple escape and retrapping processes, at low bias the phase particle diffuses along the tilted washboard potential, until an increase of the tilt raises the velocity and the phase particle can switch to the running state. $I-V$ characteristics display both hysteresis and a phase diffusion branch at small voltages.

1.2 Moderately damped regime

In underdamped junctions, a single escape event is enough for the junction to switch to the running state. This occurs since the kinetic energy gained by the phase particle running down in the tilted washboard potential is not all dissipated, but enough energy remains to carry the phase over the next "hill". In the case of overdamped junction ($Q < 1$), following an event of escape the particle may travel down the potential for a few wells and then is retrapped in one of the following minima of the potential. At low bias the process of escape and retrapping may occur multiple times generating diffusion of the phase until an increase of the tilt of the potential, due to a change in the bias current, raises the velocity of the particle and the transition to the running state occurs. The competition between multiple escape and retrapping processes prevents the access to the running state and leads to the appearance of a non zero voltage, manifesting as a phase diffusion branch in the $I-V$ characteristic[3, 30, 31]. Therefore in the overdamped regime the $I-V$ characteristic is non hysteretic with a distinctive resistive branch at low voltages and the transition to the running state is no longer a stochastic phenomenon. The analytical expression for the retrapping rate from the resistive to the superconducting state is given by[44, 45]:

$$\Gamma_R(I) = \omega_0 \frac{I - I_{R0}}{I_{c0}} \sqrt{\frac{E_J}{2\pi k_B T}} \exp\left[\frac{-E_J Q_O^2}{2k_B T}\left(\frac{I - I_{R0}}{I_{c0}}\right)^2\right] \tag{1.10}$$

where I_{R0} is the fluctuation-free retrapping current, ω_0 and Q_O are the plasma frequency and quality factor for $I = 0$ respectively. In 1990 Martinis and Kautz[31], following the works of Ono et al.[29], have shown both experimentally and theoretically that hysteresis and phase diffusion (PD) can coexist in small area JJs. In such junctions, the critical current is a few nA (with a critical current density $J_c \approx 10 A/cm^2$) and E_J is of the order of the thermal energy $k_B T$. The coexistence of hysteresis and PD could be explained in the framework of the RCSJ model if frequency dependent damping is taken into account. In fact in a typical experimental setup, the junction is also capacitively and resistevely shunted by the leads attached to the junction itself. A more realistic equivalent circuit of the junction is thus that presented in Fig. 1.4 rather than the simple RCSJ model of Fig. 1.2.

At low frequencies, the dissipation is mostly determined by the junction resistance R, but at high frequencies (usually ω_p is of the order of 10 GHz) the impedance is typically small because C_s acts as a short and R_s is small compared to R. In the zero voltage state, the phase oscillates in a well at the plasma frequency and it may transit from one well to another in a time which is of the order of the inverse of the plasma frequency. The dissipation is thus characterized by $R(\omega \approx \omega_p)$ in this case. Without a specially designed environmental circuit, this high frequency dissipation is usually of the order of the impedance of the leads ($\approx 100\Omega$). After the switching to the running state, dissipation takes place at low frequencies ($\omega \approx 0$) so that junctions are overdamped at high frequencies but are in the underdamped limit at low frequencies respectively[31].

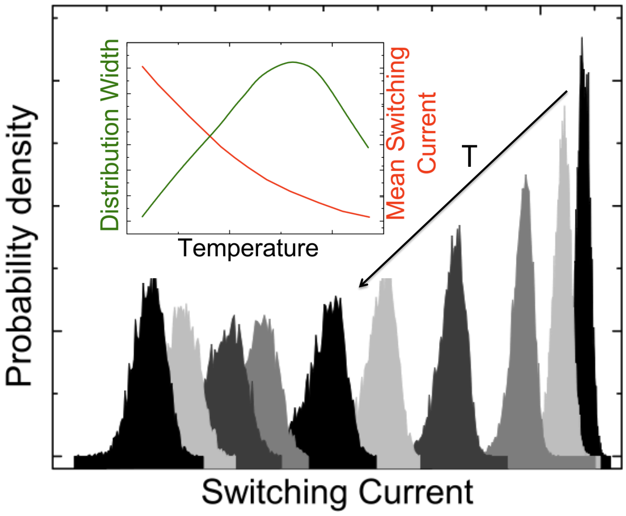

Figure 1.5: SCD histograms are schematized as function of temperature in the moderately damping regime. The temperature dependence of the width and of the mean switching current are both reported in the inset of figure. This behavior is qualitatively quite different when compared to the underdamped case, providing distinct signatures of the phase dynamics.

PD has reappeared from a different perspective in 2005 in magnetometers with much larger and unshunted junctions used for qubits readout[34, 35]. In such junctions I_c ranges from a few hundreds nA to a few μA ($E_J >> k_B T$), and they fall in the moderately damped regime (MDR) ($1 < Q < 5$). The $I-V$ characteristics are hysteretic and the transition to the running state is a stochastic phenomenon. In addition to the usual crossover between MQT and TA behavior, measurements of SCD have showed the transition from TA to the PD regime, resulting in a more diversified (k_BT, E_J) phase diagram[35]. This translates in a characteristic dependence of σ, as the appearance of an anticorrelation between the temperature and the width of the switching distributions[34, 35, 36, 46, 47, 48, 49]. After the MQT saturation at the lowest temperatures, σ follows the expected $T^{2/3}$ dependence, deviations are evident in proximity and above a transition temperature T^* that is defined as the temperature at which the width σ of the SCD reaches the maximum value. Above T^* histograms tend to become more symmetric and shrink

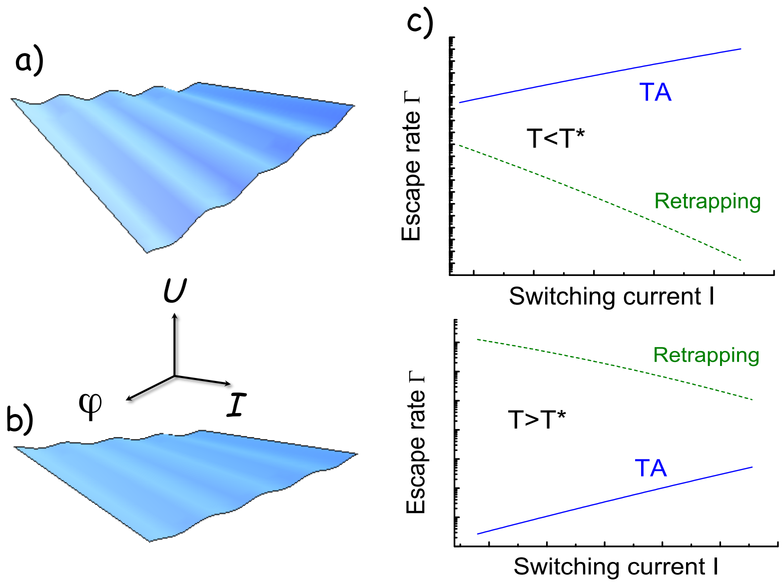

Figure 1.6: (a) 3-dim view of the washboard potential as a function of the phase and of the bias current. The current spans from 0 to I_c. In (b) E_J is half of the value used in (a), and this favors the PD regime (see text). (c) Schematic representation of thermal Γ_T and retrapping Γ_R escape rates at $T < T^*$ (top panel) and at $T > T^*$ (bottom panel)[50].

rather than broaden with a consequent increase of their maximum (see Fig. 1.5). The change in the sign of the derivative of σ and a modification of the shape of the distributions at temperature around T^* turn to be distinctive signatures of the PD regime. As showed by Fenton and Warburton[50], the anomalous thermal behavior of the SCDs in the MDR could be explained considering the competition between thermal escape and multiple retrapping processes in the switching dynamics. For $T < T^*$, thermal escape dominates on the retrapping rate, differently from the case $T > T^*$, as schematically shown in Fig. 1.6c.

As it can be seen in Fig. 1.4, the diffusive regime is characterized by the onset of multiple retrapping processes in subsequent potential wells. As roughly sketched in Fig. 1.6 and by the equation 1.10, a decrease of the Josephson energy E_J and of the quality factor Q enhances the retrapping probability Γ_R, causing multiple retrapping phenomena in the switching dynamics. For LTS systems, once the barrier thickness and the J_c have been fixed, a reduction in its size unavoidably leads to a lowering of the critical current and determines a quite different phase dynamics "re-normalized" to the new scaling energy[30, 31, 34, 35, 48]. Lower critical currents result in lower Josephson energies, and higher levels of dissipation are expected. The range of the energy dynamical parameters is significantly enlarged, and it is technologically easier to reproducibly realize not trivial configurations. The possibility to reproducibly achieve low I_c in submicron junctions has promoted studies on moderately damped junctions. The same regime can be controllably induced in larger junctions in case of low J_c[47, 49], or with lower reproducibility in junctions with larger intrinsic dissipation levels, as occurring in HTS systems[36, 46], which will be addressed in the next section. These devices are characterized by intermediate levels of dissipation and by PD phenomena. The low J_c limit seems to be characteristic also of all futuristic nano-hybrids devices incorporating nanowires, and the moderately damped regime is intrinsically more common than it could be expected[32, 33].

1.3 HTS Josephson junctions: grain boundary junctions

HTS oxides enlarge the occurrence of superconductivity to unexpected energy (superconducting gap $\Delta \approx 20$meV) and length scales (coherence lenght $\xi \approx 1$nm). This is true also for the Josephson effect. Dimensionality, strong correlations, d-wave order parameter (OP) symmetry (see Fig. 1.7) will represent the fundamental ingredients which contribute to define the properties of HTS. As a matter of fact, in the last thirty years HTS have opened the new horizons of unconventional superconductivity.

Because of the difficulties in producing a traditional tri-layer structure (superconductor - insulator (normal metal) - superconductor, S-I (N)-S) composed by HTS electrodes[23, 51], in analogy to LTS junctions, alternative types of junctions have been developed. The HTS junctions are described in extensive reviews[23, 51]. Here the main concepts of the junctions employed in the experiments described in the following are outlined. Grain boundary (GB) junctions have been largely used in HTS compounds. They take advantage of a significant reduction of the critical current between two grains

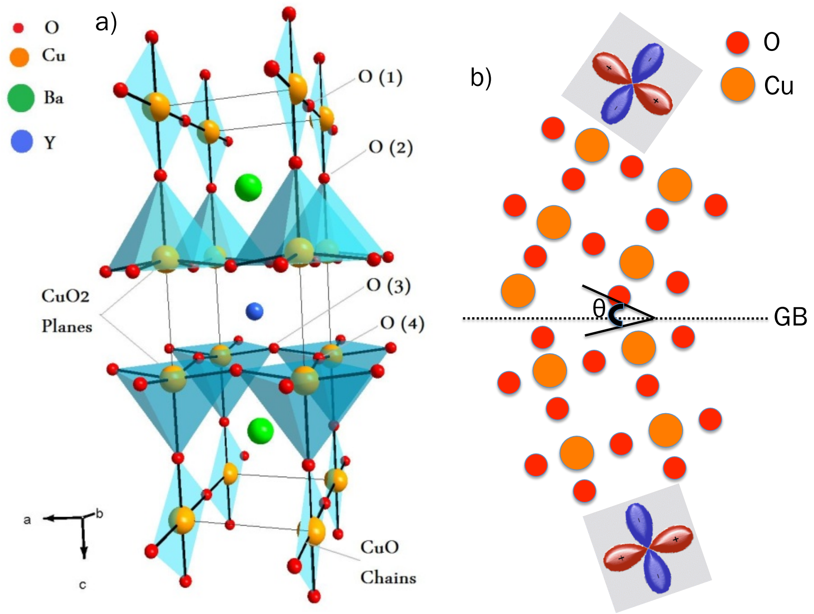

Figure 1.7: (a) Crystal structure of $YBa_2Cu_3O_{6+x}$. CuO_2 planes and CuO chains are both highlighted. (b) Schematic drawning of grain boundary between two d-wave superconductive electrodes. θ indicates the misorentation angle.

with different orientations which generates weak coupling and Josephson-like behavior between the two electrodes. The bicrystal technique, based on the union of two substrates with different crystal orientations, is the most direct way to create a GB[52]. The HTS films, if they grow epitaxially, will reproduce the relative orientations of each of the two substrates.

Bicrystal imposes junctions on specific locations determined by how the substrates are glued. Methods to locate GB junctions everywhere on a chip were offered for HTS by the step, step-edge and biepitaxial techniques, all employing photholithographic means to define the GB interfaces[23, 51]. The biepitaxial technique for instance uses changes of the orientation of HTS films induced by epitaxial growth on structured template layers. In the original technique[53], a MgO template layer on a r-plane sapphire produces an in-plane rotation by 45° of a $SrTiO_3$/YBCO bilayer compared to an identical bilayer grown directly on the sapphire, producing a GB with a 45° tilt around the [001] direction. The biepitaxial technique has been extended to novel configurations, in which one of the electrodes does not grow along the c-axis orientation[54]. A schematic representation of GB biepitaxial JJs is shown in Fig. 1.8. A specific feature of these structures is the use of a [110]-oriented MgO or CeO_2 buffer layer, deposited on [110] $SrTiO_3$[54] or $(La_{0.3}Sr_{0.7})(Al_{0.65}Ta_{0.35})O_3$ (LSAT) substrate[55]. YBCO grows along the [001] direction on the MgO and on the CeO_2 seed layers, while it grows along the [103]/[013] direction on the substrates. The presence of the CeO_2 produces an additional 45° in-plane rotation of the YBCO axes with respect to the in-plane directions of the substrate. As a consequence, the GBs are the product of two 45° rotations, a first one around the c-axis, and a second one around the b-axis. Atomically flat interfaces can be achieved in appropriate conditions[54], as a result of an opportune "self-assembling" growth mode. The tilt of one of the electrodes and the in-plane 45° rotation on the CeO_2 both contribute to decrease the barrier transmission, while the in plane rotation enhances on demand the desired d-wave features. These types of junctions have been used for the macroscopic quantum tunneling experiments[24, 25, 56] discussed in the next section.

GBs have been used for several corner-stone experiments on HTS junctions [6, 23, 51]. The possibility to span over 4 orders of magnitude in J_c by selecting specific misorientation angles in GB junctions remains as one of the most significant advantages. This is mostly ruled by the d-wave OP symmetry and by the GB microstructure. We can have on one hand large J_c values for relatively low misorientation angles, which allow studies on static and dynamical effects associated to half flux quantization. On the other hand J_c values of the order of 10^2 A/cm^2 lead to junctions with hysteretic behavior in the current-voltage characteristics, which have permitted the experiments on macroscopic quantum phenomena in HTS systems. It is important to recall that the tunnel limit, as commonly reported for traditional LTS JJ, has never been achieved for HTS junctions based on thin film technology. The expression 'tunnel-like' is commonly used to indicate HTS junctions characterized by a significant hysteretic behavior in the $I-V$ curves, with critical currents typically not larger than a few μA and normal state resistance (R_n) not lower than a few hundreds Ω for micron size junctions with thickness of the thin film of about 100-200nm. Such junctions represent a minority among the data available in literature.

Probably the most convincing evidence for a predominantly d-wave OP symmetry in the cuprates has come from phase sensitive tunneling measurements [6, 57, 58, 59]. Evidence from other types of measurements have been extensively discussed in[6]. After the first two phase sensitive tunneling demonstrations of the d-wave nature of the OP symmetry in HTS[6, 58], other experiments still employing JJs have confirmed the effectiveness of a predominant d-wave OP symmetry[60]. The whole set of experiments now constitutes a solid background[6, 23, 51, 57] whose methodology and procedures can be extended to junctions composed of whatever type of materials. Such methodology does not apply only to unconventional materials, where it would make sense to look for 'exotic' OP symmetry, but also for instance to junctions with ferromagnetic barriers, whose unconventional phenomenology also funds on the notion of π-phase shift[61, 62, 63, 64].

The general expression of the current-phase relationship, which takes into account current components carried by multiple reflection processes at the junction interface and effects related to possible anisotropic OP symmetry, is[65, 66, 67]:

$$I(\phi, \theta_1, \theta_2) = \sum_{i \geq 1} (I_n(\theta_1, \theta_2) \sin(n\phi) + J_n(\theta_1, \theta_2) \cos(n\phi)) \tag{1.11}$$

where θ_1 and θ_2 are the angles of the crystallographic axes with respect to the junction interface of the left and right electrodes respectively. The I_n contribution depends on the barrier transparency as a $\overline{T}^n$ power-law and corresponds to the n-multiple reflection process. On the basis of general symmetry arguments, for two generalized d-wave superconductors in the case of time reversal symmetry J_n=0, to the lowest order, the well known Sigrist-Rice formula is found in the clean limit[68]:

$$I(\varphi, \theta_1, \theta_2) = A_S[\cos(2\theta_1)\cos(2\theta_2)] \cdot \sin(\varphi) \tag{1.12}$$

The dirty limit expression when disorder effects and faceting are taken into account, is given by:

$$I(\varphi, \theta_1, \theta_2) = A_S[\cos(2\theta_1 + 2\theta_2)] \cdot \sin(\varphi) \tag{1.13}$$

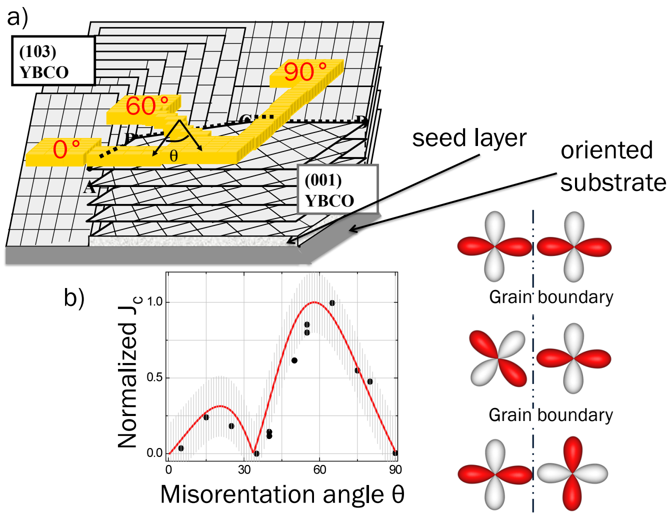

Figure 1.8: (a) Schematic drawing of GB biepitaxial structure for three different interface orientations $\theta = 0°$, $60°$ and $90°$. Mgo or CeO_2 seed layer grows on the oriented $SrTiO_3$ or LSAT substrate, YBCO grows along the [001] direction on the seed layer while it grows along the [103] direction on the substrate. (b) Normalized J_c (black points) as function of the interface orientation is shown for a set of GB biepitaxial JJs, compared with the Sigrist-Rice formula (red line, Eqn. 1.13). On the right, different GB configurations are shown: J_c has a maximum in the lobe-lobe configuration, while the minima occur at the lobe-node configuration. Finally, a change in the sign of the current occurs if a positive lobe faces the negative one (adapted from [60]).

In these expressions a negative supercurrent can be translated as a phase shift of π at the junction[69]. Particular choices of θ_1 and θ_2 (for instance with misorientation of 45° in GB junctions) can also make the $\sin(\varphi)$ component negligible, as shown in Fig. 1.8. Higher order corrections in the current-phase relationship can lead to important modifications for d-wave superconductors. The free energy can be expressed as:

$$F_J = -\Phi_0/(2\pi c)|I_1|\cos(\varphi - \varphi_0). \tag{1.14}$$

which is not invariant under time reversal. The intrinsic phase shift is φ_0, which corresponds to a two-fold degenerate state which breaks time reversal symmetry. A direct consequence of time reversal symmetry breaking can be seen in the presence of spontaneous supercurrents and the possibility of vortices with fractional flux quanta[68]. Again these concepts extensively studied for HTS[6, 23, 68] are of general relevance for all exotic superconductors, and recently also for systems aimed to the detection of Majorana fermions[70, 71, 72]. In addition, an intriguing merging between the physics of Majorana bound states and d-wave JJs, with their additional intrinsic possibility of manipulating the phase[73], comes into play. Deviations from the sinusoidal behavior are relevant for weak links in the ballistic case at low temperatures and for highly transmissive barriers[4, 74]. Issues related to the current-phase relationship for different types of junctions have been extensively discussed in the review by Golubov, Kupryanov and Ilichev[75].

1.4 Macroscopic quantum phenomena in HTS based Josephson junctions

The idea that performances of qubits could be improved and optimized by a suitable design of the ensemble qubit-circuit was accompanied by the awareness that some limits on coherence are imposed by intrinsic dissipation due to the 'chemistry' of the junctions, of the barrier interfaces and of the materials composing them. Progress in engineering new materials into junctions and in understanding and more and more controlling the physics of interfaces may offer novel solutions for junctions of superior quality and complementary functionalities, and therefore may lead in the long run to improve specific qubit performances. In other words, material science could contribute to develop solutions for hybrid systems for quantum computation. Experiments on macroscopic quantum behavior have been extended to novel types of structures and materials. Measurements of SCD in these last years have turned to be standard tools to investigate phase dynamics in unconventional and hybrid systems and nanostructures. HTS are an example of unconventional systems, because of the d-wave OP symmetry and of the presence of low energy quasi-particles[6], which are expected to induce high level of dissipation and as a consequence to spoil macroscopic quantum coherence. The first examples of unconventional systems are given by HTS devices[23], biepitaxial GB YBCO JJs[24, 25] and a variety of intrinsic junctions, built on high quality single crystals[26, 27]. HTS may be an interesting reference system for novel ideas on key issues on coherence and dissipation in solid state systems because of their unusual properties[6, 76]. Low energy quasiparticles have represented since the beginning a strong argument against the occurrence of macroscopic quantum effects in these materials. Quantum tunneling of the phase leads to fluctuating voltage across the junctions, which excites the low energy quasi-particles specific for d-wave junctions, causing decoherence. Contributions to dissipation due to different transport processes, such as channels due to nodal quasi-particles, midgap states, or their combination, have been identified and distinguished[75].

The search of macroscopic quantum effects has become feasible once high quality HTS JJs with significant hysteresis in the $I - V$ characteristic were available. Two classes of experiments, which are based on two different complementary types of junctions, have been performed: 1) MQT and energy level quantization (ELQ)[24, 25] on off-axis YBCO grain boundary biepitaxial JJs, where the experiment has been designed to study d-wave effects with a lobe of the former electrode facing the node of the latter; 2) MQT and ELQ on intrinsic Josephson junctions (IJJ) on single crystals of different materials[26, 27], where d-wave OP symmetry is expected to play a minor role[75]. The experiments using GBs are more complicated because of the complexity of these junctions, but are very complete and allow to address relevant issues on the effects of a d-wave OP symmetry on dissipation and coherence. In HTS JJs, when a lobe of the OP symmetry on one side of the junction meets a lobe on the other side, a larger J_c is measured, differently from the case of a lobe facing a node[6, 23, 51, 60] (see Fig. 1.8). If we produce d-wave junctions with different interface orientations, as for instance made possible by the biepitaxial technique, a wide range of different OP symmetry configurations are realized, representing an additional knob to tune phase dynamics. The interest for phase dynamics intrinsically encoded in the GB cannot be disjointed from the general problem of understanding dissipation in systems with very low energy and potentially highly dissipative quasi-particles, as occurring in d-wave systems. The GB biepitaxial junctions[54] used in[24, 25] had reproducible hysteretic behavior up to 90%. The junction in the tilt configuration (angle θ=0°) turns out to be the most interesting case for the MQT and ELQ experiments. This lobe to node configuration maximizes d-wave induced effects[60] and allows to explore the effects of low energy quasi-particles. The SCDs as a function of temperature substantially follow what commonly measured on LTS JJs, with a saturation of the measured σ below 50 mK[24], which corresponds to the crossover temperature from the thermal to the MQT regime and is consistent with the predicted values. The change of T_{cross} through an external magnetic field is an important confirmation of the occurrence of MQT. Values of $R \simeq 100\Omega$ and $C \simeq 0.22$pF can be obtained from the measurements with a plasma frequency $\omega_p/2\pi \simeq 2.6$GHz and a quality factor of the order of 10[25, 77]. C-axis tilt is mostly responsible for low barrier transparency and leads to the presence of a significant kinetic inductance in the modeling of YBCO JJ. In these junctions the presence of a kinetic inductance and a stray capacitance determine the main difference in the washboard potential making the system behavior depending on two degrees of freedom[25, 77]. The YBCO JJ is coupled to this LC-circuit and the potential becomes two-dimensional.

The layered crystal structure with strongly anisotropic properties in HTS allows another "unique" type of junction called intrinsic stacked junctions. These junctions mostly exploit c-axis transport. Most successful results have been achieved in $Bi_2Sr_2CaCu_2O_8$[78] and $Tl_2Ba_2Ca_2Cu_3O_{10}$ single crystals and thin films[79, 80]. In these junctions the nodes of the d-wave OP are not expected to affect significantly MQT. Experiments on $Bi_2Sr_2CaCu_2O_8$ IJJs[26, 27] have been aimed to increase T_{cross} and to clarify the nature of IJJs, rather than raising novel themes of coherence in d-wave systems. Josephson coupling between CuO_2 double layers has been proved, and most of the materials behaved like stacks of S-I-S JJs with effective barriers of the order of the separation of the CuO_2 double layers (1.5nm) (J_c typically 10^3 A/cm^2)[81]. IJJs have a much higher Josephson coupling energy than GB junctions, the $I-V$ curves exhibit large hysteresis and multiple branches, indicative of a series connection of highly capacitive junctions. Practical realizations of IJJ have been designed in order to nominally avoid heating effects[36, 79]. However, at high voltages caution is required when extracting information because of possible unavoidable heating problems. T_{cross} has been reported to be about 800mK, remarkably higher than those usually found in LTS systems. By using microwave spectroscopy, the unique uniform array structure of IJJ stacks have been considered responsible for a remarkable enhancement of the tunneling rate[27]. This enhancement adds a factor of approximately N^2 to the quantum escape rate of a single JJ, also resulting in a significant increase of T_{cross}, where N is the number of the junctions in the stack. This effect can be caused by large quantum fluctuations due to interactions among the N junctions[27].

1.5 Switching processes in nanostructures

Measurements of SCD have recently performed on a series of different nano-structures. Some of them are junctions and then can be easily classified in the schemes described above, and more specifically in the MDR. Some of them are simple nanowires. A subtle path exists between these different systems with analogies and distinctive features. When considering that a micro-bridge of width of the order of the coherence length behaves as a JJ[3, 4], measurements of SCD will turn to be a direct way of discriminating the phase dynamics and the transport in non trivial cases, which are going to be more and more common with advances in nano-patterning superconductors at extreme scales.

Supercurrent passes in graphene sheets comprised in between superconducting electrodes[28]. This is one of the nanostructured proximity-coupled Josephson systems based on conducting spacers, able in principle to be electrically tuned. Other SCD measurements are realized on nanowires[82, 83], carbon nanotubes[84, 85] and nanocrystals[86]. In Lee et al. [28], graphene is attached to PbIn electrodes separated by a trench of 300nm. PbIn superconducting electrodes significantly enhances the critical current compared with commonly used Al (as high as 6μA in highly doped regions). The crossover from the classical to quantum regime is controlled by the gate voltage and has been found surprisingly high, of the order of a few hundreds mK. Q factor is about 5-6 for all voltages. Capacitance is for instance about 35fF at V=$-$60V and seems to be not related to self-heating[87] but consistent with an effective capacitance $C_{eff} = \hbar/R_n E_{th}$ due to diffusive motion of quasiparticles in graphene[88] (E_{th} is the Thouless energy). Phase diffusion regime has been found for all gate voltages with T^* ranging from about 1K (V=0) to 2K (V=$-$60V).

Stochastic dynamics of superconductive-resistive switching in hysteretic current-biased superconducting nanowires undergoing phase-slip fluctuations is a topic of growing interest. Recent studies have reported phase-slip induced switching in superconducting nanowires[89, 90]. In $Mo_{79}Ge_{21}$ nanowires of lenght ranging from 100nm up to 200nm[89], measurements of SCD have been used to investigate the behavior of individual quantum phase-slip events in homogeneous ultranarrow wires at high bias currents, observing a monotonic increase of σ with decreasing temperature. In Al nanowires[90] of width less than 10nm and length ranging from 1.5 to 10μm (with critical currents of the order of a few μA), fluctuations in the average critical current exhibit three distinct regions of behaviors and are nonmonotonic in temperature. Saturation is present well below the critical temperature T_c, an increase occurs as $T^{2/3}$ at intermediate temperatures, and a collapse is present close to T_c. The relationship between individual phase-slips and switching has been also theoretically investigated[91] in order to provide a tool to study phase-slips, to help establish whether they are caused by thermal fluctuations or by macroscopic quantum tunneling[92]. It has been found that although several phase-slip events are generally necessary to induce switching, there is an experimentally accessible regime of temperatures and currents for which just one single phase-slip event is sufficient to induce switching, via the local heating it causes.

Chapter 2

Experimental setup

The challenging search of macroscopic quantum effects and a comparative study of phase dynamics and dissipation in different Josephson systems requires very low temperatures, high resolution measurement setup and very low noise environment. Therefore, the design of a measurement setup that allows to minimize the effects of noise and coupling from the environment becomes crucial. The experimental setup described in this chapter is designed to reduce noise as much as possible and allows measurements down to the quantum regime in very different systems with excellent reproducibility.

The first section of this chapter is dedicated to the description of the dilution unit and its equipment, with particular attention to the improvements made during this work. Great efforts have been dedicated to noise reduction, to shielding from external magnetic field and to the thermal coupling of the sample to the cooling unit. In the second section, the measurement procedures used to investigate the escape dynamics of the Josephson devices will be described, along with the low noise-high resolution electronic apparatus. Finally, the flexibility and the performances of such measurement setup will be highlighted by examples of measurements of thermal and magnetic properties of different systems, such as oxide-based interfaces and hybrid structures.

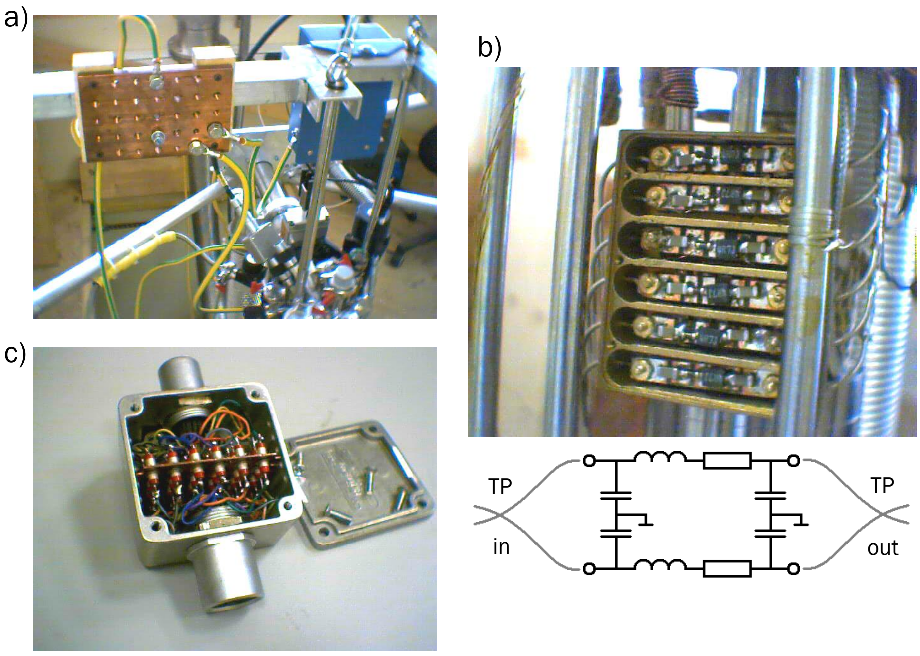

Figure 2.1: a) Ground plate on the top of the cryostat. b) Picture (top) and circuit diagram (bottom) of the mounted RCL-Pi-filter at the 1K-plate. Since the wiring is in twisted pair configuration, there are two filter PCBs in one chamber. c) Filter box with 24 channel EMI filters.

2.1 Dilution fridge

The measurements reported in this work have been carried out using a specifically designed dilution cryostat shielded against external magnetic field and radiofrequency noise. The dilution fridge is a Kelvinox MX400 made by Oxford Instruments and uses a mixture of ^{3}He -^{4}He to reach a base temperature of a few mK. In the following, the efforts made for noise reduction, for a better control of the dilution unit and to improve the performances of the experimental procedure will be described.

One of the most important pre-requisites for high quality low noise measurements at low temperatures is an excellent electrical ground. For this purpose, a separate strong ground connection line has been installed (cross-section= $75mm^2$) and all delicate devices have been connected to it (see Fig. 2.1.a). Filters systems have been installed and thermally anchored at different stages of the dilution unit. In a first step a box with 12 miniaturized Pi-style RCL-filters have been installed at the 1K-plate ($T \simeq$1.7K, see Fig. 2.1.b). The used elements (two capacitors of 100nF, one resistor of 100Ω and one inductor of 4.7μH) have been tested at low temperatures before being installed. The cut-off frequency of these low-pass filters is about 100kHz. The main advantage of this type of filter is the possibility of filtering a large number of lines in a small volume. The wiring from room temperature stage to the RCL-Pi-filters consists of 12 twisted pairs (TP), and every pair is shielded by a German silver tube with 0.8mm outer diameter. The material of the wires is both manganin (9 pairs) and copper (3 pairs), with Formvar isolation and a bare diameter of 0.1mm. Manganin is an alloy composed by copper, manganese and nickel; it is widely used in cryogenic measurements since at low temperature its thermal conductivity is two orders of magnitude less than the copper one. Therefore, manganin wires have been chosen to reduce the heat load to the refrigerating system for most of the lines, while copper wires have been chosen for the current-carrying lines to avoid excessive heating, because of the higher resistivity of manganin. German silver, which is a copper, nickel and zinc alloy, has been chosen for its low thermal conductivity. From the 1K-plate to the mixing chamber stage niobium-titanium superconducting wires have been used. The critical temperature of this alloy is 11K. The superconducting wiring allows to bias the samples with high currents without risking excessive heating.

For a sufficient suppression of electromagnetic high frequency peaks, coming for example from mobile phones, a 24-channel filter box with electromagnetic interference (EMI) filters has been realized (Fig. 2.1.c) and mounted at the entrance of the cryostat at room temperature. The RCL-Pi-filters installed at the 1K-plate are subject to a significant loss in attenuation at frequencies higher than 1MHz due to the parasitic inductance of the capacitor[93]. Therefore this type of filters does not work well against noise at frequencies in the GHz range and above. Further filtering is provided by a combination of copper powder[94] and twisted pair filters[95]. Two stages of copper powder filters have been realized, the first thermally anchored at the cold-plate ($T \simeq$0.05K, see Fig. 2.2.b), the second thermally

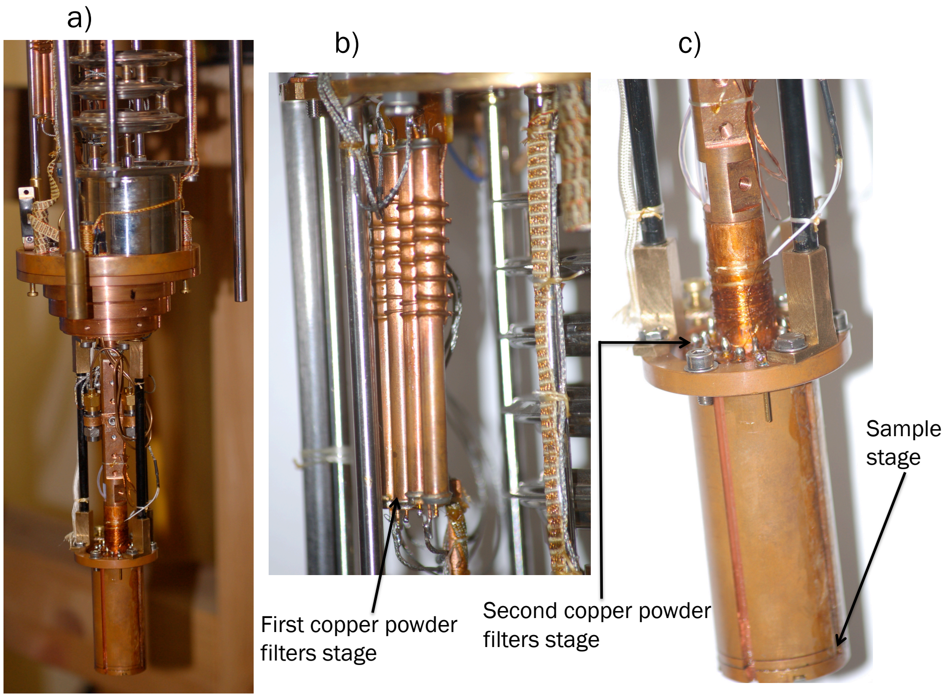

Figure 2.2: a) Picture of the last stage of the dilution cryostat, including the heat exchangers, the mixing chamber and the sample stage. b) First stage of copper powder filters thermally anchored at the cold-plate. c) Picture of the second copper powder filters stage and of the sample stage. The pins of the copper powder filters, to which the lines have been soldered, are indicated by the black arrow.

anchored at the mixing chamber (Fig. 2.2.c). They are realized with a spiral coil of insulated wire inside a tube filled with copper powder with a grain size ranging from 5 to 30μm. Since each grain of the powder is insulated from its neighbours by a naturally grown oxide layer, the effective surface area is enormous[96, 97]. The filter attenuates an incoming electrical signal via eddy current dissipation in the metal powder. The cut-off frequency of this type of filters is in the range of a few GHz.

The sample is mounted at the bottom of the mixing chamber (see Fig. 2.2), on a chip holder electrically connected to the control electronics. The chip holder has copper pads to which the junctions are connected with alu-

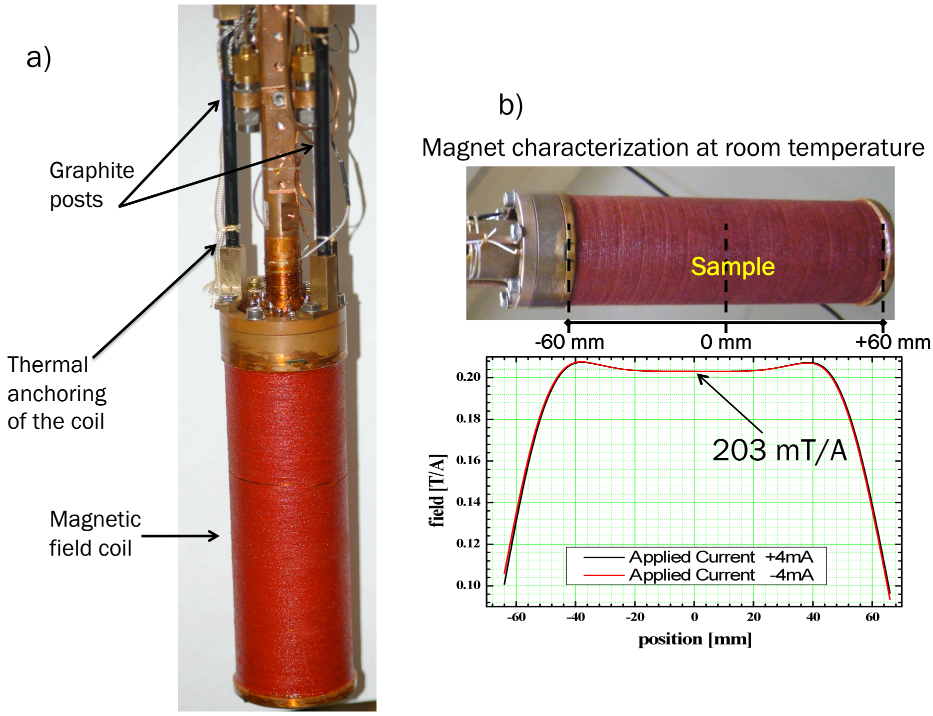

Figure 2.3: a) Picture of the Nb-Ti coil. The coil is mechanically anchored to the mixing chamber (not shown in the picture, see Fig. 2.2) through graphite posts, which at the same time provide thermal isolation between the coil and the mixing chamber. Thermal anchoring to the still plate is provided by copper wire shielded with insulating twist. b) Characterization of the coil at room temperature. The conversion factor between the current flowing in the coil and the magnetic field generated is 203mT/A.

minium wire, bonded with commercially available bonder machine.

The refrigerator is also equipped with a solenoid for the generation of magnetic field. A superconducting Nb-Ti wire has been used for the windings in order to generate fields up to about a few hundreds of mT with low heating. For standard micron size junctions, these fields are enough to fully characterize the magnetic performances of junctions and superconducting quantum interference devices (SQUIDs). In view of measurements on mesoscopic samples and junctions and on thin films, the coil supports higher currents and magnetic fields. The upper limit in H is suggested by the need of avoiding heating and magnetization of the sample holder and thus remnant fields, which usually occur when relatively high fields are applied. As shown by the magnet characterization at room temperature in Fig. 2.3.b, an important feature of the coil is the high uniformity of the generated field. The sample is mounted inside the solenoid at $x = 0$. For $-20\text{mm} < x < 20\text{mm}$, the field variation is of the order of 10^{-3} T/A. The conversion factor between the current flowing in the coil and the magnetic field generated has been checked at low temperatures. Finally, in order to reduce heating and thermal load to the mixing chamber, the coil is thermally linked to the still plate of the dilution cryostat through a copper wire shielded with insulating twist. Mechanical anchoring to the mixing chamber is provided by graphite posts (see Fig. 2.3.a) which at the same time provide thermal insulation between the coil and mixing chamber.

All the measurements that will be shown in this work have been realized in a magnetically shielded environment. The shielding was provided by a system of superconducting and cryoperm screens. The screen system is composed by a cryoperm shield 1mm thick as an external screen, a lead shield of 1mm and a μ-metal shield of 0.1mm in the inner section. If only the superconducting screens were present, during the cool down of the screens the external magnetic field (as for example the earth magnetic field and the fields produced by electronic equipments) would be frozen inside the superconductors. Therefore, the cryoperm shield is added as an external screen. On the other hand, a screening system made only with cryoperm would not be feasible, since the high magnetic fields produced by the coil would magnetize the material.

2.2 Electronic setup

The search of macroscopic quantum phenomena in superconducting junctions and an accurate measurement of the Josephson properties require specifically designed and optimized low noise electronic setup. Fig. 2.4.a shows a block diagram of the experimental setup including both room temperature electronic and the whole filtering system. The room temperature circuits have been optimized to minimize the effect of unwanted noise. In order to

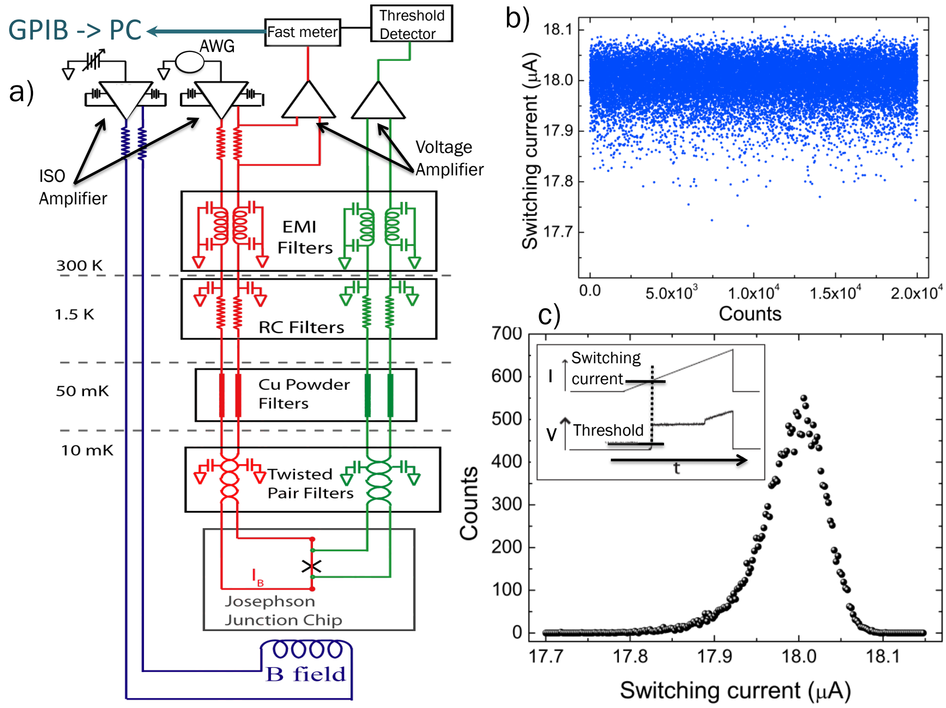

Figure 2.4: a) Schematic of the measurement electronics including the various stages of filtering. Such setup has been used for measurements of SCD. b) and c) show the raw data and the corresponding switching histogram respectively, measured on a niobium JJ at the base temperature of 20mK. In the inset, voltage and current signal sequence, along with the voltage threshold and the corresponding switching current, are illustrated.

avoid ground loops and noise pick up, the whole experiment is designed to have a single ground[98, 99]. All connections to the sample are floating and are only capacitively coupled to ground through the filters. All grounded signal sources pass through battery powered unity gain isolation amplifiers (ISO amplifiers, see Fig. 2.4.a) that effectively disconnect the signal from the earth ground. The current paths are all designed to be symmetric with respect to the sample to reduce the effect of common mode noise[100]. This allows for sufficient decoupling from the ground, and at the same time the amplifiers are keeping far from saturation, due to charging, since a return current path is provided. The amplifiers are designed to have 100MΩ of resistance between their inputs and the ground of the battery circuit. All signals entering the fridge are isolated, shielded, and filtered, thus making the dilution refrigerator an RF shield for the cold portion of the experiment.

In order to investigate the phase dynamics of underdamped and moderately damped JJs, the signal from Stanford Research DS345 arbitrary waveform generator (AWG) goes through an isolation amplifier to a bias box consisting of biasing and monitoring resistors. The voltage across the monitoring resistor is sensed by a voltage amplifier operating in differential mode. The voltage from the sensing amplifier is measured using HP Agilent 3458A fast multimeter. The bias current of the junction is ramped at a constant sweep rate, the voltage is measured using a low noise differential amplifier and is fed into a threshold detector which is set to generate a pulse signal when the junction switches from the superconducting state to the finite voltage state. This signal is used to trigger the fast voltmeter. Both voltage and current signal sequences are shown in the inset of Fig. 2.4.c. The switching current is then recorded by a computer interfaced to the multimeter via a General Purpose Interface Bus (GPIB). Such a procedure is repeated at least 10^4 times at each temperature (see Fig. 2.4.b), which allows us to compile a histogram of the switching currents (Fig. 2.4.c).

As shown in the next section, the flexibility of the measurement setup provides the possibility to investigate thermal and quantum properties of superconducting devices in wide range of parameters. Depending on the specific aim of each measurement, different instruments have been used and several Labview programs have been implemented. For istance, Stanford Research 530 Lock-In Amplifier has been used for magneto-resistance measurements on different oxide-based interfaces, while Keithley 2400 SourceMeter and LeCroy WaveRunner 6100A have been used for magnetic field pattern of Josephson systems. In both cases, Labview programs drive the measurements in remote control. All the instruments mentioned are decoupled form the laboratory electric lines using a transformer, to limit the external line disturbances influence on the measurement.

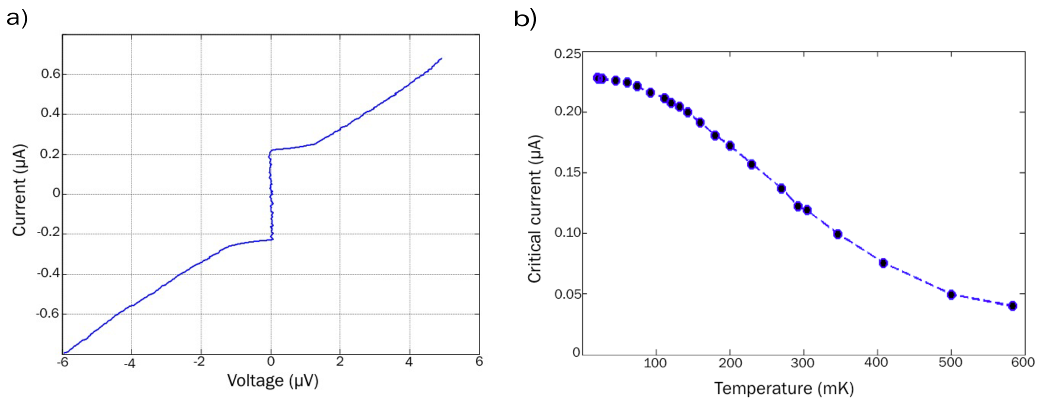

Figure 2.5: a) Current-voltage $I - V$ characteristic measured at 20mK on a dc SQUID, in which the junctions are composed by aluminium electrodes and by BiSe flakes as barrier respectively. b) Thermal behavior of the critical current of the dc SQUID. Black points refer to the measured I_c while the blue dashed line is a guide for the eye. Below 100mK the I_c(T) slope changes.

2.3 Functioning of the measurement setup

In the next chapters of this work, phase dynamics of underdamped and moderately damped JJs will be studied through measurements of SCD using the cryogenic and the electronic setup illustrated in sections 2.1 and 2.2 respectively. In this section, just to give an overview on the capabilities of the measurement setup for different types of experiments, measurements of the thermal and magnetic properties of novel oxide-based interfaces and of hybrid systems, such as junctions composed by superconductors and topological insulators as barriers, will be discussed.

Topological insulators constitute a topic of growing interest in the last few years, due to the uncommon features of their band structures[101, 102]. The linear energy spectrum corresponding to the edge states closely resembles the feature of a relativistic Dirac cone, thus providing a test branch material not only for fundamental physics experiment, but also for spintronic applications. In such systems, the presence of topologically protected bound states, known as Majorana bound state, is also envisaged[72]. As resulting from the collaboration between our group and the Quantum Device Group of the

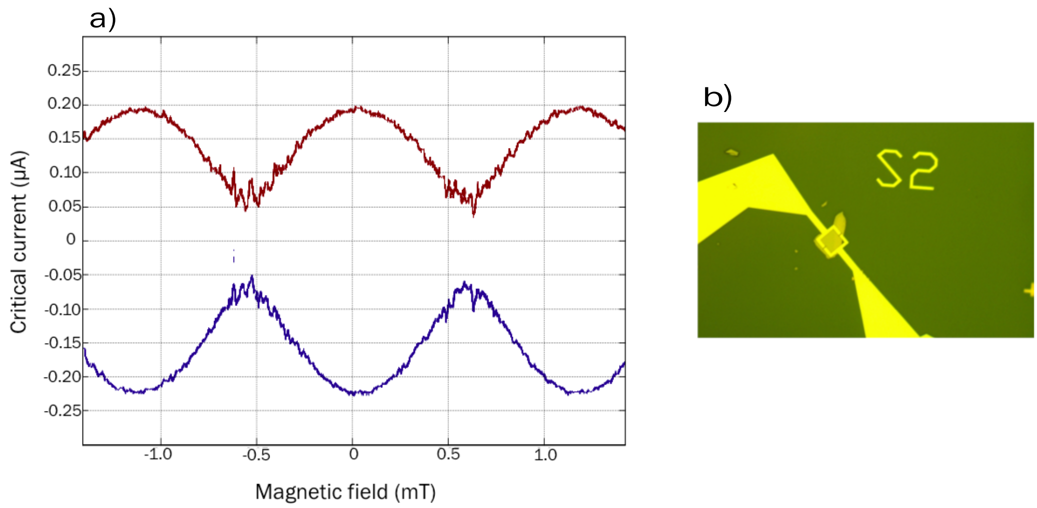

Figure 2.6: a) Magnetic field pattern of the positive (red curve) and negative (blue curve) I_c of the dc SQUID measured at 20mK. b) SEM image of the device.

Chalmers University of Technology leaded by Prof. Floriana Lombardi (Ph. D. thesis of Luca Galletti), junctions composed by topological insulators and superconductors (Al-BiSe-Al) have been realized with the goal to address proximity effect and phase sensitive measurements, both in single junctions and in dc SQUIDs, looking for unusual features.

A SEM image of one of the realized dc SQUIDS is shown in Fig. 2.6.b and the measurements reported in the following refer to such device. Fig. 2.5.a shows a current-voltage characteristic measured at 20mK: the high resolution of the measurement setup provides to measure systems with critical currents of about 100nA in the range of a few μV with high precision, as confirmed by the very low band noise on the voltage axis in the superconducting state (about 100nV). RSJ behavior has been measured in such devices, with a very small voltage step from the superconducting to the resistive state of about 1μV. The R_n is about 10Ω. In Fig. 2.5.b the temperature dependence of the I_c is shown: again the high resolution of the measurement setup allows to observe a change of the I_c(T) slope below 100mK. The good quality of the measurements is confirmed by the magnetic field pattern of the dc SQUID measured at 20mK. $I-V$ characteristics have been collected at different values of the magnetic field, in step of 15μT, and the I_c of each of these

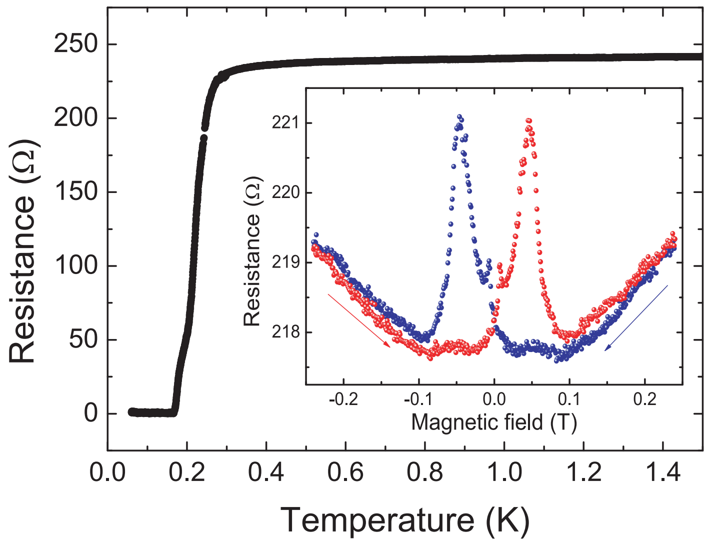

Figure 2.7: Thermal behavior of the sheet resistance of the oxide-based $LaGaO_3/SrTiO_3$ interface is shown. The superconducting critical temperature is about 170mK. In the inset, measurement of the resistance as function of the magnetic field up to ±240mT at 300mK is shown. Blue and red points refer to downward and upward sweep direction of the magnetic field respectively, as shown by the coloured arrows.

curves has been extrapolated using a Mathlab program. In Fig. 2.6.a the red curve represents the magnetic field behavior of the positive I_c while the blue curve refers to the magnetic field behavior of the negative I_c. In both cases, the experimental error on the determination of the I_c(H) is very low (about 1%). These measurements constitute an important step towards the comprehension of the proximity effect in hybrid systems.

Another topic of great interest in the last few years is the study of the transport properties of the two dimensional electron gas (2DEG) at the interface between the $LaAlO_3$ and $SrTiO_3$ wide bandgap insulators. The nature of the ground state of such 2DEG has been for years highly controversial[103], due to the contrasting reports of magnetism[104] and superconductivity[105]. More recently, several reports have accredited the idea of a phase-separated ground state, where superconductivity and magnetism can coexist[106, 107].

Again as resulting from the collaboration between our group and the

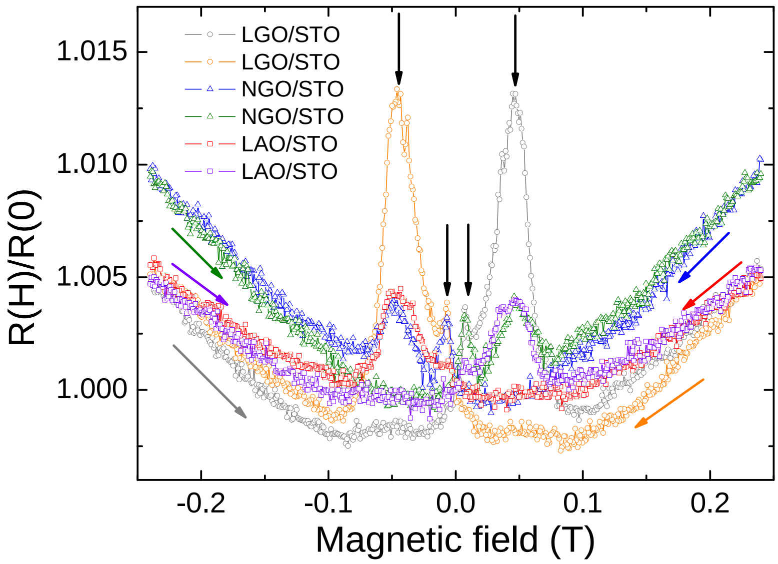

Figure 2.8: Magneto-resistance measurements performed at 300mK on different oxide-based polar-nonpolar interfaces. On the y-axis the resistance is normalized to the value in absence of magnetic field. Coloured arrows indicate the magnetic field sweep direction, while black arrows indicate the main magneto-resistance peaks at ±10mT and ±50mT, which occur with different relative magnitude for all the measured oxide-based interfaces.

M.O.D.A. group of the University Federico II of Naples, the low temperature magneto-transport properties of the polar-nonpolar $LaAlO_3/SrTiO_3$ interfaces have been compared with the properties of two novel oxide-based polar-nonpolar interfaces, such as $LaGaO_3/SrTiO_3$[108, 109] and $NdGaO_3/SrTiO_3$ recently developed in Naples. The results collected in the 20mK-1K range have confirmed the coexistence of superconductivity and magnetism both in $LaAlO_3/SrTiO_3$ and in the new interfaces.

In Fig. 2.7, the measurement of the resistance as function of the temperature for a 5x5mm^2 $LaGaO_3/SrTiO_3$ film is shown. The transition to the superconducting state occurs at 170mK, a value which is in good agreement with previously measured $LaAlO_3/SrTiO_3$ interfaces. In the inset, magneto-resistance measurement at 300mK of the same $LaGaO_3/SrTiO_3$ film is shown:

the magnetic field ranges from 240mT to -240mT (blue points) and viceversa (red points) in step of 1mT, the film is current biased with a sinusoidal waveform at low frequency ($\simeq$11Hz) and the lock-in amplifier has been used to measure the voltage. As shown also in Fig. 2.8, such magneto-resistance measurements display two main resistance peaks at $\pm$10 and $\pm$50mT when the direction of the magnetic field is reversed. In addition, such voltage peaks correspond to $\simeq$1% variation of the voltage measured in absence of magnetic field. The relative magnitude of the peaks is different for the different oxide-based polar-nonpolar interfaces, while the position of the peaks is the same. Again the capability to detect such features with high precision testifies the high quality of the measurement setup and provides the possibility to study the coexistence of superconductivity and magnetism is such systems. For both topics manuscripts are now in preparation.

Chapter 3

Measurements and data analysis

Progress in engineering new materials into junctions and in understanding and controlling the physics of interfaces may offer novel solutions for junctions of complementary functionalities and possibly of superior quality for specific properties, and therefore may lead in the long run to improve also specific qubit performances[16]. These junctions may fall in the moderately damped regime (MDR), which represents the technological result of the application of nanotechnology to conventional superconductors, and of the implementation of novel types of hybrid structures with unconventional barriers composed by grain boundaries[24], graphene sheets[28], topological insulators flakes and so on.

In this chapter, phase dynamics of moderately damped JJs will be discussed through measurements of SCDs to study both thermal activation (TA) and MQT. In the first section, measurements on a conventional underdamped JJ will be shown as a reference for the study of MQT and dissipation. In the second and in the third sections the MDR will be addressed through measurements on LTS low-J_c JJs, and the damping level will be studied through numerical methods. Phase dynamics of YBCO JJs will be discussed for different GB configurations and the experimental results will be studied by using the tools developed for conventional JJs. The experimental results and the numerical outcomes allow us to reconstruct a phase diagram condensing the various activation regimes[35, 56]. Such a phase diagram is valid in a large range of dissipation conditions and constitutes a functional guide to classify the switching behavior of a JJ, clearly defining the fundamental junction parameters and energies in the MDR[110, 111]. It is therefore a reference for phase dynamics of novel types of junctions and systems for which the nature of the current induced transition from the superconducting to the normal state has not been completely clarified.

3.1 Phase dynamics of underdamped Josephson junctions

As a reference for the study of the MDR, a conventional Nb/AlOx/Nb JJ has been measured. In Fig. 3.1.a the $I-V$ characteristic measured at the base temperature of T=20mK is shown. While the critical current $I_c \simeq 18\mu$A and $R_n \simeq 130\Omega$, the switching voltage V$_{sw}$, at which the junction switches from the superconducting to the normal state, is about 3mV. The dimensions of the counter and base electrodes are 3x2.5μm^2. Taking into account a specific capacitance of 40fF/μm^2 typical for Nb tunnel junctions[34], we reliably estimate a junction capacitance of 0.3pF. Assuming that the dissipative element R associated to the junction is completely determined by the circuitry connected to the junction[14] ($R \approx 100\Omega$), we obtain a quality factor of about 15 and the junction falls in the underdamped regime. In Fig. 3.1.b measurements of SCDs at temperatures ranging from the base temperature up to 2.5K are shown. The experimental tecnique has been explained in chapter 2. In this case the current ramp rate is dI/dt =30mA/s. To avoid heating effects[14], the ramp has been setted in order to reduce the time the junction spends in the resistive state and a dwell time for $I=0$ has been programmed in order to increase the time the junction spends in the superconducting state (see inset of Fig. 2.4.c).

For each temperature the first and second moment of the switching histograms have been calculated and the temperature dependence is shown in Fig. 3.2. The first moment is the mean switching current I_{mean} and the second central moment is the standard deviation σ, which is proportional to the width of the switching distribution. At temperatures higher than 200mK

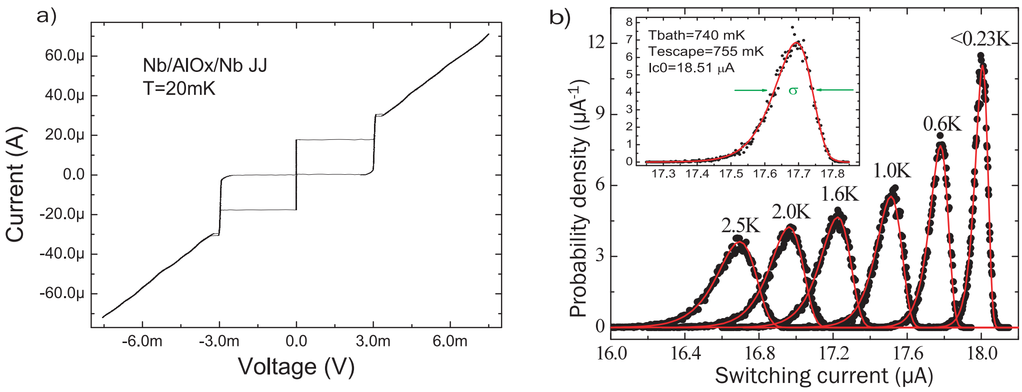

Figure 3.1: a) $I-V$ characteristic of a Nb/AlOx/Nb JJ measured at 20mK. b) Measurements of SCDs (black points) along with the theoretical fits (red lines), according to thermal and quantum escape rates (Eqns. 1.5 and 1.6), from the base temperature up to 2.5K. Below 230mK the histograms overlap and only one distribution has been shown. In the inset, the fit of the SCD measured at 0.74K is shown, along with the values of the fitting parameters T_{escape} and I_{c0}.

we observe a broadening of the switching distributions, which indicates that the junction is in the TA regime. As a matter of fact when T increases the thermal fluctuations increase and the width of the switching distributions increases as well. In this regime σ increases as $T^{2/3}$ (the black dashed line in Fig. 3.2.a), as expected from the thermal escape rate Γ_T (Eqn. 1.5). Such a thermal dependence derives from the cubic approximation of the height of the potential barrier of the washboard potential[14]: $\Delta U \propto E_J\,(1 - I/I_{c0})^{3/2}$. Below 200mK σ saturates (black line in Fig. 3.2.a), indicating the transition to the MQT regime with a crossover temperature of about 230mK. In this regime the histograms overlap. The estimate of T_{cross} is in good agreement with the junction parameters (see Eqn. 1.8). We have analyzed these data through fits of the probability density of switching. The fitting parameters are T_{escape}, which is related to the width of the distribution, and I_{c0}, which is the critical current in absence of thermal fluctuations and is related to the position of the maximum of the distribution. In the TA regime, the discrepancy between T_{escape} and the bath temperature indicates possible noise and heating effects which could affect the measurements. In the inset of

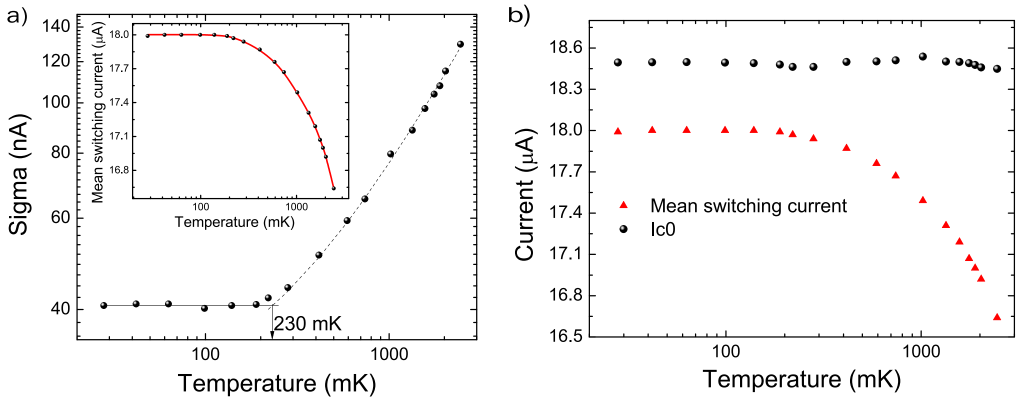

Figure 3.2: a) Thermal behavior of σ: above 230mK the junction is in the TA regime and σ increases with temperature as $T^{2/3}$ (black dashed line), while below 230mK σ saturates indicating the transition to the MQT regime. The black line indicates also the mean value of σ in the quantum regime. In the inset, thermal behavior of I_{mean} (black points) is shown compared to the expectations based on TA and MQT escape rates (red line). The agreement is excellent. b) Thermal dependence of the fitted values of I_{c0} compared to I_{mean}. In the quantum regime the ratio between I_{mean} and I_{c0} is about 97%.

Fig. 3.1.b an example of a fit of a switching distribution is shown along with the values of the fitting parameters. The low discrepancy between the bath temperature and T_{escape} confirms the good functioning of the experimental set-up and of the measurements. Finally, in Fig. 3.2.b the temperature dependence of I_{mean} is compared with I_{c0} as estimated from the SCD fits. I_{mean} is constant in the MQT regime, and decreases by increasing the temperature above T=200mK, consistently with what expected from TA regime (see also the inset of Fig. 3.2.a), while I_{c0} is almost constant in the whole temperature range[112]. By collecting the I_{c0} values of all fits, the estimate of I_{c0} is given by the mean value of such an ensemble and the uncertainity is given by the standard deviation of the mean of the same ensemble ($I_{c0} = 18.50 \pm 0.03 \mu A$). The thermal dependences of the SCDs, I_{mean}, σ, I_{c0} illustrated in this section are typical of the underdamped dynamics. In the next sections of this chapter important deviations will be shown as the MDR will be approached.

3.2 Macroscopic quantum tunneling in moderately damped NbN Josephson junctions

In this section and in the next two sections, the phase dynamics of moderately damped NbN JJs will be studied, both in the thermal and in the quantum regime. NbN is a material of great interest for sensor applications[113, 114] since it guarantees fast non equilibrium electron-phonon relaxation times τ, higher gap values and tends to form smaller amount of native surface oxide compared with traditional junction technologies based on Nb, Al and Pb[115]. Short τ are in principle favorable for multi-photon phenomena in Josephson tunneling, allowing to extend studies on few photon processes[25, 116, 117] to dynamics involving several photons and effects of non-equilibrium[118]. Low J_c NbN devices may contribute to set a more comprehensive NbN platform, and constitute a nontrivial extension of the more established high J_c NbN junctions, usually designed for superconducting digital circuits[119, 120].

The JJs reported in this section consist of a NbN/MgO/NbN trilayer epitaxially grown on a single-crystal MgO substrate[121]. A schematic drawing of the junction is reported in Fig. 3.3.a. Epitaxial MgO is traditionally a high quality tunnel barrier[122] whose complete impact on superconducting electronics is still under investigation and depends on the interface with the superconducting layers, on its epitaxial quality and possibly on its size. The NbN base and counter electrode are both 200nm thick and were deposited using DC magnetron sputtering with a Nb target in a mixture of 5 parts argon and 1 part nitrogen gases. The MgO tunnel barrier is about 1.0nm thick and was deposited by RF sputtering. A more detailed description of the fabrication process can be found in Ref. [121].

The realized junctions have been tested through preliminary measurements of the $I-V$ characteristics (see Fig. 3.3.b). We have measured circular junctions of various diameters ranging from 2 to $10\mu m$ and consistently found a very low J_c of about $3A/cm^2$, which is the lowest value ever reported for NbN based junctions[123]. For circular junctions with a diameter of 10μm, I_c is about 2μA and the junction falls under the criteria of the MDR, as demonstrated in the next section. Large values of the switching voltage (V$_{sw}$=5.7mV) and of the I_cR_n product of about 5mV have been

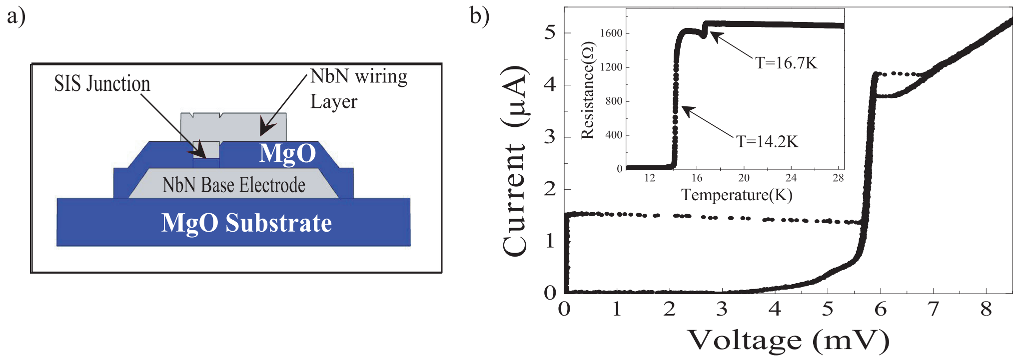

Figure 3.3: a) Cross section of the NbN/MgO/NbN tunnel junction. b) $I-V$ characteristic of a 10μm diameter JJ measured at 300 mK. The inset shows the measurement of the resistance as a function of the temperature of the device.

measured along with a small subgap leakage voltage (V_m=23.5mV measured at 3mV)[124]. From the magnetic field dependence of the critical current we have estimated the London penetration depth at 300mK to be about λ_L =190nm, which is in good agreement with previously measured values for epitaxially grown NbN[125]. Therefore for a barrier of thickness t=1nm the Josephson penetration depth turns out to be[3] λ_J=$(\hbar c^2/8\pi e J_c d)^{1/2}$=150$\mu$m, where $d = 2\lambda_L + t$. This nominally guarantees more uniform currents than in devices of comparable sizes but larger J_c.

In figure 3.4 measurements of SCD (black points) are shown at different temperatures ranging from the base temperature up to 1.56K, along with the theoretical fits of the probability density (red lines). From these fits we have obtained $I_{c0} = 1.91 \pm 0.03\mu A$ using the methods explained in section 3.1, while the value of the damping, $Q = 2.7 \pm 0.1$, is deduced from the PD regime as discussed in the next section.

In fig. 3.4.b the thermal dependence of σ is shown. Above 90mK the data agree with predictions for TA, while the saturation of σ at T< 90mK indicates that the escape is dominated by quantum tunneling and constitutes the first reported data of MQT in NbN/MgO/NbN JJs[123]. An estimate of the capacitance C=0.3pF, of the plasma frequency ω_{p0} $\simeq$22GHz and of the resistance R=65Ω can be obtained on the basis of T_{cross}, Q and I_{c0}. The value of the capacitance can in principle be calculated also from the posi-

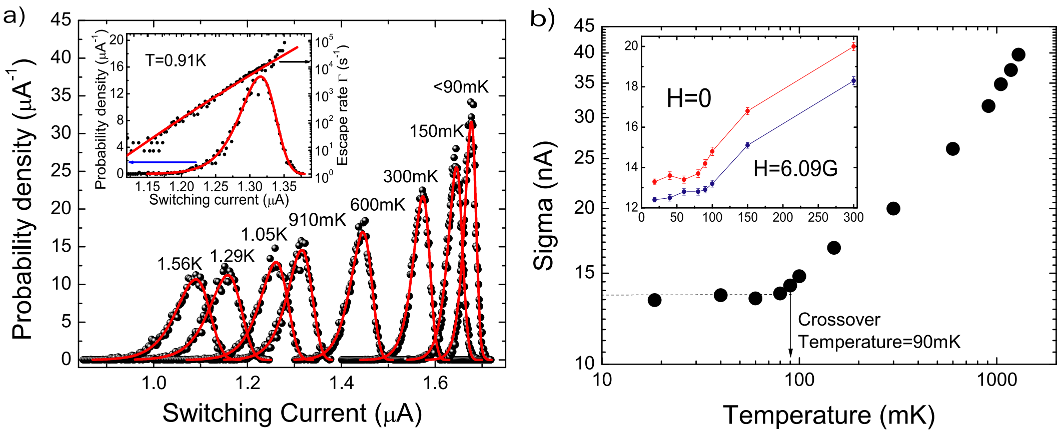

Figure 3.4: a) SCDs at H=0 for different bath temperatures. The symbols represent data and the red lines are the fitting curves. The inset shows the quality of the fit at T=0.91K, along with the data converted into escape rates. b) Temperature dependence of the standard deviation σ of the switching distributions at zero magnetic field; the error bars are within the width of the data point. The black arrow indicates the quantum crossover temperature T_{cross} while the black dashed line indicates the saturation of σ below 90mK. The inset shows σ vs temperature below 300mK for two values of magnetic field. The magnetic field induces smaller values of σ and a reduction of T_{cross} with respect to the case H=0.

tion in voltage of the Fiske steps, but in this case the amplitude of such steps is vanishingly small[3]. This is partly due to the fact that the Fiske resonance amplitude depends on[126] $J_c * (r/\lambda_J)^2$, where r is the junction radius. Therefore, the Fiske step fades out because of the low values of J_c found in our junctions and because $r << \lambda_J$. We have also measured the temperature dependence of σ for a reduced critical current by applying an external magnetic field (see inset of Fig. 3.4.b). Such temperature dependence is a neat confirmation of MQT[14, 123]: H induces both smaller values of σ and a decrease of the plasma frquency ω_p and therefore of the crossover temperature T_{cross} consistently with MQT expectations[3, 14].

The possibility to achieve very low J_c in moderately damped NbN junctions, combined with their short electron relaxation time τ <10ps[127], paves the way to novel experiments aimed to observe extreme multi-photon tunneling quantum effects. As a matter of fact, the intrinsic properties of low

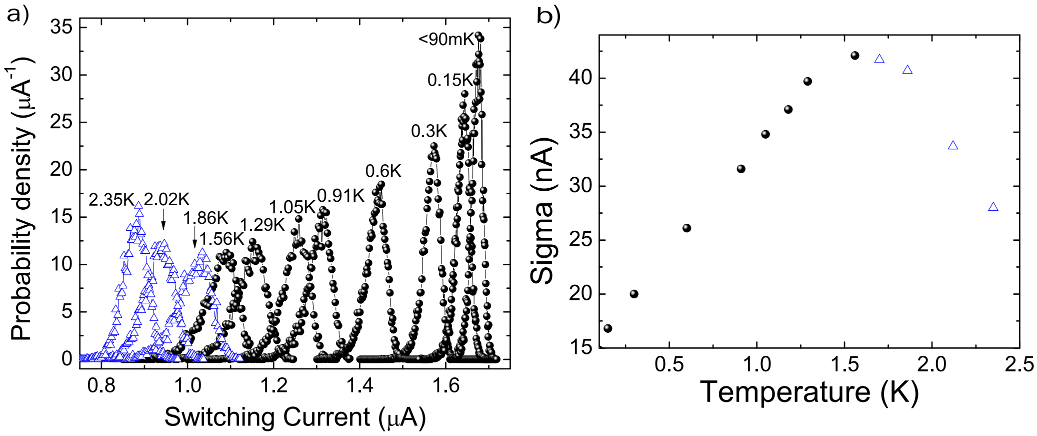

Figure 3.5: a) SCDs collected at different temperatures ranging from the base temperature up to 2.35K in absence of magnetic field. b)Thermal behavior of σ of the SCDs shown in a). Black points refer to switching histograms in the TA regime while blue open triangles refer to histograms in the PD regime. In both cases the lines are a guide for the eye.

J_c NbN junctions with $I_{c0} < 1\mu$A meet the condition $\tau < \hbar/E_J = 2e/I_{c0}$ for measurements of multi-photon effects in the presence of a non-stationary signal, and guarantee quite accessible working regimes to observe Euclidean resonance (ER)[118]. According to numerical simulations presented by Ivlev et al.[118] for ER proposals, the moderately damped junction would require amplitudes ($\tilde{I}$) and frequencies (Ω_p) of the non stationary component of the bias current lower than 0.2μA and larger than 20GHz respectively and therefore experimentally feasible. In the following we are mostly interested in NbN JJs as a reliable tunable system, where to test concepts and algorithms to explain PD and to evaluate the dissipation in this still unexplored regime.

3.3 Diffusive dynamics in moderately damped NbN Josephson junctions

In this section we focus on the thermal regime of the same NbN/MgO/NbN junction discussed in the previous section. In Fig. 3.5.a we report the SCD curves collected over a wide range of temperatures in absence of an externally

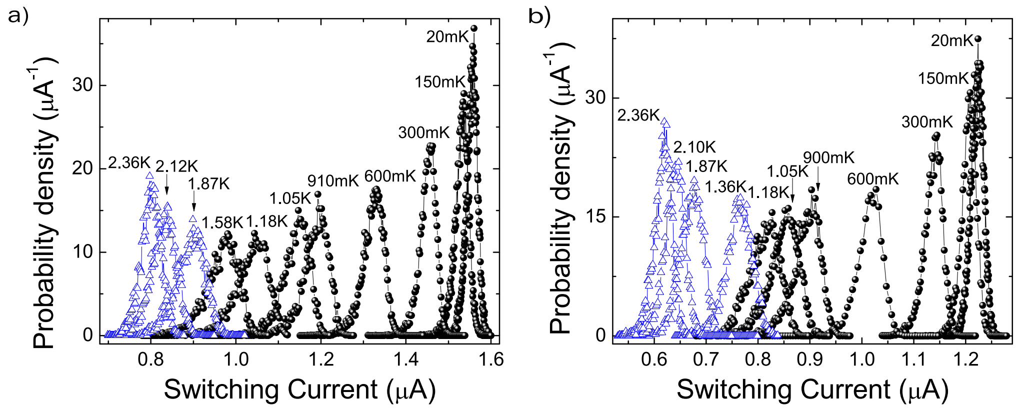

Figure 3.6: SCDs measured at different temperatures for H=3.045G (a) and for H=6.09G (b). In both cases, black points relate to histograms in the TA regime while blue open triangles refer to distributions in the PD regime.

applied magnetic field. Distinctive fingerprints of PD (see section 1.2), due to multiple hopping and retrapping of the phase particle in the washboard potential, can be found in the temperature dependence of σ of the SCD curves, which is shown in Fig. 3.5.b. The most striking effect observable is the appearance of an anticorrelation between the temperature and the width of the switching distributions[34, 35, 36]. Below 1.6K the histograms broaden increasing the temperature and σ follow the expected $T^{2/3}$ dependence (black points in Fig. 3.5.a and Fig. 3.5.b), while above the transition temperature T^{*}=1.6K the histograms shrink with a consequent increase of their amplitude and the temperature derivative of σ(T) becomes negative[47] (blue open triangles in Fig. 3.5.a and Fig. 3.5.b). SCDs have been measured also in presence of an external magnetic field. Such measurements are reported in Fig. 3.6.a for H=3.045G and in Fig. 3.6.b for H=6.09G respectively. As dicussed in the previous section, the magnetic field induces a reduction of I_c, thus providing an additional knob to tune the phase dynamics. As it can be seen in Fig. 3.7, the reduction of the Josephson energy causes the reduction of the transition temperature T* when the magnetic field is increased[47].

We compare our results with the model of Fenton and Warburton[50] which condenses ideas on PD of the last 20 years, offering a reliable methodology to evaluate the dissipation level in the MDR, in analogy with what well established for underdamped junctions[14]. According to Ref. [50], the anomalous thermal behaviour of σ can be explained if the competition between thermal escape and multiple retrapping processes is taken into account. The retrapping rate Γ_R strongly depends on the quality factor of the junction (see Eqn. 1.10), therefore the study of the PD regime provides a powerful tool to estimate the dissipation level in the junction. The phase difference $\varphi(t)$ is the solution of the following Langevin differential equation (see also Eqn. 1.4):

$$\varphi_{tt} + \varphi_t/Q + i + i_N = 0 \tag{3.1}$$

Times t are normalized to $1/\omega_p$, the subscript t indicates the derivative with respect to time, i is the bias current normalized to the critical current I_{c0} and i_N is a Gaussian correlated thermal noise current, i.e.:

$$\langle i_N(t), i_N(t') \rangle = \sqrt{2\pi k_B T / Q I_{c0} \Phi_0}\, \delta(t - t'). \tag{3.2}$$

Frequency dependent damping[31] (see section 1.2) assumes that phase dynamics is affected by two quality factors, the high frequency quality factor $Q_1 = Q(\omega_p)$ and the low frequency quality factor $Q_0 = Q(\omega \simeq 0)$. Therefore, Q_1 is related to the phase dynamics occurring at time compared to the inverse of the plasma frequency, while Q_0 is related to the phase dynamics in the steady state. Since the switching processes occur at frequencies of the order of the plasma frequency, it should be possible to fit the switching histograms by using a single quality factor $Q = Q_1$ in Eqn. 3.1, and Q_0 should play a minor role since the steady motion is not involved in the switching processes.

Stochastic dynamics is simulated by integrating the Langevin Eqn. 3.1 by a Bulirsh-Stoer integrator using as noise generator the cernlib routine RANLUX[77]. The multiplicity of switching modes between the running and the trapped states raises a problem of how to define an escape event. In our simulations the condition to define the switch is $v(i,t) > v(i,0)/2$, where v represents the average velocity of the phase particle in the washboard potential. In other words, the particle spends in the running state more than 50% of the observation time. Typical runs for simulations of Eqn. 3.1 will last from $4 \cdot 10^6$ to $6 \cdot 10^6$ normalized time units, that is, $6 \cdot 10^5$ to $9 \cdot 10^5$ plasma periods[47]. Observation time for each point generated in the $I - V$ characteristics is $2 \cdot 10^4$ time units, which is a long enough time to ensure that the average time spent in running/zero voltage state does not vary as a

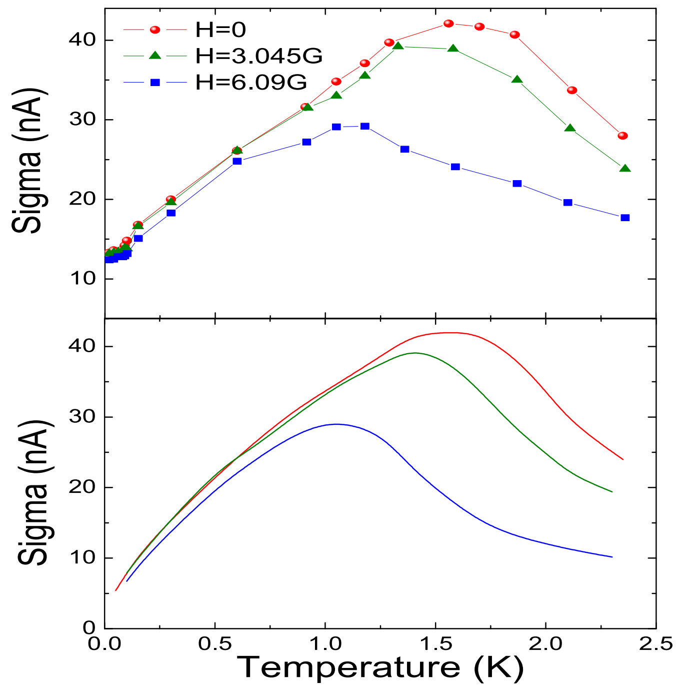

Figure 3.7: Upper frame: temperature dependence of the standard deviation σ of the switching distributions for H=0G (circles), H=3.045G (triangles), and H=6.09G (squares). Bottom frame: Monte Carlo simulations of the data. Data and numerical simulations are in good agreement in the whole temperature range and for all magnetic fields.

function of the observation time[31]. To obtain the SCD we have simulated a number of escape events between 3000 and 5000, which is similar to the number of counts experimentally measured. Simulated curves of σ vs T are plotted in the lower frame of Fig. 3.7 for the same values of the magnetic field used in the experiment[47]. The critical current I_{c0} has been fitted at low temperatures in the TA and in the MQT regime (see section 3.2), while the quality factor is the fitting parameter. Good agreement between data and numerical simulations has been obtained with $Q = 2.7 \pm 0.1$.

In Fig. 3.8.a the mean switching current I_{mean} (data points) is plotted along with the expected values (solid lines) without taking into account retrapping effects. Due to the onset of retrapping events, it is necessary to provide a larger tilt to the energy potential to allow the system to switch to the running state. Discrepancies at higher T demonstrate that the ex-

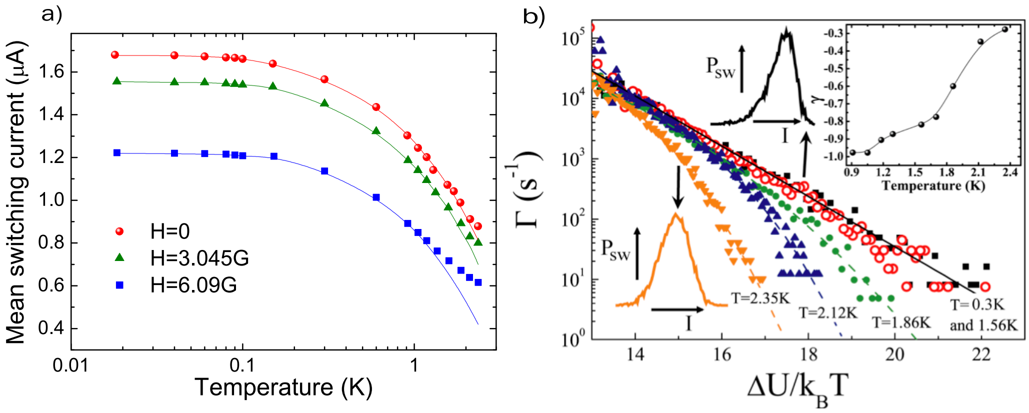

Figure 3.8: a) Temperature dependence of the mean switching current of the SCDs for H=0 (circles), H=3.045G (triangles), and H=6.09G (squares). The solid lines are the calculated values of I_{mean} considering MQT and TA and no retrapping. b) Escape rates (symbols) as a function of the ratio between the barrier height and the thermal energy at zero magnetic field for temperatures near T^*. Below T^* the fit has been calculated using thermal escape rate (solid line), while above T^* numerical simulations (dashed lines) of the phase dynamics have been performed. The inset shows the experimental value of the skewness γ of the switching distributions as function of the temperature.

perimental values of I_{mean} above T^* are greater than the predicted values, which only consider the effects of TA. Due to the dependence of T^* with the external magnetic field, as shown in Fig. 3.7, from the data taken in presence of a 6.09G static magnetic field, the onset of retrapping clearly occurs at a lower temperature.

Phase diffusion also appears in the escape rates Γ shown in Fig. 3.8.b as a function of the ratio between the barrier height ΔU and the thermal energy. The escape rates are calculated from the switching distributions using Eq. 1.9. In the TA regime the distributions are asymmetric and skewed to the left, and Γ values all fall onto the same line, as it is the case for the reported data from T=0.3K to 1.56K. Retrapping processes cause a progressive symmetrization of the switching distribution, as it can be seen in Fig. 3.5.a, Fig. 3.6.a and Fig. 3.6.b, and a bending in the Γ vs $\Delta U/k_BT$ curves, as shown in Fig. 3.8.b. We use the same procedure previously described to evaluate the simulated escape rates as function of the ratio $\Delta U/k_B$T. Numerical data

Table 3.1: Comparison of device parameters.

Device Structure	I_{c0} (μA)	$Q(I=0)$	R (Ω)	C (fF)	ΔU/k$_B T^*$
NbN/MgO/NbN JJ[47]	1.91	2.7	65	300	17
Al/AlOx/Al dc SQUID[35]	0.2	3.9	500	100	14
Al/AlOx/Al JJ[35]	0.63	3.6	230	130	18
Nb/AlOx/Nb dc SQUID[34]	4.25	2.4	70	90	15
Nb/AlOx/Nb dc SQUID[34]	2.9	3.3	70	260	17
Bi-2212 Intrinsic JJ[46] [1]	1.26	2.2	62	330	14
Nb/AlOx/Nb JJ[48]	0.122	4.8	1800	20	NA
Nb/AlOx/Nb JJ [48]	0.48	3.3	315	77	12
S-2DEG-S[36]	2.5	1.1	36	110	24

[1] In this work the authors have estimated the fit parameters to be temperature dependent. Here we report the values at the lowest experimental temperature T=1.5K.

have been obtained by a polynomial fit of numerical escape rates in order to compare it with experiments. The same value of the Q factor is obtained by fitting the curves, shown in dashed lines in Fig. 3.8.b[47]. The symmetrization of the switching distribution due to the interplay between escape and retrapping events can be clearly observed by plotting the skewness of the distributions γ as a function of the temperature. γ is the ratio m_3/σ^3 where m_3 is the third central moment of the distribution. For the lowest temperatures we obtain $\gamma = -1$, which is consistent with the case of switching current distributions in the quantum or thermal regime. As the temperature increases the distributions become more and more symmetric as γ tends to zero. It should be noted that for these data the temperature T^* at which the derivative of $\sigma(T)$ changes sign is equal to 1.6K and that the skewness starts increasing already at about 1.2K, which is a clear indication that the onset of retrapping phenomena occurs well below T^*[50].

A non exhaustive list of Josephson devices that have displayed a similar PD behavior is reported in Table 3.1 along with most of the relevant device parameters. The papers on which Table 3.1 is based report on similar experimental results but their interpretation differs in a few assumptions, as properly pointed by Fenton and Warburton[50]. For instance Kivioja et al.[35] interpreted their results within the semiclassical model of Larkin and Ovchinnikov[128]. Since in dc SQUIDS there are few energy levels and the hypothesis of continuous energy spectrum is not valid, they used a model which takes account both PD and level quantization. On the other hand this model, which assumes separated levels in the metastable well, is not properly valid for a single JJ since the number of energy levels is large and the separation is smaller than their width. Männik et al.[34] and Bae et al.[46] calculated the retrapping probability through Monte Carlo simulations. The authors expressed the net escape rate as a sum of probabilities of multiple escape-retrapping events based on thermal escape rate and retrapping probability. The probability of retrapping is considered as a time-independent quantity which is in contrast with the work of Ben-Jacob et al.[45], in which retrapping is modeled by a rate and therefore by a probability increasing proportionally to the time spent in the running state. The very good fitting of experimental curves obtained in this work using the approach of Ref. [50] confirms the occurrence of a multiple-retrapping regime with a large number of escapes of duration of Γ_R^{-1} and in particular it confirms that the time dependence of the retrapping probability cannot be ignored. If the fast scattering time plays a role in diffusive process is a topic of further investigations. As it can be seen from Table 3.1, all the junctions exhibiting PD over a large range of materials and geometry have low critical current ($I_c \simeq 1\mu$A), 1<Q<5 and $12 < \Delta\mathrm{U}/\mathrm{k}_B T^* < 24$, which are therefore the relevant parameters signaling the insurgence of multiple escape and retrapping in the washboard potential.

3.4 Ramp rate dependence of the transition temperature from thermal activation to phase diffusion regime

The JJs discussed in this section consist of epitaxially grown NbN/AlN/NbN trilayers. The impact of such high quality junctions on superconducting quantum computing is still under investigation. In the last years, great at-

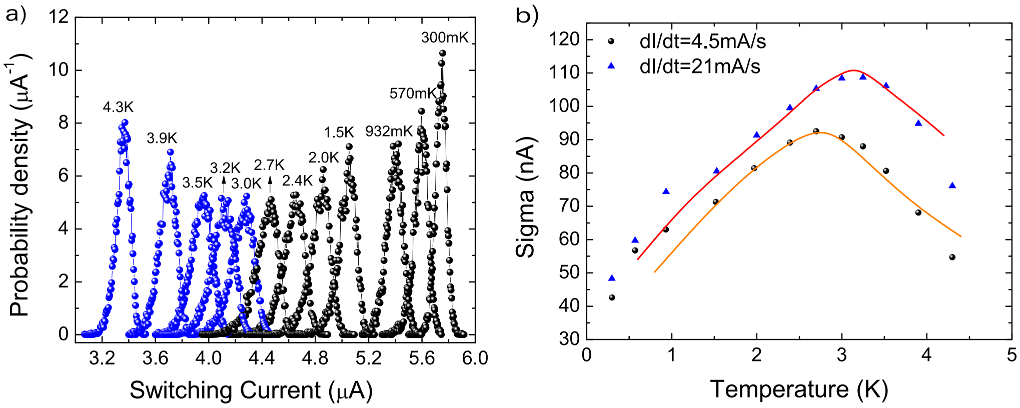

Figure 3.9: a) SCDs measured at different temperatures on a moderately damped NbN/AlN/NbN JJ with ramp rate dI/dt=4.5mA/s. Black points refer to histograms in the TA regime while blue open triangles refer to distributions in the PD regime. b) Temperature dependence of σ for two sets of bias ramp rate: black circles refer to dI/dt=4.5mA/s while blue triangles refer to dI/dt=21mA/s. The solid lines are numerical simulations of the data.

tention has been devoted to realize Josephson qubits based on advanced materials since the superconductor's native oxides and the interface between superconductor and its substrate have been suspected as regions with high density of unpaired surface spins (magnetic two level states TLS). This would lead to the low frequency flux noise, an additional source of dephasing both for Josephson flux and phase qubits[129]. The epitaxial growth of NbN film could suppress the amount of the surface defects and oxides. In addition, the realization of a qubit with NbN/AlN/NbN JJs showed a surprisingly long coherence time[129].

In order to study the phase dynamics of such structures, we have realized circular JJs with J_c=10A/cm^2 and with diameters ranging from 4μm to 20μm. This work has been performed in collaboration with CNR-ICIB Institute of Pozzuoli, in Naples. In this section we present the results for a circular junction with a diameter of 4μm and a critical current of $I_c \simeq$ 6μA, which again falls in the MDR as demonstrated below. In the previous section we have studied the role played by the magnetic field in tuning the phase dynamics in the thermal regime. Here we cover another important aspect related to the behavior of the damping factor Q and of the transition temperature T^* as a function of the bias ramp rate.

In Fig. 3.9.a switching histograms collected in a wide range of temperature ranging from 0.3K up to 4.3K are shown. In this case the transition temperature T^* from the TA to the PD regime is T^*=2.7K and the bias ramp rate is dI/dt=4.5mA/s (as a term of comparison, the ramp rate used for the measurements on NbN/MgO/NbN JJs is dI/dt=0.15mA/s). In Fig. 3.9.b the thermal dependence of σ for two different sets of measurements which refer to different bias ramp rate is shown. Black points refer to dI/dt=4.5mA/s while blue triangles refer to dI/dt=21mA/s. In both cases there is a transition from TA to PD regime, but the transition temperature T^* changes from 2.7K at dI/dt=4.5mA/s to 3.2K at dI/dt=21mA/s. Monte Carlo simulations of the data have been performed, in the same way explained in the previous section. As shown by the solid lines in Fig. 3.9.b, good agreement between data and simulations is achieved with the same fitting parameters, in particular with the same Q=1.85±0.05. Only the ramp rate is changed between the two sets of simulations. Such effect is again in strong agreement with the model of Fenton and Warburton[50] and provides a method to change T^* without affecting the fundamental parameters of the JJ.

3.5 Phase dynamics of YBCO grain boundary Josephson junctions

In the second part of this chapter, phase dynamics of biepitaxial YBCO JJs will be addressed. As discussed in section 1.4, recent experiments demonstrate that, despite the presence of low-energy quasi-particles, macroscopic quantum phenomena can be observed also in HTS JJs[24, 25, 26]. These investigations revealed coherence beyond expectations and paved the way to a more systematic and reliable study of phase dynamics in HTS devices, which has been elusive for a long time. Phase dynamics of HTS JJs is indeed particularly rich, thanks to the new flavors brought in by HTS unconventional superconductivity[6, 23, 57] (see section 1.3). Some effects generally observed in HTS junctions, as for example the values of the I_cR_n parameters on average one order of magnitude lower than the expected value of 2Δ,

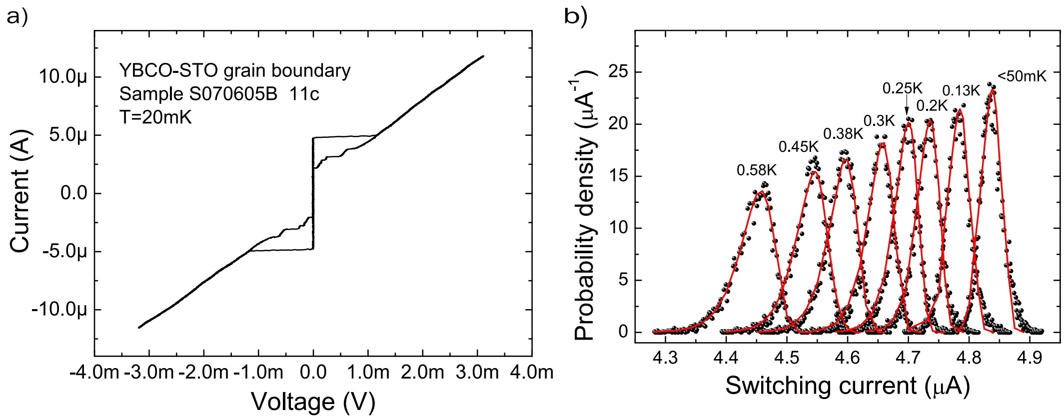

Figure 3.10: a) $I-V$ characteristic of YBCO GB STO-based 11c junction measured at 20mK. b) SCDs measured in the temperature range from 20mK up to 580mK. Black points are data while red lines are fits according to TA and MQT (for T<50mK) escape rates.

may signify the relevance of other energy scales in these devices[23, 51]. One possibility is the Thouless energy associated to single nanoscale channels in a filamentary approach to transport across the GB[130].

In this section phase dynamics of STO-based biepitaxial JJs will be discussed, while in the next section experimental results on samples realized on LSAT substrates will be illustrated. STO is the most commonly used substrate for the realization of YBCO films and devices thanks to the good reticular matching with YBCO, chemical compatibility and structural stability. On the other hand, it has high values of the dielectric constant, which also increases when lowering temperature up to values in the range of 10^4[131]. Therefore, the large stray capacitance of this substrate could introduce a capacitive element in parallel to the junction, making the final circuit structure more complicated[25, 77, 132]. LSAT was developed a few years ago with the aim of combining the low dielectric constant and the low loss tangent of $LaAlO_3$ (LAO) with the structural stability of STO[133]. In addition, LSAT has lattice parameter smaller than STO, allowing a decrease of the mismatch with the YBCO film orientations used in the off-axis biepitaxial structure. All these properties make LSAT an excellent candidate for the realization of high quality HTS biepitaxial junctions. The capability to engineer junctions on different substrates offers the opportunity to disentangle the role of the

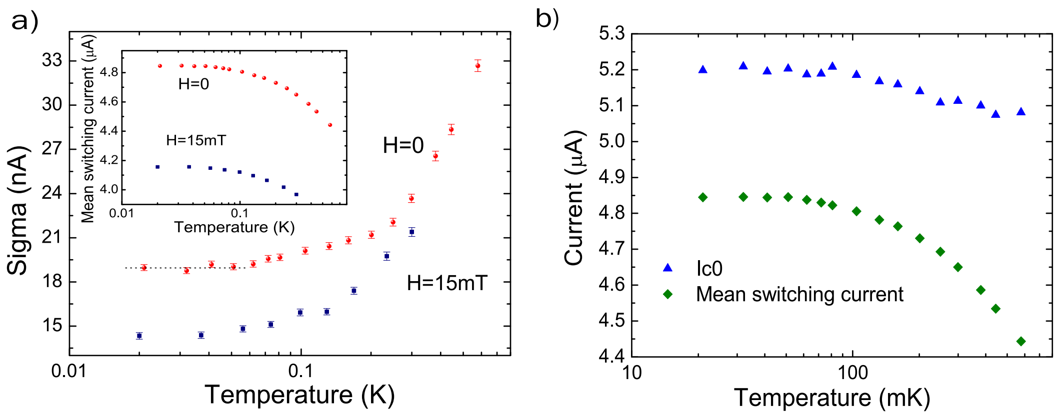

Figure 3.11: a) Thermal dependence of σ of junction 11c at H=0 (red points) and H=15mT (blue squares). The dashed black line indicates the saturation of σ below 50mK and the transition to the MQT regime. At H=15mT we observe smaller values of σ. In the inset the thermal dependence of the mean switching current is shown for the same values of the magnetic field. b) A comparison between the fitted values of I_{c0} and the experimental I_{mean} is shown. I_{mean} is constant in the MQT regime below 50mK, while it decreases above 50mK. I_{c0} is almost constant below 100mK. Above 100mK a decreasing trend is observed.

shell circuit in the phase dynamics and thus a tuning of the capacitive effects in HTS GB biepitaxial JJs[55, 111].

In Fig. 3.10.a the $I-V$ characteristic measured on STO-based GB junction 11c at the base temperature is shown. The critical current $I_c \simeq 5\mu$A, $R_n \simeq 250\Omega$ and the switching voltage V_{sw} is about 1mV. For this sample, as well as for the junctions reported in this and in the next section, $I_c R_n \simeq V_{sw}$ thus confirming the existence of an energy scale one order of magnitude lower than the YBCO gap[134]. In addition, such junctions are characterized by an amplitude of hysteresis ranging from 25% up to 70%. For junctions 11c and 12b (see Fig. 3.12), the thicknees of the YBCO film is about 250nm while the width of the junctions are 0.8μm and 1.5μm respectively.

In Fig. 3.10.b measurements of SCD on junction 11c at temperatures ranging from 20mK up to 580mK are shown; in this case the current ramp rate is dI/dt =0.15mA/s. Temperature dependence of σ and I_{mean} is shown in Fig. 3.11. At temperature higher than 50mK the broadening of the

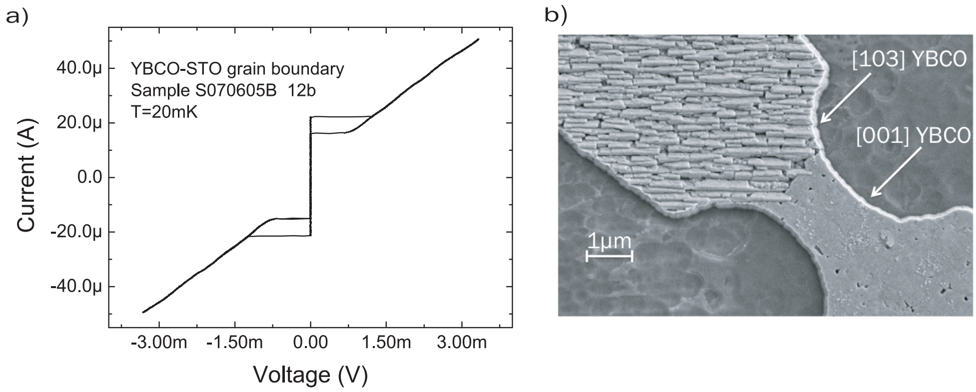

Figure 3.12: a) $I - V$ characteristic of YBCO GB STO-based 12b junction measured at 20mK. b) SEM image of the junction.

switching distributions is observed, which indicates that the junction is in the TA regime. Below 50mK σ saturates (black dashed line in Fig. 3.11.a), indicating the transition to the MQT regime. In the same figure, data are also reported for a reduced critical current by applying an external magnetic field. Smaller values of σ are observed and the crossover temperature T_{cross} is reduced. We have analyzed these data through fits of the probability density of switching, in the same way as described in section 3.1. I_{c0} has been determined from the fits at very low temperature ($I_{c0} = 5.20 \pm 0.04\mu$A) and the quality factor Q=1.40±0.05 has been estimated from the phase diagram for moderately damped junctions reported in Fig. 3.18.b (see next section). The capacitance C=1pF and the resistance R=11Ω have been determined on the basis of T_{cross}, I_{c0} and Q, in analogy to what described in sections 3.2 and 3.3. The resulting specific capacitance is $5{\cdot}10^{-4}$F/cm^2, in good agreement with STO-based GB biepitaxial JJs reported in previous works[23, 24, 134].

In Fig. 3.11.b the temperature dependence of I_{mean} is shown and compared to the I_{c0} value estimated from the SCD fits. I_{mean} is constant in the MQT regime, while at higher temperatures (T>50mK) it begins to decrease (see also the inset of Fig. 3.11.a). I_{c0} is almost constant below 100mK, a decreasing trend is observed at T>100mK which is in contrast with the thermal behavior usually observed in conventional JJs (see Fig. 3.2.b). Therefore, phase dynamics of junction 11c substantially follows what commonly observed in LTS JJs, except for the thermal dependence of I_{c0}. SCD measurements require very high resolution but constitute a powerful tool to investi-

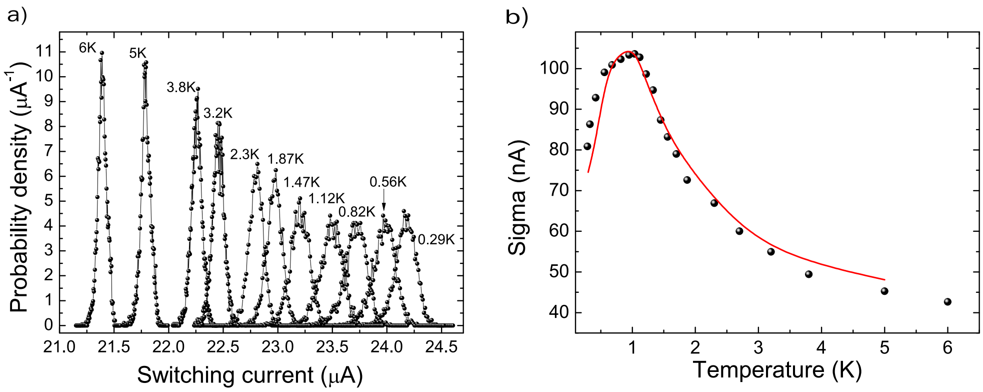

Figure 3.13: a) SCDs measured at different bath temperatures from 0.29K up to 6K for junction 12b. b) Thermal dependence of σ (black points). The red line is the result of numerical simulations based on multiple escape and retrapping processes in the wasboard potential.

gate not only phase dynamics of HTS systems but also unusual I_c(T) dependences of such structures[23]. I_c(T) dependence may discriminate proximity effect[3, 4]. In weak links and in HTS, Andreev bound states contribute differently because of the various OP configurations of the electrodes[23].

The second sample reported in this section is junction 12b whose $I-V$ characteristic at 20mK is shown in Fig. 3.12.a. The SEM image of the device is illustrated in Fig. 3.12.b. In Fig.3.13.a we report the SCDs collected over a wide range of temperatures in absence of magnetic field. A transition from TA to PD regime is observed at T*=1.0K. Below 1.0K the histograms broaden when increasing the temperature. Above the transition temperature T^* the histograms shrink with a consequent increase of their amplitude and the temperature derivative of σ(T) becomes negative (see Fig. 3.13.b). Experimental data have been compared with Monte Carlo simulations based on the model of Fenton and Warburton[50] described in section 3.3. The numerical outcomes are shown by the red line in Fig. 3.13.b and the agreement with the data is excellent with Q=1.17±0.02. The dissipative essence of the quality factor Q strongly depends on the value of the effective frequency dependent resistance R(ω) and of shunting capacitance C, which are in turn determined by several interplaying effects, such as circuit impedance, subgap resistance, stray capacitance[31] and GB microstructure in HTS JJs. Since these parameters are not easily accessible, a reliable way able to estimate the quality factor Q in the MDR, both for LTS and unconventional superconductors, as well as for hybrid systems, is of great interest.

3.6 Direct transition from MQT to phase diffusion in YBCO grain boundary Josephson junctions

The possibility to have extremely low I_c can be functional to investigate phase dynamics at extreme conditions. An example is given by a recent experiment on submicron Nb/AlOx/Nb junctions[48]. Data show an anomalous $\sigma(T)$ dependence with a negative $d\sigma/dT$ over the entire temperature range. This regime can be achieved by engineering junctions with lower critical current and junction capacitance, such that the ratio I_{c0}/C, which regulates T_{cross}, is constant and the transition temperature T^*, which scales with the Josephson energy[36], is lower or comparable to the quantum crossover temperature T_{cross}. Another example is given by the work by Yoon et al.[135]. They have engineered Al/AlOx/Al JJs in order to obtain low critical currents, of about 400nA, and low capacitance, of about 40fF, at the same time. In this way they have observed that TA is completely suppressed since T^* is lower than T_{cross}. On the other hand, TA regime is recovered by adding a shunting capacitance in the device circuit, and this demonstrates that the capacitance can be used in order to tune the phase dynamics. Neverthless, a solid self-consistent method to characterize the dissipation level in MDR is missing. In particular, the approach used in Ref. [48] seems to provide estimates of the damping factor and of junction parameters which are not self-consistent from one sample to the other. Junctions with intrinsically low J_c and high level of dissipation, such as HTS GB junctions, could rather represent an interesting term of comparison to study these kinds of unconventional regimes using standard micrometer junctions, since they may cover a wide range of junction parameters[49, 110].

In this section measurements on YBCO GB biepitaxial JJs based on LSAT substrate are reported. The new design fully responds to the task of reducing stray capacitances. The resulting devices constitute a relevant

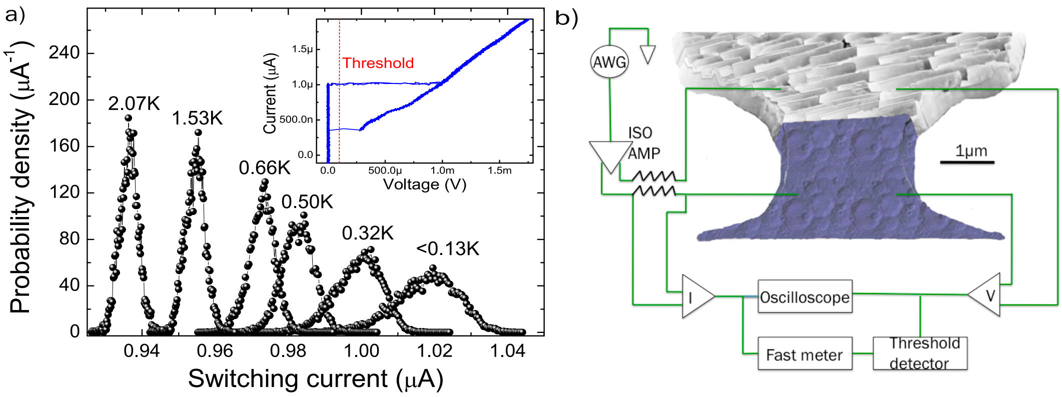

Figure 3.14: a) SCDs measured on YBCO GB LSAT-based 16a junction. The inset shows the $I-V$ characteristic measured at 20mK. The reference value for the threshold detector is displayed by the red dashed line. b) Picture of the junction along with a block diagram of the measurement setup. In the bottom part of the image in blue is the YBCO (001) electrode while in the top part in gray the needlelike YBCO (103) grains are shown (adapted from [56]).

term of comparison to search the origin of the capacitive effect in GB JJs, on average one order of magnitude lower than those measured on STO-based devices[24, 55], and is more representative of the intrinsic nature of the GB[55, 56], as demonstrated by the final results.

The samples reported in this section are junction 16a and 4S with interface orientations of 75^o for sample 16a and 50^o for sample 4S respectively. For such angles a robust overlap of the d-wave lobes on both sides of the junctions is expected[55, 60, 134]. For junction 16a, the thickness of the YBCO film is about 100nm while the width of the junction is 2.5μm (see the SEM image in Fig. 3.14.b). For junction 4S the YBCO film is 200nm thick and the width is 1.5μm. The $I-V$ characteristic of junction 16a measured at 20mK is shown in the inset of Fig. 3.14.a: $I_c \simeq$1μA, $R_n \simeq$1KΩ and V_{sw}=1mV. In this case the current ramp rate is dI/dt=30μA/s and the usual tecnique has been used for the measurements of the switching histograms (the threshold voltage is displayed by the red dashed line in the inset of Fig. 3.14.a).

SCDs collected over a wide range of temperatures on sample 16a are reported in Fig. 3.14.a, while those collected on junction 4S are shown in Fig.

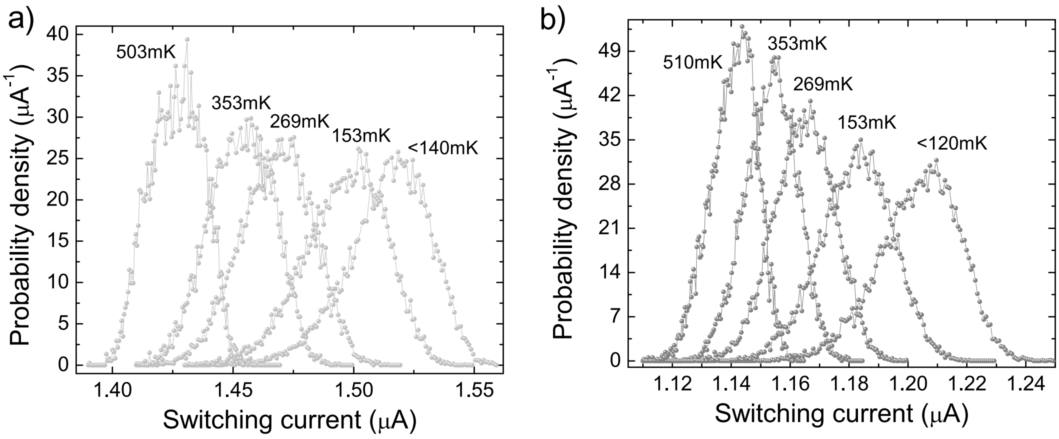

Figure 3.15: SCDs as function of temperature measured on YBCO GB LSAT-based 4S junction for H=0 (a) and H=12G (b) respectively. Above the crossover temperature T_{cross} (T_{cross} ≃140mK in (a) and T_{cross} ≃120mK in (b)), the histograms shrink rather than broaden and become more symmetric, since retrapping processes play a relevant role.

3.15.a and in Fig. 3.15.b for two different values of the magnetic field (H=0 and H=12G respectively). The temperature dependence of σ of the SCD curves for both the samples is shown in Fig.3.16.a. Our data are characterized by two distinct regimes. In Fig.3.14.a, increasing the temperature above 130mK the switching current histograms shrink rather than broaden, which corresponds to the negative temperature derivative of σ in Fig.3.16.a. This behavior is consistent with a diffusive motion due to multiple escape and retrapping processes in the potential wells. The σ dependence has been fitted through Monte Carlo simulations[50, 56] (see section 3.3) with a damping factor Q=1.30±0.05 (light grey line in Fig. 3.16.a). In the same way, the damping factor for junction 4S has been estimated (Q=1.28±0.05).

Below 130mK, histograms overlap and σ saturates, which is a typical signature of a quantum activation regime. In analogy to what commonly done to prove MQT in underdamped junctions[14], the magnetic field has been used to tune in situ the quantum crossover temperature T_{cross} to unambiguously prove MQT as source of the saturation of σ below T_{cross}. In the inset of Fig. 3.16.a the thermal dependence of σ for the junction 4S at H=0 and H=12G (light gray and gray circles respectively) is reported. Again the magnetic field reduces at the same time I_{c0} and T_{cross} and induces smaller

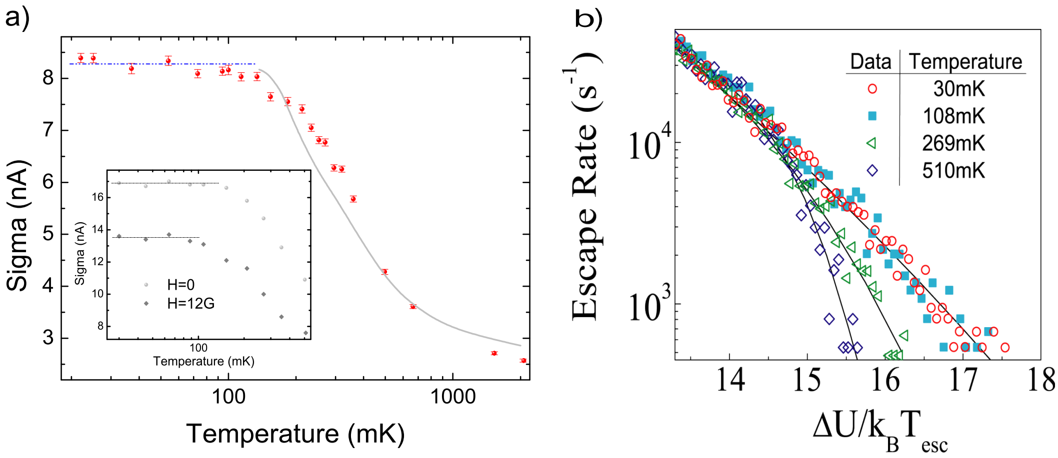

Figure 3.16: a) Thermal behavior of σ of the SCDs measured on junction 16a (red circles). The light grey solid line is the result of Monte Carlo simulations in the PD with a quality factor Q=1.30, while the blue dashed line indicates the saturation of σ below T_{cross}. The inset shows temperature dependent data for sample 4S at H=0 and H=12G. The black lines indicate the average values of σ in MQT regime and the value of T_{cross}, which are both reduced by the magnetic field. b) The experimental escape rates (symbols) as a function of ΔU/k$_B T_{escape}$ along with the numerical fits at different temperatures for junction 4S are shown. The Q value used for the fits is Q=1.28.

values of σ[56, 111].

Phase diffusion also appears in the escape rates Γ, shown in Fig. 3.16.b, as a function of the ratio between the barrier height ΔU and the escape energy k$_B$T$_{escape}$. Differently from the measurements on NbN JJs (see section 3.3), T_{escape} has been used instead of T since the escape is dominated by quantum effects at very low temperature (see section 1.1 and Ref. [14]). Below T_{cross}, the escape rates approximately fall on a straight line according to MQT escape rate (Eq. 1.6), while above T_{cross} retrapping processes cause a bending in Γ versus ΔU/k$_B T_{escape}$ curves[34, 56]. I_{c0} has been fitted from the fits of the probability density in the quantum regime (I_{c0}=1.20$\pm$0.02μA for junction 16a and I_{c0}=1.79$\pm$0.03μA for junction 4S). On the basis of Q, I_{c0} and T_{cross}, C=64fF and R=85Ω for junction 16a, C=74fF and R=64Ω for junction 4S. The specific capacitance for both samples is about 2$\cdot$10^{-5}F/cm^2[55].

Relevant device parameters of the junctions discussed in this and in the

Table 3.2: Summary of device parameters of the YBCO JJs reported in this chapter. Errors are reported in the text in the various sections.

Sample	Angle (^{o})	I_{c0} (μA)	J_c (A/cm^2)	Q	C (fF)	R (Ω)	T_{cross} (mK)
4S-LSAT	50	1.79	$5 \cdot 10^2$	1.28	74	64	145
16a-LSAT	75	1.20	$5 \cdot 10^2$	1.30	64	85	135
11c-STO	50	5.20	$3 \cdot 10^3$	1.40	1000	11	50
12b-STO	55	26.0	$7 \cdot 10^3$	1.17	1000	5	NA

previous section are reported in Table 3.2. The damping parameter is of the order of 1 and all the junctions fall in the MDR. On the other hand, the tuning of the capacitive effects has important consequences: STO-based junctions have a capacitance one order of magnitude larger than LSAT-based junctions, therefore the quantum crossover temperature is lower for STO-based junctions[24]. In addition, LSAT-based junctions have lower critical currents, thus the transition temperature T* is reduced with respect to STO-based devices. Therefore, taking advantage of the design flexibility of the YBCO GB biepitaxial JJs[24, 55], we have substantially engineered devices with T*<T_{cross}[56], to which correspond a direct transition from MQT to the PD regime, and TA is completely suppressed. For temperatures well below T_{cross}, MQT contributions to escape rates are larger than those coming from both thermal escape and retrapping processes, while above T_{cross} the retrapping rate dominates over thermal and quantum escape rates (see Fig. 3.17).

The contiguity between quantum escape (T< T_{cross}) and PD (T> T_{cross}) leads to MQT phenomena characterized by low Q values and not necessarily to quantum PD. This phenomenology is quite distinct from all previous studies[31, 34, 35, 36, 46, 47, 50], where in the transition to quantum activation, retrapping processes decay faster than thermal escape, and from the work of Yu et al.[48], where the occurrence of a quantum activated PD has been claimed. In Ref. [48], the semiclassical nature of their quantum PD is testified by the dependence of σ on the temperature over the entire temperature range, and the transition is as a matter of fact revealed by a change of the temperature derivative of σ[48]. MQT processes are substantially fol-

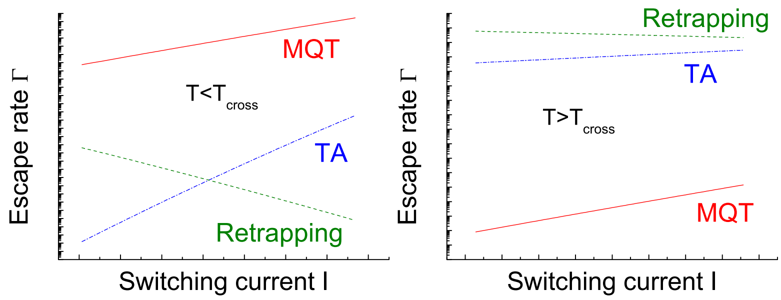

Figure 3.17: Schematic escape rates of MQT, TA, and retrapping processes at $T < T_{cross}$ (left panel) and at $T > T_{cross}$ (right panel)

lowed and assisted by thermally-ruled retrapping processes. However, a fully quantum account of phase fluctuations passes through the condition of a Josephson energy much larger than Coulomb energy, $E_J >> E_c$, given by Iansiti et al.[30]. E_J and E_c have been defined in chapter 1; according to the estimates of I_{c0} and C, we obtain $E_J/E_c \simeq$1000 for both the junctions 16a and 4S. Thus the condition $E_J \simeq E_c$ is not satisfied both in the present experiment and in the work of Yu et al.[48]. Phase dynamics in the unusual regime $E_J \simeq E_c$ will be addressed in the next chapter.

Monte Carlo simulations have been performed for different values of the quality factor Q ranging from 1 to 5. Only TA and PD processes have been calculated in the graphs reported in the inset of Fig. 3.18.a. For each of these curves, T^* indicates the transition temperature from TA to PD regime. Q tunes T^* and modifies the slope of the σ(T) fall-off at higher temperatures. The capability to numerically reproduce this region makes it possible to estimate Q with high precision. The section below T^* reproduces the expected $T^{2/3}$ dependence for a thermally activated regime[8] (red solid line) as an additional test of consistency. In Fig. 3.18.a, the MQT section is missing. It would attach below T_{cross} to each of the curves with its characteristic saturation in σ, as shown in Fig. 3.16.a in fitting experimental data.

Such numerical simulations also allow us to fully reconstruct the (Q, k_BT/E_J) phase diagram illustrated in Fig. 3.18.b[35, 56]. The transition curve between the PD regime and the running state following thermal or quantum activation has been determined numerically by varying the quality factor Q as function of the ratio between the thermal energy and the Josephson energy. The coloured symbols in the phase diagram are (Q, k_BT^*/E_J)

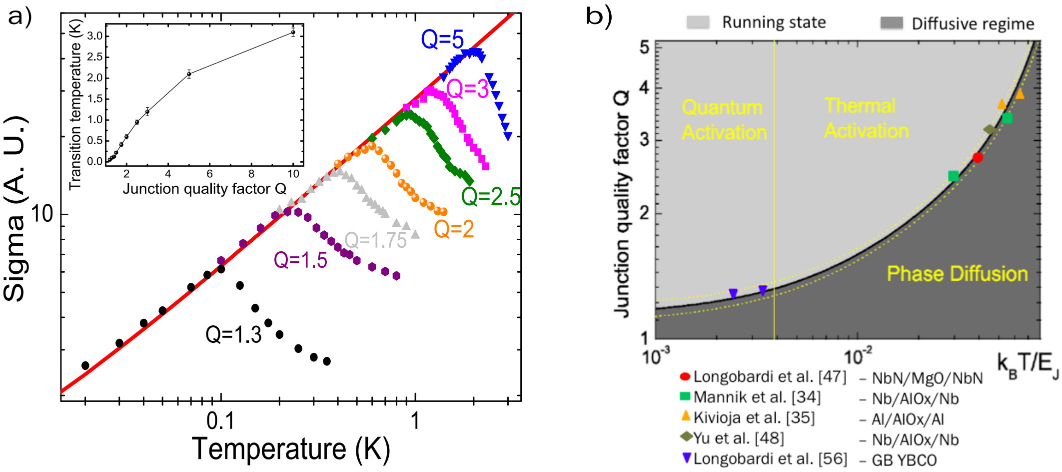

Figure 3.18: a) Simulated thermal behavior of σ for several values of the Q damping parameter. In the inset we report the dependence of the transition temperature T^* on the damping parameter. b) $(Q, k_BT/E_J)$ phase diagram, showing the various activation regimes. The transition curve (black line) between the PD regime and the running state has been extrapolated through numerical simulations, the sideband curves (yellow dashed lines) mark the uncertainty in our calculation and are due to the temperature step size. The symbols refer to various works reported in the literature in the last ten years. The good agreement between experiments and simulations certifies the universal character of the phase diagram. Finally, the transition curve between quantum and thermal activation (yellow line) depends on E_J and is peculiar of samples 16a and 4S.

values derived from several experiments pointing to PD both in LTS and HTS JJs[34, 35, 47, 48, 56]. The proximity of experimental data to the simulations suggests the validity of such approach and the universal nature of the transition curve. On the other hand, the transition between thermal and quantum activation (yellow line in Fig. 3.18.b) is function only of E_J and is peculiar of junctions 16a and 4S. Finally, the experiments discussed in this section contribute to settle an uneploxed region of the phase diagram and a clear ground to quantify to some extent dissipation in the MDR is achieved through direct comparison between measurements and numerical simulations[49, 110]. The methods illustrated in this chapter provide the estimate of the junction parameters in a self-consistent way and phase dynamics has been described in terms of 3 quantities: the temperature T, the Josephson energy E_J and the quality factor Q. Such phase diagram represents a guideline for very reduced size JJs and for superconducting hybrid nanoscale devices[32, 33].

Chapter 4

Phase dynamics at extreme conditions

In the previous chapter the phase dynamics of moderately damped YBCO GB JJs has been described in terms of the operational temperature, of the Josephson energy and of the quality factor (see Fig. 3.18.b). As shown in Table 4.1, the junctions reported in the previous chapter have critical current density J_c of the order of 10^2-10^3A/cm^2. For these values of J_c in micrometric and sub-micrometric JJs, we have given a robust evidence of MQT, TA and PD regime, consistently with what commonly observed on other systems[14, 31, 34, 35, 36]. In this case I_c values of the order of a few μA are obtained and the condition $E_J >> E_c$ is satisfied.

The topic of this chapter is the study of phase dynamics in a wider and unconventional range of junction parameters: we will span a very large set of J_c, both very low J_c (the first two devices reported in Table 4.1) and relatively high J_c (the last junction in Table 4.1). Each of these junctions has been measured for several weeks. They have been selected in chips, each containing not less than 50 junctions. Their behaviors are characteristic of GB and JJs, covering quite a wide range of junction parameters. The former case of low J_c is obtained by reducing the GB dimensions of LSAT-based JJs down to 600nm of width. As discussed in the next section, such devices in the submicron range are strongly affected by oxygen desorption, thus, depending on the GB configuration, J_c one or two orders of magnitude lower

Table 4.1: Summary of device parameters of the YBCO JJs reported in the previous chapter (black) and in this chapter (red). The samples are ordered according to increasing values of J_c.

Sample	Angle (^{o})	Width (μm)	I_{c0} (μA)	J_c (A/cm^2)	E_J (meV)	E_c (μeV)
6W-LSAT	60	0.6	0.035	5	0.07	45
1W-LSAT	90	0.5	0.13	65	0.27	45
4S-LSAT	50	1.5	1.79	$5 \cdot 10^2$	3.7	1.1
16a-LSAT	75	2.5	1.20	$5 \cdot 10^2$	2.5	1.2
11c-STO	50	0.8	5.20	$3 \cdot 10^3$	10.8	0.1
12b-STO	55	1.5	26.0	$7 \cdot 10^3$	54	0.1
11a-STO	50	0.2	50	$9 \cdot 10^4$	100	0.8

than micrometric LSAT-based JJs is obtained, and the critical current is scaled down to a few nA. The latter case is obtained by reducing the GB barrier in the twist configuration[23, 54, 60], since in such configuration the transport occurs along the point contacts of CuO_2 planes (see sections 1.3 and 4.4).

Therefore, in the first two sections of this chapter, phase dynamics of very low J_c JJs in the unusual condition $E_J \approx E_c$ (see Eqn. 1.3) will be addressed. This energy scale favours the access to the quantum phase diffusion regime, which is quite unexplored and whose nature is still unsettled[30, 37, 48, 136]. Such issue is of broad interest due to the difficulty of reaching this limit also for LTS JJs. In addition, ultrasmall HTS junctions have been used to realize single electron transistors with unprecedented energy resolution[137] and have been proposed for ultra sensitive SQUIDs to use in the detection of small spin systems[138]. These efforts basically respond to the need for a systematic and reliable study of their phase dynamics.

In the third section, switching processes in nanowires and phase-slips mechanisms (see section 1.5) will be addressed[91, 92]. A subtle path exists between these systems and JJs with analogies and distinctive features. In the last section a comparative study of switching measurements between moderately damped JJs discussed in the previous chapter and junction 11a will be shown, the aim is to identify and to distinguish the transport modes and the border between the two distinct regimes of the Josephson effect and of phase-slips, in view of a wider phase diagram for superconducting weak links[49, 56].

4.1 Phase delocalization in the washboard potential

In the previous chapter moderately damped LTS and HTS JJs have been investigated through the analysis of the SCD histograms[47, 49, 56, 111]. All these devices are characterized by values of the Josephson energy E_J much larger than those of the charging energy E_c. Devices characterized by $E_J \approx E_c$ were first studied by Iansiti et al.[30] using Sn based junctions with nominal cross section of $0.1\mu m^2$ and I_c in the range of a few nA.

When the condition $E_J >> E_c$ is satisfied, the state of the system (see Eqn. 1.3) is obtained by the minimization of the energy by a classically well defined φ value at the minimum of a well of the washboard potential[30, 37]. In the opposite limit, when the charging energy is dominant, quantum fluctuations in φ are very large and the quantum mechanical conjugate Q (the charge difference between the two electrodes) may now be treated classically. The value of the ratio $x = E_c/E_J$ is a measure of how strongly the charging energy acts in delocalizing the phase, being related to the width of the phase wave function[30] $\psi(\varphi)$: $\delta\varphi = (x)^{1/4}$. For $x << 1$ $\psi(\varphi)$ is a narrowly peaked function. In this situation the phase can be treated as a semiclassical quantity, since fluctuations in φ are very small, and there are many excited states in each well of the washboard potential. For values of x larger than 1/4 the phase variable is sufficiently delocalized that quantum fluctuations cannot be neglected and quantum uncertainty, especially at low temperatures, has to be taken into account[30].

From the experimental point of view, delocalization effects reflect in the appearance of both a diffusion branch in the $I-V$ characteristic and a finite resistance at low voltages R_0 in the superconducting branch, as shown in Fig. 4.1.b[136]. Such finite resistance is due to diffusion of the phase in the washboard potential also at very low bias currents. In the presence of a bias current I the tunneling probability of the expectation value of the phase φ

is greater in the downhill direction than in the uphill one, resulting in a net rate of tunneling proportional to I. On the other hand, there is sufficient damping that, below a critical current set by the binding energy E_B (see next section), after an event of escape through the barrier the phase is retrapped in the well into which it has just tunneled. This description corresponds to the appearance of a small voltage $V \propto d\varphi/dt \propto I$, which gives rise to R_0. R_0 is proportional to the tunneling rate[30] $R_0 \approx \frac{h}{2eI}\Gamma$ and Γ can be calculated by using the Caldeira-Leggett approximation in presence of dissipation[1]. This picture is strictly valid in absence of thermal fluctuations. Since the condition $E_J \approx E_c$ is obtained by reducing the critical current to a few nA, at higher temperatures the condition $E_J \approx k_B T$ is also satisfied. Therefore, thermal fluctuations are responsible of very frequent escape and retrapping events at higher temperatures, while quantum fluctuations become dominant at low temperatures. In the former case the low voltage resistance R_0 is the result of thermal fluctuations and depends on temperature (see Fig. 4.1.b), in the latter case R_0 is caused by quantum fluctuations and is temperature independent[30, 136].

A quantitative analysis could be performed using SCD histograms. However, due to the extremely low values of the critical currents, such measurements are extremely difficult to perform. As discussed in the next section, for such low values of E_J, the ratio between σ and the mean switching current is of the order of 10^{-3}, thus $I_c \simeq$10nA would implicate $\sigma \simeq$10pA. Therefore, in the next section the analysis of sub-micrometric GB YBCO JJs is carried out using measurements of the $I-V$ characteristics at different temperatures. Numerical methods on the basis of the frequency dependent damping Kautz-Martinis[31] (KM) model (the equivalent circuit is shown in Fig. 4.1.a) have been developed in order to study the phase dynamics in the classical regime at higher temperatures, while arguments developed by Iansiti et al.[30] have been used when quantum fluctuations become relevant at low temperatures.

In order to approach the quantum phase diffusion regime, we have realized junctions with lateral size down to 600nm, obtaining I_c of the order of few tenths of nA[136]. We have extended the nanolithography approach recently reported for YBCO off-axis biepitaxial junctions on STO substrates[134] to LSAT substrates[55], in collaboration with NEST-Scuola Normale Superiore of Pisa. The reduction of the junctions size is an effective tool to reduce

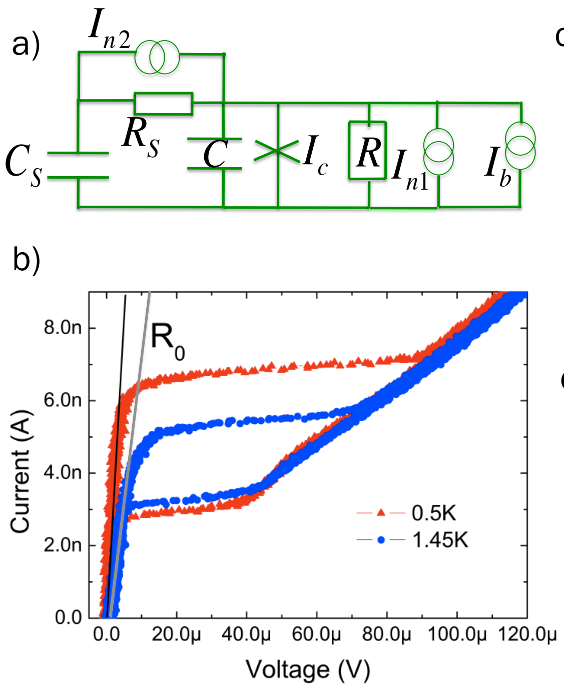

Figure 4.1: a) Equivalent circuit of a real JJ, according to the frequency dependent damping Kautz-Martinis model (adapted from [31]). C_S and R_S are the the shunting capacitance and resistance respectively, associated with the external circuit connected to the junction, while I_{n1} and I_{n2} are the noise currents associated with the intrinsic resistor R and the shunting resistor R_S respectively. b) $I-V$ characteristics measured on junction 6W at 0.5K (red triangles) and at 1.45K (blue circles). In this figure the main features of the phase dynamics in the condition $E_J \approx E_c$ are shown: very low critical current of the order of a few nA, coexistence of hysteresis and PD bending and a low voltage resistance R_0 which is function of the temperature (the gray line at 1.45K and the black line at 0.5K). c) and d) are SEM images of junctions 1W and 6W respectively. The nominal width is 600nm for both devices.

the influence of GB microstructure on the transport properties and better isolate the intrinsic junction behavior[134]. The definition of the sub-micron bridges is carried out using an electron beam lithography technique, adapted to HTS requirements[139]. The electron beam pattern is transferred to a 80nm thick Ti layer which serves as a hard mask. The YBCO not covered by the Ti mask is removed using ion beam etching (IBE), keeping the sample at low temperature (120K) in order to minimize oxygen loss. After this, the Ti mask is removed by chemical etch in a highly diluted (1:20) HF solution. In Fig. 4.1.c and Fig. 4.1.d SEM images of 600nm wide devices 1W and 6W respectively are shown. The high quality of the YBCO film is testified by the systematic presence of elongated grains with typical size of 1μm in the (103) part and by the absence of impurities and outgrowths in the (001) part[54].

4.2 Approaching quantum phase diffusion in sub-micrometric YBCO grain boundary structures

$I-V$ characteristics of the two devices 1W and 6W are shown in Fig. 4.2.a and in Fig. 4.2.b respectively at different temperatures. The magnetic field patterns are regular and Fraunhofer-like[136], as predicted for ideal JJs[3, 23]. Taking into account focusing effects[140], the pattern periodicity in field points to an effective width of ≈500nm for junction 1W and of ≈600nm for junction 6W[136]. These values are very close to the nominal dimensions of the devices. The estimated J_c is 65A/cm^2 for junction 1W and 5A/cm^2 for device 6W.

The low J_c values of these devices are a consequence of oxygen depletion, occurring especially in the GB region. This is a quite general feature of HTS JJs[23] and is expected to be of particular relevance when decreasing the size of the junction, as in this case. We have found that the devices realized using LSAT as a substrate are characterized by higher R_n values and are more affected by aging when compared with the ones fabricated on STO substrates. These micro structural factors could in this case mask the influence of the d-wave OP in determining the magnitude of J_c as a function of the junction

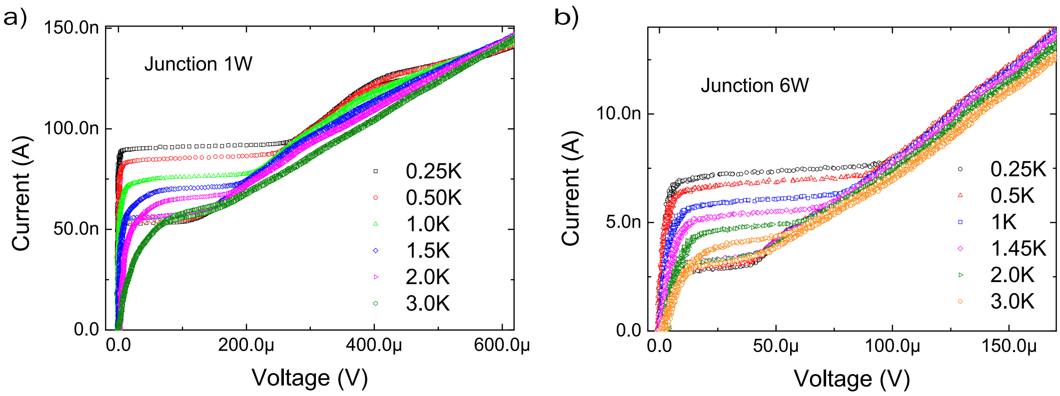

Figure 4.2: $I-V$ characteristics of junction 1W (a) and of junction 6W (b) respectively, measured in a wide rage of temperature from 0.25K up to 3K.

misorientation[60]. Grains elongated in the current direction in the device 1W (see Fig. 4.1.c), for instance, might be less exposed to oxygen desorption compared to grains leaning against the walls of the channel in device 6W (see Fig. 4.1.d), explaining the different values of I_c measured for these two devices[136].

The reduction of J_c offers the possibility to have access to junction regimes which have been poorly explored. The Josephson energy E_J is $\simeq 270\mu$eV for device 1W and 70μeV for device 6W. E_J has been calculated for both the junctions from the fitted I_{c0} values according to the frequency dependent damping KM model (see Fig. 4.1.a), as discussed in the following of this section. Such values are one or two orders of magnitudes smaller than those measured for junctions where macroscopic quantum behavior has been demonstrated[24, 56], and five orders of magnitude smaller than what observed in most HTS Josephson devices[23, 51]. More importantly, for device 6W, E_J is comparable with the charging energy E_c.

The $I-V$ characteristics shown in Fig. 4.2.a and 4.2.b are highly hysteretic, with a difference between the critical and the retrapping current up to 70% at the lowest temperature. Remarkably, the neat hysteresis coexist with a slope at low voltage, which is an hallmark of PD effects[31] (see Fig. 4.1.b and sections 1.2 and 4.1). The low voltage slope, to which corresponds a finite resistance R_0, is visible in Fig. 4.2.a (junction 1W) for temperatures larger than 2K, and in Fig. 4.2.b (junction 6W) in the whole temperature range down to the 0.25K.

In order to study the phase dynamics through measurements of $I-V$ characteristics, we use the frequency dependent damping KM model[31] (the corresponding circuit is reported in Fig. 4.1.a). Conservation of current at nodes and Josephson equations imply the following normalized Langevin equations for the phase φ and the voltage V_b at the external circuit capacitance C_S:

$$\begin{aligned}\ddot{\varphi} &= Q_0^{-2} \cdot ((V_b - \dot{\varphi})(Q_0/Q_1 - 1) - \dot{\varphi} - \sin\varphi + \gamma_b + \gamma_{n1} + \gamma_{n2}) \\ \dot{V}_b &= \rho Q_0^{-2} \left((\dot{\varphi} - V_b) + \gamma_{n2}/(Q_0/Q_1 - 1)\right)\end{aligned} \tag{4.1}$$

In the equations above time is normalized to $\hbar/2eI_{c0}R = \omega_0^{-1}/Q_0$ and currents to critical current I_{c0}. $Q_0 = R\sqrt{2eI_{c0}C/\hbar} = \omega_0 RC$ and $Q_1 = (1/R + 1/R_S)^{-1}\sqrt{2eI_{c0}C/\hbar} = \omega_0 R_S C$. The term $(V_b - \dot{\varphi})(Q_0/Q_1 - 1)$ represents the normalized current through the external load R_S, $\rho = RC/R_S C_S$ is the time constant ratio, γ_b is the normalized bias current and γ_{n1} and γ_{n2} are the normalized noise currents, associated with the intrinsic resistor R and the external resistor R_S respectively. These are modelled as Gaussian stochastic processes with zero mean and variance given by:

$$\langle \gamma_{nk}(t), \gamma_{nk}(t') \rangle \equiv \sigma_k^2 \delta(t - t') = \alpha_k \frac{2k_B T}{E_J} \delta(t - t') \tag{4.2}$$

with α_1=1 and α_2=$Q_0/Q_1 - 1$. This simple model is able to reproduce the main features of PD in the $I-V$ characteristics[31] without the use of other parameters. As discussed in section 3.3, simulations of Langevin equations have been made generating Gaussian noise by cernlib RANLUX routine[77]. Other details of numerical integration can be found in Ref. [77]. In order to capture the PD regime in the $I-V$ characteristics an average procedure over 2000 or 3000 single $I-V$ was performed depending on temperature. Each single $I-V$ was generated by averaging over 2000 time units.

Fig. 4.3.a shows the comparison between the experimental data of device 1W measured at three different temperatures (left side) and numerical simulations based on Eqn. 4.1 (right side). Significant changes in the shape of the $I-V$ curves take place when cooling down from 2.0K, where the $I-V$ exhibits a small hysteresis of 15% and a pronounced rounding of the low voltage branch, to 0.25K, where the hysteresis reaches 40% and a sharp switch from

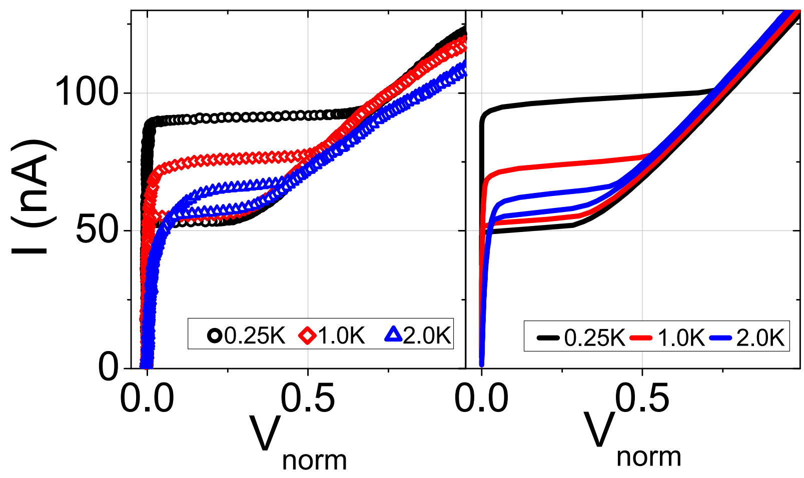

Figure 4.3: Experimental $I-V$ characteristics (left panel, symbols) measured at T=0.25K, 1.0K and 2.0K are compared with Monte Carlo simulations (right panel, full lines). Good agreement is achieved using the following parameters: Q_1=0.6, Q_0=5 and I_{c0}=130nA.

the superconducting to the resistive branch is observed. The simulations well reproduce experimental data in terms of critical current, amplitude of the hysteresis and coexistence of hysteresis and PD bending[136]. From the simulations, dissipation levels of Q_1=0.6±0.1 and Q_0=5±0.5 are obtained. The estimated critical current is I_{c0}=130nA.

The experimental I_c measured at 0.25K is only 70% of the I_{c0} value used for the simulations. This difference arises since the small E_J means that, at 0.25K, $k_B T/E_J \simeq 1/10$ and so thermal noise currents (whose amplitude is proportional to $(k_B T/E_J)^{1/2} \simeq 0.31$) have a significant effect.

For this device, we have measured the SCD histograms at various temperatures, reported in Fig. 4.4.a. The standard deviation σ of the experimental histograms decreases as the temperature increases (black circles in Fig. 4.4.b), as expected in the PD regime. The ratio between σ and the mean switching current is in the range 10^{-3}, in agreement with that found in the literature[141]. In Fig. 4.4.a and in Fig. 4.4.b we also show the numerical simulations of the SCD histograms (red lines). Such simulations have been realized using the following parameters: Q_1=0.6, Q_0=2, I_{c0}=130 nA. As ex-

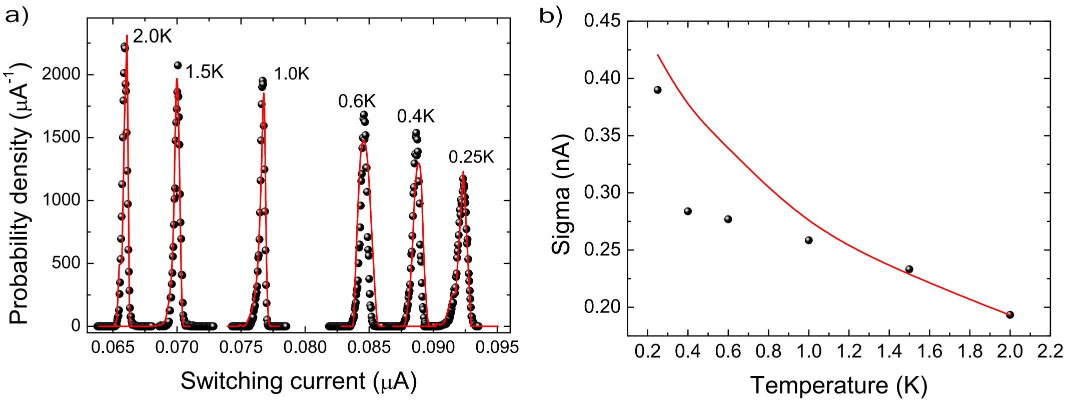

Figure 4.4: a) Experimental (black points) SCD histograms measured at different temperatures are shown, along with the outcomes of numerical simulations (red lines). b) Thermal dependence of σ (black points) of the SCDs shown in (a) is compared with Monte Carlo simulations (red line). The junction is in the PD regime in the whole temperature range analyzed.

plained in section 3.3, the study of the switching behavior of JJs in the MDR is usually performed using a single Q model to fit the experimental SCD histograms[34, 35, 47, 50] by putting Q_0=Q_1. Such procedure works well when the condition $E_J/k_BT>>1$ is satisfied and the high frequency quality factor is larger than one. In this case, Q_1=0.6 and therefore, in order to preserve the underdamped dynamics of the phase after the escape process, the KM model requires a slight increase of the low frequency quality factor Q_0 with respect to Q_1. Finally, Q_0=2 is the lowest value for which a good agreement between experimental histograms and numerical simulations has been achieved. It is important to recall that in the case of the $I-V$ curves Q_0 is a fitting parameter which is related to the return current and the amplitude of the hysteresis, while in the case of the SCDs Q_0 has to be interpreted as a stability parameter that should be used in the KM model at extreme conditions of very low critical currents and high dissipation.

We point out that experimental reports showing the occurrence of PD effects both in the $I-V$ curves and in the SCD histograms are extremely rare. This combined analysis has previously been carried out, to our knowledge, only in Ref. [141] where, contrary to what happens in our case, the main contribution to the damping of the devices comes from the external impedance, and the junction intrinsic resistance plays no significant role. In our case, the reduced value of E_J makes PD effects become evident not only in the behavior of the SCD histograms, but also in the shape of the $I-V$ characteristics, thereby offering two independent routes for the study of PD in the MDR.

Once retrieved the classical PD behavior in the $I-V$ characteristics of sub-micrometric HTS junctions, we turn to the possible quantum phase diffusion regime in device 6W, where E_c is comparable with E_J. This regime can be obtained by reducing either the I_c value or the capacitance. From the simulated curves, for junction 1W a specific capacitance of 1.5×10^{-6} F$\cdot$cm^{-2} (consistent with what observed in wider junctions[55]) and an effective resistance of 500Ω are obtained. In our case, the devices are defined on the same chip and the capacitance can reasonably assumed to be constant, while I_c is reduced of a factor of 10 when compared to junction 1W, leading to a ratio of E_J/E_c of about 1.5 ($E_c\simeq45\mu$eV). This value falls in the region where quantum phase diffusion could take place. In Fig. 4.5.a we compare the experimental $I-V$ curves of device 6W (left panel) with simulations (right panel). The most relevant difference with the previous device is the impossibility to find a single set of parameters which could reasonably reproduce the $I-V$ curves in the whole range of temperature. Agreement with the main features of the experimental data is obtained at high temperature (T=1.45K) by using the following parameters: Q_1= 0.6, Q_0=12 and I_0=35nA[136]. The fact that Q_0 for junction 6W is larger than Q_0 of junction 1W suggests an increase in effective resistance for device 6W, prevailing on the reduction of I_c. Iansiti et al.[30] pointed out that the $I-V$ characteristic becomes more resistive in the low voltage regime since charging effects become more relevant when reducing the E_J/E_c ratio. However, the intrinsic origin of the reduction of dissipation in the junction with lower I_c remains unclear. Once demonstrated that it is possible to achieve a regime where the scaling energies E_c and E_J are comparable, only a more systematic study could give additional hints on possible microscopic factors, in particular the relation between a d-wave OP symmetry and dissipation.

Remarkable deviations appear when reducing the temperature down to 0.25K and signal a transition from a classical regime, in which thermal fluctuations dominate and the experimental data are well reproduced using the

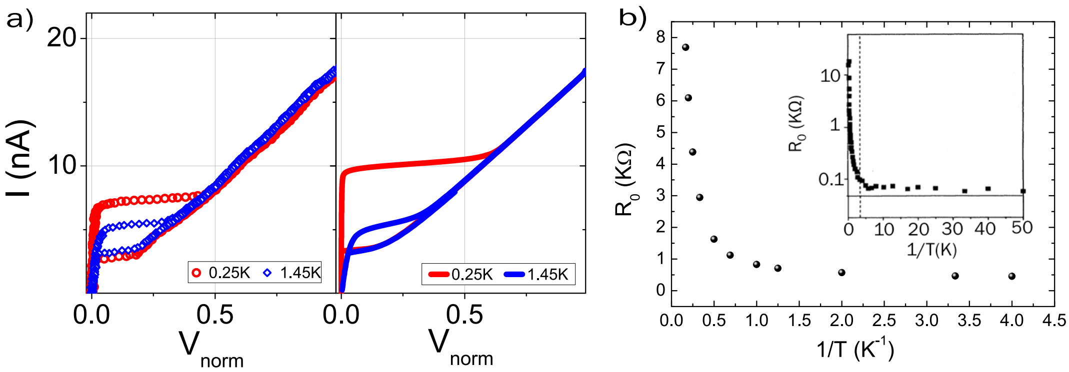

Figure 4.5: a) $I-V$ characteristics of device 6W (symbols, left panel) measured at T=0.25K and at T=1.45K compared with Monte Carlo simulations (full lines, right panel) using Q_1=0.6, Q_0=12 and I_{c0}=35nA. Good agreement is achieved at 1.45K, while important deviations are evident at 0.25K. b) Measured low voltage resistance R_0 as function of 1/T is shown. Above $3K^{-1}$ (T$\simeq$0.3K) R_0 tends to saturate, indicating the transition to the quantum regime. As a term of comparison, R_0(1/T) dependence reported by Iansiti et al.[30] is shown in the inset. For such device x$\simeq$0.25, thus a lower R_0 value is found in the quantum regime and saturation is observed at lower temperatures ($\simeq$150mK) (the inset has been taken from Ref. [30]).

frequency dependent damping model, to a quantum regime in which phase delocalization plays a key role in the dynamics. An evident difference between the experimental $I-V$ measured at 0.25K and Monte Carlo simulations is the value of the critical current. For junction 6W, $x \simeq$0.65 and the width $\delta\varphi$ is ≈ 0.9, smaller than the width of the potential well. Although the phase φ is still confined in one well of the washboard potential, the barrier height of such a well, which depends on both E_J and E_c, is reduced, influencing the critical current. For x>1/4, the critical current is scaled by the ratio E_B/E_J where E_B is the binding energy and represents the minimum energy of the delocalized wave function[30]. As remarked by Iansiti et al.[30], according to the weak binding approximation the binding energy is given by:

$$E_B \approx E_J 2x[(1+1/8x^2)^{1/2}-1] \tag{4.3}$$

leading to a temperature independent I_c=$2eE_B/\hbar$ which is less than the value I_{c0}=$2eE_J/\hbar$ which would be observed in the absence of quantum fluctuations. Using the values of E_J and x to calculate E_B, we obtain I_c=6.5nA, in good agreement with the experimental value measured at 0.25K[136] (see Fig. 4.5.a).

The transition to a different regime can be inferred also from the fact that device 6W shows a finite resistance R_0 at low voltages, even at the lowest temperature. Resuming the arguments discussed in the previous section, by calculating the tunneling rate Γ[1], R_0 value of the order of 500Ω, as measured on junction 6W (see Fig. 4.5.b), is obtained with Q≃1, consistent with the high frequency Q_1, which reflects dissipation in the low voltage regime, determined by classical methods at 1.45K. In addition, as shown in Fig. 4.5.b, R_0 decreases with temperature and levels off around 0.3K. The saturation of R_0 marks the entrance into the quantum regime[136]. Iansiti et al.[30] report that the value and the behavior of R_0 depends on the ratio x. The R_0 values shown in Fig. 4.5.b are consistent with those found in Ref. [30] resulting from numerical simulations using x=0.65.

From the estimated value of the plasma frequency ω_p ≈40GHz, we calculate a crossover temperature T_{cross} of 120mK. This temperature is much lower than the one where, in our experiment, we measure a levelling of the R_0 values (0.3K). Such equation for the crossover temperature has been estimated in the more common regime $E_J >> E_c$[39]. This temperature is much lower than the one where, in our experiment, a leveling of the R_0 values is observed. This discrepancy has to be probably ascribed to the fact that, in the regime $E_J \simeq E_c$, the binding energy is modified with respect to the case $E_J >> E_c$ and the phase delocalization is larger and hence the transition rate should be larger. Therefore the probability for quantum tunnelling of the phase is increased, thus pushing up the temperature where quantum tunnelling have a significant impact on the phase dynamics. Finally, we point out that junction 1W has similar values of ω_p and T_{cross} (75GHz and 155mK respectively) but the condition $E_c << E_J$ results in negligible delocalization effects, and the dynamics of the junction is classical down to 0.25K, as shown by the good agreement between the experimental data and simulations (see Fig. 4.3).

4.3 Switching processes in superconducting nanowires

Superconducting nanowires have been even considered as quantum phase-slip junctions, and some of their functionalities have been shown to have a profound duality with the Josephson effect[142, 143]. The border between the two distinct regimes of the Josephson effect and of phase-slips might be quite subtle in some cases, because of the presence of controlled or intrinsic undesired nano junctions along nanowire leads, or because of intermediate transparencies of very thin barriers.

In this thesis we have shown how the phase dynamics of the JJs can be identified as encoded in the escape dynamics and specifically in the SCDs[7, 14, 40]. The study of SCDs allows us to quantify the interaction of the junction with the environment[1]. In view of a comparison between switching processes in nanowires and in JJs, in this section a recent model developed for phase-slips mechanisms in superconducting nanowire is presented[91]. The moderately damped regime stands as a clear reference for the phase-slips regime, and helps in clearly defining thermal dependences of the switching histograms in phase-slips processes[34, 35, 36, 47, 50, 56].

Superconducting nanowires show hysteretic $I - V$ characteristics at low temperatures. Because of fluctuations, the current at which the switching occurs is lower than the depairing current. Such fluctuations are known as phase-slips: the phase of the order parameter between the left and right ends of the wire changes by a multiple of 2π[37, 92]. Thermally activated phase-slips (TAPS) can provide an intrinsic source of dissipation and have been studied in wide superconducting transitions of widths of up to several Kelvins[92]. Recent experiments on even narrower superconducting nanowires have aimed to investigate quantum phase-slips (QPS), i.e. phase-slips due to quantum rather than thermal fluctuations[89, 90], as an additional proof of switching histograms as a powerful tool to learn about the nature of phase-slip fluctuations[40]. This strategy works well at low temperatures, since nanowires become hysteretic, and is complementary of traditional experiments[92], in which R(T) measurements at low bias current are used to study fluctuations. R(T) measurements become difficult at low temperatures, since the wire resistance becomes very small. Superconducting nanowires are usually in the overdamped regime, thus a single phase-slip does not result in a switching event. Instead, multiple consecutive phase-slips are required to trigger switching.

Recent experiments[90] have shown that fluctuations in the average critical current are nonmonotonic in temperature, and anticorrelation between the bath temperature and the width of the switching distributions has been observed[89]. A numerical model in order to the study the stochastic aspects of the switching dynamics in superconducting nanowires has been developed by Shah et al.[91] and the main concepts are reported in the following. The model is based on a freestanding wire of effective length L and cross-sectional area A, the ends of which are at the bath temperature T_b, as shown in Fig. 4.6.a. This design closely reproduces what can be experimentally realized. Since the wire is suspended, all heat generated locally in the wire can be taken away only through the ends. Stochastic phase-slips that heat the wire and heat dissipation that cools the wire are the dominating mechanisms. Since the phase-slip rate depends on the local temperature of the wire, heating by phase-slips can create a runaway cascade that eventually overheats the wire. The stochasticity inherent in the switching process is based on the fact that the resistive fluctuations of the superconducting nanowire consist of discrete phase-slip events that occur at random instants and are centered at random spatial locations along the wire. Given that edge effects favor phase-slip locations away from the wire ends, the source term is restricted to the region at the center of the wire. The system is thus modeled by assuming that heating takes place within a central segment of length W to which a uniform temperature T_f is ascribed, and the heat is conducted away through the end segments[91]. A simple sketch of such model is represented in Fig. 4.6.b and in Fig. 4.6.c.

Therefore the stochastic phase-slip dynamics is reduced to the following ordinary differential equation for the time evolution of the temperature of the central segment[91]:

$$\frac{dT}{dt} = -\alpha\,(T, T_b)\,(T - T_b) + \eta(T, I)\sum_i \delta(t - t_i) \tag{4.4}$$

The second term on the right-hand side corresponds to stochastic heating by phase-slips, whose rate Γ(I, T) is temperature and current dependent and

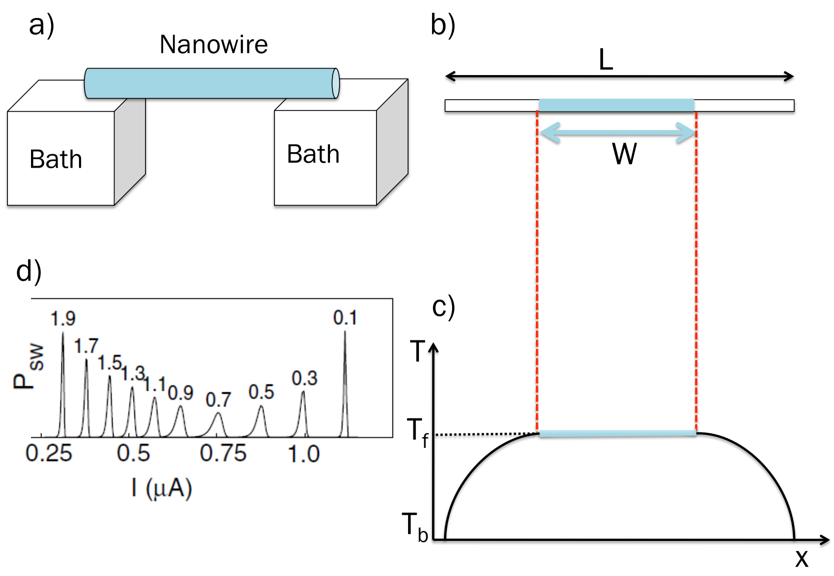

Figure 4.6: a) A superconducting nanowire is suspended between two thermal baths. b) Phase-slips occur in the central (green) segment of length W, along which the temperature T_f is uniform. Heat is carried away through the end segments. The temperature at the ends of the wire is the bath temperature T_b. c) Sketch of the temperature profile of (b). d) SCDs obtained from numerical simulations of Eqn. 4.4. Below 0.7K histograms broaden when increasing the temperature, while above 0.7K histograms shrink. ((a), (b) and (c) are adapted from Ref. [91] while (d) is taken from Ref. [91]).

follows the ubiquitus Arrhenius law:

$$\Gamma(I,T) = \Omega(I,T)\ \exp -\frac{\Delta F(I,T)}{k_B T} \tag{4.5}$$

where ΔF(I, T) is the free energy barrier given by[92]

$$\Delta F(I,T) = \left[\frac{\sqrt{6}\phi_0 I_c(T)}{k_B T}\ (1 - I/I_c(0))^{3/2}\right], \tag{4.6}$$

If T_i and T_f are the temperatures before and after a phase-slip respectively, the temperature jump η(I, T) due to a phase-slip can be expressed as:

$$A \cdot W \int_{T_i}^{T_f} C_v(y)dy = hI/2e \tag{4.7}$$

where C_v(T) is the specific heat of the wire.

The first term in Eqn. 4.4 represents the cooling mechanism as a result of conduction of heat from the central segment to the external bath via the two end segments, each of length (L−W). The temperature dependent cooling rate is given by

$$\alpha(T, T_b) = \frac{4}{W(L-W)C_v(T)} \frac{1}{T-T_b} \int_{T_b}^{T} dyK(y) \tag{4.8}$$

where K(T) is the thermal conductivity of the wire. In addition to restrictions on length scales, in the equations above the time for a phase-slip and the quasiparticle thermalization time are both assumed to be smaller than the heat diffusion time[91].

Solutions of Eqn. 4.4 have been performed numerically by Shah et al.[91] in a wide range of temperature and current. There is a region of the (I, T) plane for which the occurrence of just one phase-slip is sufficient to cause the nanowire to switch from the superconductive to the resistive state. Measurements in this range can thus provide a way of detecting and probing an individual phase-slip fluctuation. In this region the width of the switching histograms increases when increasing the temperature, following the usual thermal activation expressed by the Arrhenius law (see Fig. 4.6.d).

Such a broadening in the distribution width is indeed obtained up to a crossover temperature T_{ps}. Above T_{ps}, the distribution width shows an anomalous decrease, since histograms begin to shrink rather than broaden as shown in Fig. 4.6.d. In this region of the (I, T) plane, one phase-slip is not sufficient to induce switching and multiple phase-slips are needed. Therefore, such striking behavior of the distribution width may be understood by the following argument: the larger the number of phase-slips in the sequence inducing the transition from the superconducting to the resisitive state, the smaller the stochasticity in the switching process and, hence, the sharper the distribution of switching currents[91]. As in the case of moderately damped JJs, the change in the sign of the derivative of σ(T) is related to a change in the phase-slips dynamics from single to multiple phase-slips fluctuations in the wire.

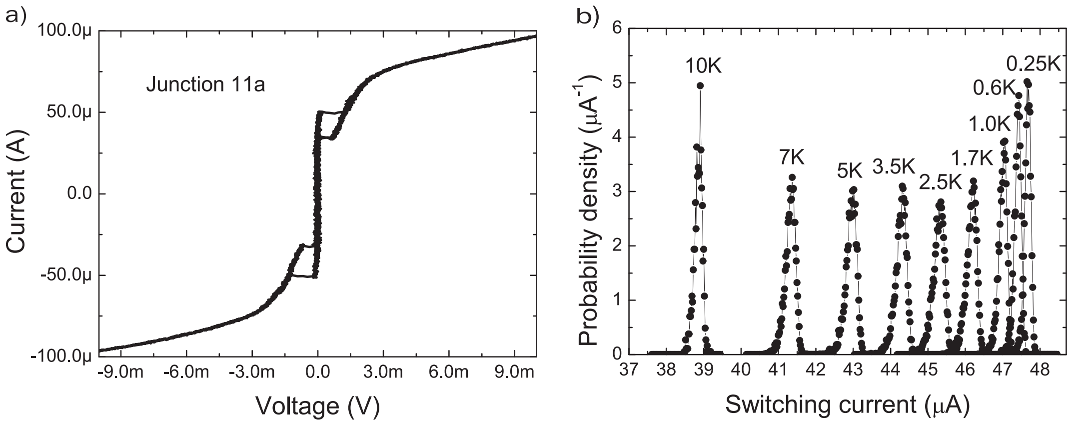

Figure 4.7: a) $I-V$ characteristic of junction 11a measured at 0.25K. b) SCDs measured on junction 11a in a wide range of temperature form 0.25K up to 10K.

4.4 Switching dynamics of high critical current density YBCO Josephson junctions

In this section switching processes of high J_c GB STO-based junction 11a are illustrated and compared with phase dynamics of moderately damped junctions studied in the previuos chapter. As shown by Fig. 4.7.a and by Table 4.1, the critical current of the junction is about 50μA and the junction width is about 200nm, thus the resulting J_c is of the order $9{\cdot}10^4$A/cm^2, from one to two orders of magnitude larger than those of the YBCO junctions analyzed in chapter 3. The nominal width of junction 11a is about 2.5μm while an effective width of about 200nm has been estimated from the Fraunhofer-like magnetic pattern. As commonly found in biepitaxial junctions, insulating impurities obstruct partially the GB channel of this junction[54], reducing its active width. Self-assembled nanoscale channels may naturally arise in the growth process of GBs and deeply influence the transport properties of the resulting junctions[130]. The perfect Fraunhofer shape of the magnetic field pattern indicates also that only one transport channel is active, thus making junction 11a a very significant junction in the lobe-lobe configuration in order to study the transport in GBs[130, 144].

As discussed in section 1.3, the possibility to scale J_c over 4 orders of magnitude represents one of the most significant advantages of GBs. This is mostly ruled by the d-wave OP symmetry and by the GB microstructure. Lattice matching across a GB at the nanoscale depends on the material growth conditions and, more importantly, the various growths determine barriers with different properties[51, 23]. GB junctions fabricated through the biepitaxial technique offer different micro or nano-structural regimes by selecting specific interface orientations with respect to the two electrodes in the patterning of the seed layer[54, 60]. The angles θ=0° and 90° define the two limiting configurations, the tilt and the twist cases respectively[54, 60]. In the tilt case the planes on the two electrodes meet along lines at the GB, current needs to travel along the c-axis in the (103) electrode and quasi-particles see on average a more uniform distributed barrier. In the twist case current always flows in the planes, but paths will be locally constricted by the nodes connecting the planes[54]. By varying the angle θ intermediate configurations will be determined and effects induced by the d-wave OP symmetry have to be taken into account. A choice of the angle θ of 50°[60] for device 11a guarantees both predominant transport across the point contacts of the planes of the two electrodes and high values of I_c, since in this configuration lobes of d-wave OP symmetry on the two sides of the junction are roughly facing each other.

In Fig. 4.7.a the $I-V$ characteristic of junction 11a measured at 0.25K is shown. The switching voltage V_{sw} is about 1mV, as for the YBCO junctions studied in the previous chapter, and hysteresis is about 30%. Deviations from the ideal RCSJ behavior are evident since a linear branch corresponding to the normal resistance R_n starts at about 5mV. In Fig. 4.7.b switching histograms measured in a wide range of temperature from 0.25K up to 10K are shown. Below 2.5K histograms broaden when increasing the temperature, following the usual TA regime, while above 2.5K histograms shrink as the temperature is increased. Therefore at about 2.5K the derivative of σ(T) changes sign.

The temperature dependence of σ of junction 11a has been reported in Fig. 4.8.a along with the thermal dependences of σ of NbN/MgO/NbN JJ studied in section 3.3 and of junction 12b analyzed in section 3.5 as terms of comparison. For all the junctions reported in Fig. 4.8.a it is possible to define a transition temperature T^* which signals the change in the sign of

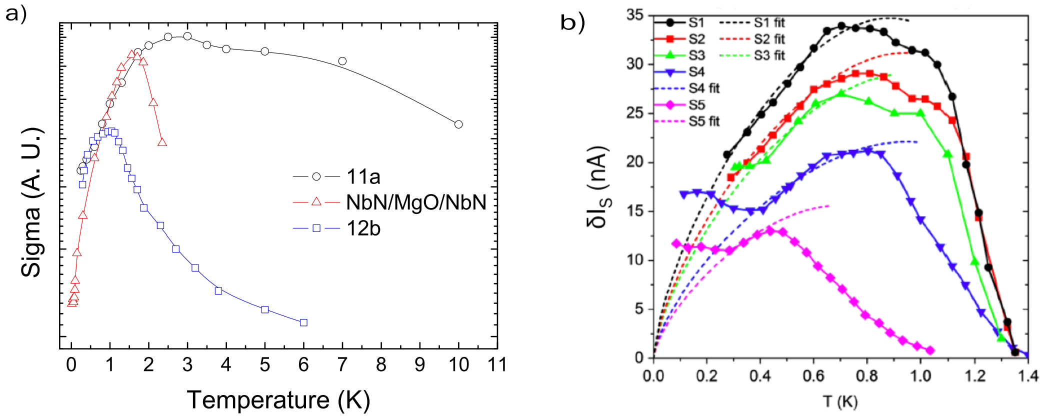

Figure 4.8: a) Thermal dependence of σ of junction 11a (black open circles) compared with those of NbN/ MgO/NbN JJ (red open triangles) and of junction 12b (blue open squares) (see sections 3.3 and 3.5). The lines are a guide for the eye. σ values have been normalized to facilitate the comparison. b) Thermal dependences of σ (symbols) of several Al nanowires measured by Li et al.[90]. Dashed line are fit of the data according to phase-slips dynamics. (The graph in (b) has been taken from Ref. [90]).

the derivative of σ(T). For NbN JJ and for junction 12b T* is the transition temperature from the TA to the PD regime, as discussed in chapter 3. Below T* thermal dependences are quite similar while above T* remarkable deviations are evident between the moderately damped junctions and junction 11a. The characteristic collapse of σ in the PD regime is not observed in junction 11a. As a term of comparison, in Fig. 4.8.b thermal dependences of σ measured by Li et al.[90] on several Al nanowires are shown. The σ(T) behavior of junction 11a resembles the phase-slips σ(T) dependences of the Al nanowires instead of the PD dynamics of moderately damped JJs.

In addition, as discussed extensively in sections 3.3 and 3.6, retrapping processes cause a progressive symmetrization of the switching distribution when increasing the temperature above the transition temperature T*. Such symmetrization is measured by the skewness γ defined in section 3.3. In Fig. 4.9.a thermal dependence of γ of junction 11a is compared with γ of the NbN JJ. While for NbN junction the skewness increases rapidly at temperatures above its transition temperature T*, the skewness of junction 11a is almost constant in temperature, indicating that no symmetrization of the switch-

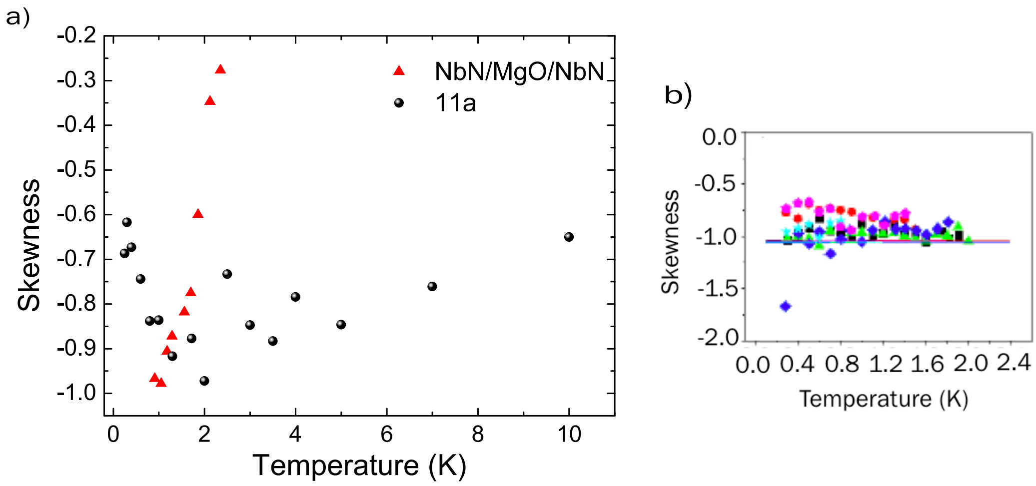

Figure 4.9: a) Thermal dependence of the skewness γ of junction 11a (black circles) compared with that of NbN/MgO/NbN JJ (red triangles) (see Fig. 3.8.b). Such behavior indicates no symmetrization of the histograms measured on junction 11a. b) Experimental values of γ as a function of the temperature of the SCDs measured on $Mo_{76}Ge_{24}$ superconducting nanowires[145]. ((b) has been taken from Ref. [145]).

ing histograms occurs. As a term of comparison, thermal dependence of γ measured on several $Mo_{76}Ge_{24}$ nanowires by Murphy et al.[145] is shown in Fig. 4.9.b. In the case of superconducting nanowires the skewness of the switching histograms does not vary in temperature.

Therefore, switching dynamics of the high J_c junction 11a presents remarkably deviations from the switching dynamics of moderately damped JJs. On the other hand, the thermal dependences of σ and γ resemble the switching dynamics observed usually in superconducting nanowires[90, 145] and could be reproduced by the model illustrated in section 4.3. The decryption of the SCDs provides a signature of the transport mode and represents a fundamental step in order to solve the duality between the phase-slips dynamics and the Josephson effect, in view of a wider phase diagram valid for superconducting weak links. Fitting of the SCDs leads to evidence of phase-slips driven phenomena for this junction with high J_c. This conclusion completes the whole picture and differences between the various cases provide some kind of general self-consistent criteria.

Measurements of SCDs spectra constitute sophisticated tools to investigate phase dynamics also in HTS JJs, where microscopic understanding of superconductivity is still missing. Well defined criteria to identify different modes of transport are given. We believe that further progress in the field will lead to novel insights not only on the Josephson effect in unconventional systems but also on the possibility to induce nanoscale transport information of relevance for the study of superconductivity in HTS.

Conclusions

We have focused on macroscopic quantum phenomena, as one of the most exciting fields of the modern physics. We have performed experiments on unconventional systems where Josephson junctions are characterized by intermediate levels of dissipation. For unconventional types of junctions, we intend both d-wave HTS JJs and low Jc NbN JJs, or devices scaled to the nano-size. Measurements of switching current distribution constitute a direct way of discriminating the phase dynamics and the transport also in nontrivial cases of moderate damping, which are going to be more and more common with advances in nanopatterning superconductors and in materials science with novel possibilities of synthesizing also hybrid coplanar systems. A wide vision on macroscopic quantum phenomena in a variety of complementary systems including d-wave junctions can promote novel arguments on the interplay of coherence and dissipation in solid state systems.

We have proved the existence of a transition between thermal activation and macroscopic quantum tunneling both in LTS and HTS JJs, in the regime of moderate damping. While this seems to be to a large extent intrinsic in HTS JJs, in LTS JJs the moderately damped regime is controllably induced by low I_c, thus by low Josephson energy E_J. More importantly we have found distinctive signatures of phase diffusion, as the appearance of an anticorrelation between temperature and the width of the switching distributions. Measurements of switching processes are supported by Monte Carlo simulations of the phase dynamics, providing a solid and reliable method to estimate the damping factor Q in moderately damped JJs. We have performed numerical simulations in a wide range of dissipation conditions and junction parameters, and direct comparison between measurements and Monte Carlo simulations allow us to reconstruct a (Q, $k_B T/E_J$) phase diagram summarizing the various activation regimes. The universal character of the phase diagram has been confirmed by the comparison with several works reported in literature. It constitutes a guideline for moderatey damped systems over a large range of junction materials, geometry and dissipation level.

We have explored a new region of the (Q, $k_B T/E_J$) phase diagram and we have demonstrated a direct transition from quantum activation to diffusive motion in grain boundary YBCO Josephson junctions. Such an experiment sets a very relevant reference in the study of the influence of dissipation on the switching statistics of Josephson junctions and is of particular relevance to understand interaction of a quantum system with the environment. Nanolitography adapted to HTS devices provides junctions characterized by very low critical currents and paves the way to the observation of fully quantum phase diffusion.

Another topic of renewed interest in the last few years is the study of switching dynamics in superconducting nanowires. Phase-slips fluctuations seem to govern the current-induced transition from the superconducting to the resistive state in such systems. Measurements of switching processes in suitably oriented GB YBCO JJs have shown to get new insights in the border between phase dynamics in Josephson junctions and phase-slips in superconducting nanowire, in view of a wider phase diagram for superconducting weak links. When looking at all regimes investigated for HTS JJs, results can be condensed in the flow chart shown in Fig. 4.10

Measurements of SCDs represent a fundamental step to investigate phase dynamics also in HTS JJs, where microscopic understanding of superconductivity is still missing. Well defined criteria to identify different regimes are given. We believe that further progress in the field will lead to novel insights on the possibility to induce nanoscale transport information of relevance for the study of superconductivity in HTS.

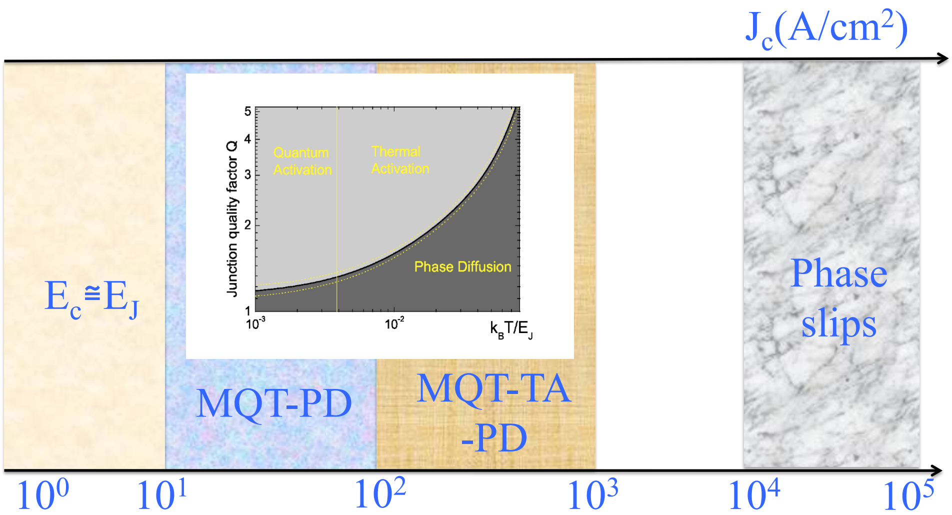

Figure 4.10: Schematic flow chart which condenses the investigated transport regimes for GB biepitaxial YBCO JJs as a function of the critical current density J_c.

Bibliography

[1] A. O. Caldeira and A. J. Leggett, Phys. Rev. Lett. **46**, 211 (1981); A. O. Caldeira and A. J. Leggett, Annals of Physics **149**, 374 (1983).

[2] B. D. Josephson, Phys. Lett. **1**, 251 (1962).

[3] A. Barone and G.釁aternò, Physics and Applications of the Josephson Effect (John Wiley and Sons, 1982).

[4] K. K. Likharev, Dynamics of Josephson Junctions and Circuits (Gordon and Breach, New York, 1986); K. K. Likharev, Rev. Mod. Phys. **51**, 101 (1979).

[5] A. F. Andreev, Zh. Eksp. Teor. Fiz. **46**, 1823 (1964) [Sov. Phys. JETP **19**, 1228 (1964)]; I. O. Kulik, Sov. Phys. JETP **30**, 944 (1969).

[6] C. C. Tsuei, J. R. Kirtley, Rev. Mod. Phys. **72**, 969 (2000).

[7] R. F. Voss and R. A. Webb, Phys. Rev. Lett. **47**, 265 (1981).

[8] L. D. Jackel, J. P. Gordon, E. L. Hu, R. E. Howard, L. A. Fetter, D. M. Tennant, R. W. Epworth, and J. Kurkijarvi, Phys. Rev. Lett. **47**, 697 (1981).

[9] W. der Boer and R. de Bruyn Ouboter, Physica B **98**, 185 (1980); D. W. Bol, R. van Weelderen, and R. de Bruyn Ouboter, Physica B **122**, 1 (1983); D. W. Bol, J. J. F. Scheffer, W. Giele, and R. de Bruyn Ouboter, Physica B **133**, 196 (1985).

[10] R. J. Prance, A. P. Long, T. D. Clarke, A. Widom, J. E. Mutton, J. Sacco, M. W. Potts, G. Negaloudis, and F. Goodall, Nature **289**, 543 (1981).

[11] I. M. Dmitrenko, V. A. Khlus, G. M. Tsoi, and V. I. Shnyrkov, Fiz. Nizk. Temp. **11**, 146 (1985) [Sov. J. Low Temp. Phys. **11**, 77 (1985)].

[12] S. Washburn, R. A. Webb, R. F. Voss, and S. M. Farris, Phys. Rev. Lett. **54**, 2712 (1985).

[13] M. H. Devoret, J. M. Martinis, D. Esteve, and J. Clarke, Phys. Rev. Lett. **53**, 1260 (1984).

[14] M. H. Devoret, J. M. Martinis, J. Clarke, Phys. Rev. Lett. **55**, 1908 (1985); J. M. Martinis, M. H. Devoret, J. Clarke, Phys. Rev. B **35**, 4682 (1987).

[15] J. Clarke, A. N. Cleland, M. H. Devoret, D. Esteve, J. M. Martinis, Science **239**, 992 (1988).

[16] J. Clarke and F. K. Wilhelm, Nature (London) **453**, 1031 (2008).

[17] J. R. Friedman, V. Patel, W. Chen, S. K. Tolpygo, and J. E. Lukens, Nature **406**, 43 (2000).

[18] A. J. Berkley, H. Xu, R. C. Ramos, M. A. Gubrud, F. W. Strauch, P. R. Johnson, J. R. Anderson, A. J. Dragt, C. J. Lobb, F. C. Wellstood, Science **300**, 1548 (2003).

[19] Y. Nakamura, Y. A. Pashkin, and J. S. Tsai, Nature **398**, 786 (1999).

[20] I. Chiorescu, Y. Nakamura, C. J. P. M. Harmans, and J. E. Mooij, Science **299**, 1869 (2003).

[21] D. Vion, A. Aassime, A. Cottet, P. Joyez, H. Pothier, C. Urbina, D. Esteve, M. H. Devoret, Science **296**, 886 (2002).

[22] J. M. Martinis, S. Nam, J. Aumentado, C. Urbina, Phys. Rev. Lett. **89**, 117901 (2002).

[23] F. Tafuri and J. R. Kirtley, Report Progress in Physics **68**, 2573 (2005).

[24] T. Bauch, F. Lombardi, F. Tafuri, A. Barone, G. Rotoli, P. Delsing, T. Claeson, Phys. Rev. Lett. **94**, 087003 (2005)

[25] T. Bauch, T. Lindstrom, F. Tafuri, G. Rotoli, P. Delsing, T. Claeson, F. Lombardi, Science **311**, 56 (2006).

[26] K. Inomata, S. Sato, K. Nakajima, A. Tanaka, Y. Takano, H. B. Wang, M. Nagao, H. Hatano, S. Kawabata, Phys. Rev. Lett. **95**, 107005 (2005).

[27] X. Y. Jin, J. Lisenfeld, Y. Koval, A. Lukashenko, A. V. Ustinov, P. Mueller, Phys. Rev. Lett. **96**, 177003 (2006).

[28] G.-H. Lee, D. Jeong, J.-H. Choi, Y.-J. Doh, H.-J. Lee, Phys. Rev. Lett. **107**, 146605 (2011).

[29] R. H. Ono, M. W. Cromar, R. L. Kautz, R. J. Soulen, J. H. Colwell, and W. E. Fogle, IEEE Trans. Magn. **MAG-23**, 1670 (1987).

[30] M. Iansiti, A. T. Johnson, W. F. Smith, H. Rogalla, C. J. Lobb, M. Tinkham, Phys. Rev. Lett. **59**, 489 (1987); M. Iansiti, M. Tinkham, A. T. Johnson, W. F. Smith, C. J. Lobb, Phys. Rev. B **39**, 6465 (1989).

[31] R. L. Kautz and J. M. Martinis, Phys. Rev. B **42**, 9903 (1990); J. M. Martinis and R. L. Kautz, Phys. Rev. Lett. **63**, 1507 (1989).

[32] Y. Zhang, G. Liu, and C. N. Lau, Nano Res. **1**, 145-151 (2008).

[33] I. V. Borzenets, U. C. Coskun, S. J. Jones, and G. Finkelstein, Phys. Rev. Lett. **107**, 137005 (2011).

[34] J. Männik, S. Li, W. Qiu, W. Chen, V. Patel, S. Han, J. E. Lukens, Phys. Rev. B **71**, 220509 (2005).

[35] J. M. Kivioja, T. E. Nieminen, J. Claudon, O. Buisson, F. W. J. Hekking, J. P. Pekola, Phys. Rev. Lett. **94**, 247002 (2005).

[36] V. M. Krasnov, T. Bauch, S. Intiso, E. Hürfeld, T. Akazaki, H. Takayanagi, P. Delsing, Phys. Rev. Lett. **95**, 157002 (2005); V. M. Krasnov, T. Golod, T. Bauch, P. Delsing, Phys. Rev. B **76**, 224517 (2007).

[37] M. Tinkham, Introduction to Superconductivity, McGraw-Hill, New York, 1996.

[38] H. A. Kramers, Physica (Utrecht) **7**, 284 (1940).

[39] H. Grabert, P. Olschowski, and U. Weiss, Phys. Rev. B **36**, 1931 (1987).

[40] T. A. Fulton and L. N. Dunkleberger, Phys. Rev. B **9**, 4760 (1974).

[41] D. B. Schartz, B. Sen, C. N. Archie, and J. E. Lukens, Phys. Rev. Lett. **55**, 1547 (1985).

[42] P. Silvestrini, S. Pagano, R. Cristiano, O. Liengme, and K. E. Gray, Phys. Rev. Lett. **60**, 844 (1988); C. Cosmelli, P. Carelli, M. G. Castellano, F. Chiarello, G. Diambrini Palazzi, R. Leoni, and G. Torrioli, Phys. Rev. Lett. **82**, 5357 (1999); B. Ruggiero, M. G. Castellano, G. Torrioli, C. Cosmelli, F. Chiarello, V. G. Palmieri, C. Granata, and P. Silvestrini, Phys. Rev. B 59, 177 (1999).

[43] A. Wallraff, T. Duty, A. Lukashenko, and A. V. Ustinov, Phys. Rev. Lett. **90**, 370031 (2003).

[44] W. C. Stewart, Appl. Phys. Lett. **12**, 277 (1968); R. Cristiano and P. Silvestrini, J. Appl. Phys. **60**, 9 (1986); Y. C. Chen, M. P. A. Fisher, and A. J. Leggett, J. Appl. Phys. **64**, 6 (1988); M. G. Castellano, G. Torrioli, F. Chiarello, C. Cosmelli, and P. Carelli, J. Appl. Phys. **86**, 11 (1999).

[45] E. Ben-Jacob, D. J. Bergman, B. J. Matkowsky, and Z. Schuss, Phys. Rev. A **26**, 2805 (1982).

[46] Myung-Ho Bae, M. Sahu, Hu-Jong Lee, A. Bezryadin, Phys. Rev. B **79**, 104509 (2009).

[47] L. Longobardi, D. Massarotti, G. Rotoli, D. Stornaiuolo, G. Papari, A. Kawakami, G.P. Pepe, A. Barone, F. Tafuri, Phys. Rev. B **84**, 184504 (2011).

[48] H. F. Yu, X. B. Zhu, Z. H. Peng, Ye Tian, D. J. Cui, G. H. Chen, D. N. Zheng, X. N. Jing, Li Lu, S. P. Zhao, S. Han, Phys. Rev. Lett. **107**, 067004 (2011).

[49] D. Massarotti, L. Longobardi, L. Galletti, D. Stornaiuolo, D. Montemurro, G. P. Pepe, G. Rotoli, A. Barone, F. Tafuri, J. Low Temp. Phys. **38**, 263 (2012).

[50] J. C. Fenton and P. A. Warburton, Phys. Rev. B **78**, 054526 (2008).

[51] H. Hilgenkamp, J. Mannhart, Rev. Mod. Phys. **74**, 485 (2002).

[52] J. Mannhart, P. Chaudhari, D. Dimos, C. C. Tsuei, T. M. McGuire, Phys. Rev. Lett. **61**, 2476 (1988); P. Chaudari, J. Mannhart, D. Dimos, C. C. Tsuei, C. C. Chi, M. M. Oprysko, M. Scheuermann, Phys. Rev. Lett. **60**, 1653 (1988).

[53] K. Char, M. S. Colclough, S. M. Garrison, N. Newman, G. Zaharchuk, Appl. Phys. Lett. **59**, 733 (1991).

[54] F. Tafuri, F. Miletto Granozio, F. Carillo, A. Di Chiara, K. Verbist, G. Van Tendeloo, Phys. Rev. B **59**, 11523 (1999); F. Tafuri, F. Carillo, F. Lombardi, F. Miletto Granozio, F. Ricci, U. Scotti di Uccio, A. Barone, G. Testa, E. Sarnelli, J. R. Kirtley, Phys. Rev. B **62**, 14431 (2000).

[55] D. Stornaiuolo, G. Papari, N. Cennamo, F. Carillo, L. Longobardi, D. Massarotti, A. Barone, F. Tafuri, Supercond. Sci. Technol. **24**, 045008 (2011).

[56] L. Longobardi, D. Massarotti, D. Stornaiuolo, L. Galletti, G. Rotoli, F. Lombardi, F. Tafuri, Phys. Rev. Lett. **109**, 050601 (2012).

[57] D. J. Van Harlingen, Rev. Mod. Phys. **67**, 515 (1995).

[58] D. A. Wollman, D. J. Van Harlingen, W. C. Lee, D. M. Ginsberg, A. J. Leggett, Phys. Rev. Lett. **71**, 2134 (1993).

[59] D. A. Wollman, D. J. Van Harlingen, J. Giapintzakis, D. M. Ginsberg, Phys. Rev. Lett. **74**, 797 (1995).

[60] F. Lombardi, F. Tafuri, F. Ricci, F. Miletto Granozio, A. Barone, G. Testa, E. Sarnelli, J. R. Kirtley, C. C. Tsuei, Phys. Rev. Lett. **89**, 207001 (2002).

[61] V. V. Ryazanov, V. A. Oboznov, A. V. Veretennikov, A. Yu. Rusanov, Rev. B **65**, 020501(R) (2001).

[62] A. Bauer, J. Bentner, M. Aprili, M. L. Della Rocca, M. Reinwald, W. Wegscheider, C. Strunk, Phys. Rev. Lett. **92**, 217001 (2004).

[63] A. I. Buzdin, Rev. Mod. Phys. **77**, 935976 (2005).

[64] K. Senapati, M. G. Blamire, Z. H. Barber, Nat. Mater. **10**, 849 (2011).

[65] S. Kashiwaya, Y. Tanaka, Rep. Prog. Phys. **63**, 1641 (2000).

[66] C. C. Tsuei, J. R. Kirtley, C. C. Chi, L. S. Yu-Jahnes, A. Gupta, T. Shaw, J. Z. Sun, M. B. Ketchen, Phys. Rev. Lett. **73**, 593 (1994).

[67] M. B. Walker, J. Luettmer-Strathman, Phys. Rev. B **54**, 588 (1996).

[68] M. Sigrist, T. M. Rice, J. Phys. Soc. Jpn. **61**, 4283 (1992).

[69] H. Hilgenkamp, Supercond. Sci. Technol. **21**, 034011 (2008).

[70] L. Fu, C. L. Kane, E. J. Mele, Phys. Rev. Lett. **100**, 096407 (2008).

[71] Y. Tanaka, T. Yokoyama, N. Nagaosa, Phys. Rev. Lett. **103**, 107002 (2009).

[72] R. M. Lutchyn, J. D. Sau, S. Das Sarma, Phys. Rev. Lett. **105**, 077001 (2010).

[73] P. Lucignano, A. Mezzacapo, F. Tafuri, A. Tagliacozzo, Phys. Rev. B **86**, 144513 (2012).

[74] I. O. Kulik, A. N. Omelyanchuk, Pis'ma Zh. Eksp. Teor. Fiz. **21**, 216 (2005) [JETP Lett. 21, 96 (2005)].

[75] Y. V. Fominov, A. A. Golubov, and M. Y. Kupriyanov, JETP Lett. **77**, 587 (2003); M. H. S. Amin and A. Y. Smirnov, Phys. Rev. Lett. **92**, 017001 (2004); S. Kawabata, S. Kashiwaya, Y. Asano, and Y. Tanaka, Phys. Rev. B **70**, 132505 (2004); ibid. **72**, 052506 (2005); T. Yokoyama, S. Kawabata, T. Kato, and Y. Tanaka, Phys. Rev. B **76**, 134501 (2007).

[76] P. W. Anderson, Science **288**, 480 (2000); Handbook of High Temperature Superconductivity: Theory and Experiment, edited by J. S. Brooks and J. Robert Schrieffer (Springer, 2006).

[77] G. Rotoli, T. Bauch, T. Lindstrom, D. Stornaiuolo, F. Tafuri, and F. Lombardi, Phys. Rev. B **75**, 144501 (2007).

[78] R. Kleiner, F. Stenmeyer, G. Kunkel, and P. Muller, Phys. Rev. Lett. **68**, 2394 (1992).

[79] R. Kleiner, P. Muller, Phys. Rev. B **49**, 1327 (1994).

[80] A. A. Yurgens, Supercond. Sci. Technol. **13**, R85 (2000).

[81] H. B. Wang, P. H. Wu, T. Yamashita, Appl. Phys. Lett. **78**, 4010 (2001).

[82] Y. J. Doh, J. A. van Dam, A. L. Roest, E. P. A. M. Bakkers, L. P. Kouwenhoven, and S. De Franceschi, Science **309**, 272 (2005).

[83] J. Xiang, A. Vidan, M. Tinkham, R. M. Westervelt, and C. M. Lieber, Nat. Nano. **1**, 208 (2006).

[84] P. Jarillo-Herrero, J. A. van Dam, and L. P. Kouwenhoven, Nature **439**, 953 (2006).

[85] J. P. Cleuziou, W. Wernsdorfer, V. Bouchiat, T. Ondarcuhu, and M. Monthioux, Nat. Nano. **1**, 53 (2006).

[86] G. Katsaros, P. Spathis, M. Stoffel, F. Fournel, M. Mongillo, V. Bouchiat, F. Lefloch, A. Rastelli, O. G. Schmidt, and S. De Franceschi, Nat. Nano. **5**, 458 (2010).

[87] H. Courtois, M. Meschke, J. T. Peltonen, and J. P. Pekola, Phys. Rev. Lett. **101**, 067002 (2008).

[88] L. Angers, F. Chiodi, G. Montambaux, M. Ferrier, S. Gureron, H. Bouchiat, and J. C. Cuevas, Phys. Rev. B **77**, 165408 (2008).

[89] M. Sahu, M. H. Bae, A. Rogachev, D. Pekker, T. C. Wei, N. Shah, P. M. Goldbart, A. Bezryadin, Nat. Phys. **5**, 503 (2009).

[90] P. Li, P. M. Wu, Y. Bomze, I. V. Borzenets, G. Finkelstein, A. M. Chang, Phys. Rev. Lett. **107**, 137004 (2011).

[91] N. Shah, D. Pekker, and P. M. Goldbart, Phys. Rev. Lett. **101**, 207001 (2008).

[92] W. A. Little, Phys. Rev. **156**, 396 (1967); J. S. Langer and V. Ambegaokar, Phys. Rev. **164**, 498 (1967); D. E. McCumber and B. I. Halperin, Phys. Rev. B **1**, 1054 (1970); N. Giordano, Phys. Rev. Lett. **61**, 2137 (1988); A. Bezryadin, C. N. Lau, and M. Tinkham, Nature **404**, 971 (2000); F. Altomare, A. M. Chang, M. R. Melloch, Y. Hong, and C. W. Tu, Phys. Rev. Lett. **97**, 017001 (2006).

[93] J. Cain, Parasitic inductance of multilayer ceramic capacitors. Technical report, AVX Corporation.

[94] F. P. Milliken, J. R. Rozen, G. A. Keefe, and R. H. Koch, Rev. Sci. Instrum. **78**, 024701 (2007).

[95] L. Spietz, J. Teufel, and R. J. Schoelkopf, e-print arXiv:cond-mat/0601316v1.

[96] K. Bladh, D. Gunnarsson, E. Hurfeld, S. Devi, C. Kristoffersson, B. Smalander, S. Pehrson, T. Claeson, and P. Delsing, Rev. Sci. Instrum. **74**, 1323 (2003).

[97] A. Fukushima, A. Sato, A. Iwasa, Y. Nakamura, T. Komatsuzaki,Y. Sakamoto, IEEE Trans. Instrum. Meas. **46**, 289 (1997).

[98] H. W. Ott, Noise Reduction Techniques in Electronic Systems (Wiley Interscience, New York, 1988).

[99] R. Morrison, Grounding and Shielding Techniques (Wiley Interscience, New York, 1998).

[100] A. Bennett, L. Longobardi, V. Patel, W. Chen, D. V. Averin, and J. E. Lukens, Quantum Inf. Process. **8**, 217 (2009).

[101] Y. L. Chen, J. G. Analytis, J. H. Chu, Z. K. Liu, S. K. Mo, X. L. Qi, H. J. Zhang, D. H. Lu, X. Dai, Z. Fang, S. C. Zhang, I. R. Fisher, Z. Hussain, and Z. X. Shen, Science **325**, 178 (2009).

[102] M. Z. Hasan and C. L. Kane, Rev. Mod. Phys. **82**, 4 (2010).

[103] A. J. Millis, Nat. Phys. **7**, 749-750 (2011).

[104] A. Brinkman, M. Huijben, M. Van Zalk, J. HuiJben, U. Zeitler, J. C. Maan, W. G. Van der Wiel, G. Rijnders, D. H. A. Blank, and H. Hilgenkamp, Nat. Mater. **6**, 493-496 (2007).

[105] N. Reyren, S. Thiel, A. D. Caviglia, L. Fitting Kourkoutis, G. Hammerl, C. Richter, C. W. Schneider, T. Kopp, A. S. Rüetschi, D. Jaccard, M. Gabay, D. A. Muller, J. M. Triscone, J. Mannhart, Science **317**, 5842 (2007).

[106] Ariando, X. Wang, G. Baskaran, Z. Q. Liu, J. Huijben, J. B. Yi, A. Annadi, A. Roy Barman, A. Rusydi, S. Dhar, Y. P. Feng, J. Ding, H. Hilgenkamp, and T. Venkatesan, Nat. Comms. **2**, 188 (2011).

[107] Lu Li, C. Richter, J. Mannhart, and R. C. Ashoori, Nat. Phys. **7**, 762-766 (2011).

[108] P. Perna, D. Maccariello, M. Radovic, U. Scotti di Uccio, I. Pallecchi, M. Codda, D. Marré, C. Cantoni, J. Gazquez, M. Varela, S. J. Pennycook, and F. Miletto Granozio, Appl. Phys. Lett. **97**, 259901, (2010).

[109] C. Aruta, S. Amoruso, G. Ausanio, R. Bruzzese, E. Di Gennaro, M. Lanzano, F. Miletto Granozio, M. Riaz, A. Sambri, U. Scotti di Uccio, and X. Wang, Appl. Phys. Lett. **101**, 031602 (2012).

[110] F. Tafuri, D. Massarotti, L. Galletti, D. Stornaiuolo, D. Montemurro, L. Longobardi, P. Lucignano, G. Rotoli, G. P. Pepe, A. Tagliacozzo, and F. Lombardi, J. Supercond. Nov. Magn. **26**, 21-41 (2013).

[111] D. Massarotti, L. Longobardi, L. Galletti, D. Stornaiuolo, G. Rotoli, and F. Tafuri, Low Temp. Phys. [Fizika Nizkikh Temperatur] **39**, 3 (2013).

[112] A. Wallraff, A. Lukashenko, C. Coqui, A. Kemp, T. Duty and A. V. Ustinov, Rev. Sci. Instrum. **74**, 8 (2003).

[113] M. Ejrnaes, A. Casaburi, R. Cristiano, O. Quaranta, S. Marchetti, N. Martucciello, S. Pagano, A. Gaggero, F. Mattioli, R. Leoni, P. Cavalier, and J. C. Villégier, Appl. Phys. Lett. **95**, 132503 (2009).

[114] F. Marsili, F. Najafi, C. Herder, and K. K. Berggren, Appl. Phys. Lett. **98**, 093507 (2011).

[115] S. B. Kaplan, C. C. Chi, D. N. Langenberg, J. J. Chang, S. Jafarey, and D. J. Scalapino, Phys. Rev. B **14**, 4854 (1976).

[116] A. Wallraff, A. Lukashenko, J. Lisenfeld, A. Kemp, M. V. Fistul, Y. Koval, and A. V. Ustinov, Nature **425**, 155 (2003).

[117] S. Saito, M. Thorwart, H. Tanaka, M. Ueda, H. Nakano, K. Semba, and H. Takayanagi, Phys. Rev. Lett. **93**, 037001 (2004).

[118] B. Ivlev, G. Pepe, R. Latempa, A. Barone, F. Barkov, J. Lisenfeld, and A. V. Ustinov, Phys. Rev. B **72**, 094507 (2005).

[119] H. Yamamori, T. Yamada, H. Sasaki. and A. Shoji, IEEE Trans. Appl. Supercond. **20**, 71 (2010).

[120] V. Larrey, J. C. Villegier, M. Salez, F. Miletto Granozio, and A. Karpov, IEEE Trans. Appl. Supercond. **9**, 3216 (1999).

[121] A. Kawakami, Z. Wang, and S. Miki, J. Appl. Phys. **90**, 4796 (2001).

[122] J. S. Kline, H. Wang, S. Oh, J. M. Martinis, and D. P. Pappas, Supercond. Sci. Technol. **22**, 015004 (2009).

[123] L. Longobardi, D. Massarotti, G. Rotoli, D. Stornaiuolo, G. Papari, A. Kawakami, G. P. Pepe, A. Barone, F. Tafuri. Appl. Phys. Lett. **99**, 062510 (2011).

[124] A. Shoji, M. Aoyagi, S. Kosaka, F. Shinoki, and H. Hayakawa, Appl. Phys. Lett. **46**, 1098 (1985).

[125] M. P. Tu, K. Mbaye, L. Wartski, and J. Halbritter, J. Appl. Phys. **63**, 4586 (1988).

[126] M. A. H. Nerenberg and J. A. Blackburn, Phys. Rev. B **9**, 3735 (1974).

[127] K. S. Il'in, M. Lindgren, M. Currie, A. D. Semenov, G. N. Gol'tsman, R. Sobolewski, S. I. Cherednichenko, and E. M. Gershenzon, Appl. Phys. Lett. **76**, 2752 (2000).

[128] A. I. Larkin and Yu. N. Ovchinnikov, Sov. Phys. JETP **64**, 185 (1986).

[129] Y. Nakamura, H. Terai, K. Inomata, T. Yamamoto, W. Qiu, and Z. Wang, Appl. Phys. Lett. **99**, 212502 (2011); Y. Yu, S. Han, X. Chu, S. I. Chu, Z. Wang, Science **296**, 889 (2002).

[130] P. Lucignano, D. Stornaiuolo, F. Tafuri, B. L. Altshuler and A. Tagliacozzo, Phys. Rev. Lett. **105**, 147001 (2010).

[131] T. Sakudo and H. Unoki, Phys. Rev. Lett. **26**, 851 (1971).

[132] R. Gross, P. Chaudari, M. Kawasaki and A. Gupta, IEEE Trans. Magn. **27**, 3227 (1991).

[133] S. C. Tidrow, A. Tauber, W. D. Wilber, R. T. Lareau, C. D. Brandle, G. W. Berkstresser, A. J. Ven Graitis, D. M. Potrepka, J. I. Budnick, and J. Z. Wu, IEEE Trans. Appl. Supercond. **7**, 1766 (1997).

[134] D. Stornaiuolo, G. Rotoli, K. Cedergren, D. Born, T. Bauch, F. Lombardi, F. Tafuri, J. Appl. Phys. **107**, 11390 (2010).

[135] Y. Yoon, S. Gasparinetti, M. Mottonen, and J. P. Pekola, J. Low Temp. Phys. **163**, 164 (2011).

[136] D. Stornaiuolo, G. Rotoli, D. Massarotti, F. Carillo, L. Longobardi, F. Beltram, and F. Tafuri, to be published in Phys. Rev. B.

[137] D. Gustafsson, D. Golubev, M. Fogelström, T. Claeson, S. Kubatkin, T. Bauch and F. Lombardi, Nat. Nano., doi:10.1038/nnano.2012.214.

[138] R. Wölbing, T. Schwarz, J. Nagel, M. Kemmler, D. Koelle, and R. Kleiner, e-print arXiv:cond-mat/1301.1189; J. Nagel, K. B. Konovalenko, M. Kemmler, M. Turad, R. Werner, E. Kleisz, S. Menzel, R. Klingeler, B. Büchner, R. Kleiner, and D. Koelle, Supercond. Sci. Technol. **24**, 015015 (2011).

[139] F. Carillo, G. Papari, D. Stornaiuolo, D. Born, D. Montemurro, P. Pingue, F. Beltram, and F. Tafuri, Phys. Rev. B **81**, 054505 (2010); G. Papari, F. Carillo, D Stornaiuolo, L. Longobardi, F. Beltram and F. Tafuri, Supercond. Sci. Technol. **25**, 035011 (2012).

[140] P. A. Rosenthal, M. F. L. Beasley, K. Char, M. S. Colclough and G. Zaharchuk, Appl. Phys. Lett. **59**, 26, (1991).

[141] D. Vion, M. Gotz, P. Joyez, D. Esteve, and M. H. Devoret, Phys. Rev. Lett. **77**, 3435 (1996).

[142] J. E. Mooij, and Y. V. Nazarov, Nat. Phys. **2**, 169-172 (2006).

[143] O. V. Astafiev, L. B. Ioffe, S. Kafanov, Yu. A. Pashkin, K. Yu. Arutyunov, D. Shahar, O. Cohen and J. S. Tsai, Nature **484**, 355-358 (2012).

[144] A. Tagliacozzo, D. Born, D. Stornaiuolo, E. Gambale, D. Dalena, F. Lombardi, A. Barone, B. L. Altshuler, and F. Tafuri, Phys. Rev. B **75**, 012507 (2007); A. Tagliacozzo, F. Tafuri, E. Gambale, B. Jouault, D. Born, P. Lucignano, D. Stornaiuolo, F. Lombardi, A. Barone, and B. L. Altshuler, Phys. Rev. B **79**, 024501 (2009).

[145] A. Murphy, P. Weinberg, T. Aref, U. Coskun, V. Vakaryuk, A. Levchenko, and A. Bezryadin, e-print arXiv:cond-mat/1303.2620.